TOHOKU UNIVERSITY

MASTER THESIS

Role of the ^{7}Be$(n, p_1)^{7}$Li* Reaction in the Cosmological Lithium Problem Studied with the ^{9}Be$(^{3}$He$, \alpha)^{8}$Be$^{*}(p)^{7}$Li Reaction

Author:
Shunki ISHIKAWA

Supervisor:
Prof. Naohito IWASA

Experimental Nuclear Physics Group
Department of Physics, Graduate School of Science

Contents

Chapter 1

Abstract

The expansion, called Big Bang, started when the whole universe was in an extremely hot and dense state nearly 13.8 billion years ago. The standard Big Bang model describes the evolution of the universe, and there are three observational and historical evidences which ensure this model: the cosmic expansion, the Cosmic Microwave Background (CMB) radiation and the Big Bang Nucleosynthesis (BBN).

Theoretical BBN calculation predicts the primordial abundances of light elements which enter the BBN reaction network during the period ranging from around 1 sec to 3 mins after the expansion started. Since the cosmic baryon density, the only free parameter in the BBN calculation, has recently been determined precisely by the measurement of CMB radiation, the BBN calculation is basically parameter free. It simply employs physical inputs, such as the number of neutrino family, the neutron lifetime, the nuclear cross sections, and so on which have been investigated individually. Consequently, the comparison between theoretically predicted abundances and observed abundances of light elements can be performed explicitly. It is found that there is a great agreement for deuterium (D) abundance, and fine agreements for ^{3}He and ^{4}He abundances. These quantitative concordances represent the credibility of the BBN calculation as one of the strong probes for the early universe. However, it appears that only for ^{7}Li, the abundance predicted by the BBN calculation is overestimated compared with the observation by a factor of three to four. This disagreement is known as the "cosmological lithium problem" [1] and is counted as one of the most important problems in nuclear astrophysics.

One of the possible ways to approach this problem is to consider the following scenario: ^{7}Be, the main source of ^{7}Li through the electron-capture decay, sees its abundance decreasing during the BBN period. The $^7\mathrm{Be}(n,p)^7\mathrm{Li}$ reaction is of primary importance in the destruction of ^{7}Be, followed by the $^7\mathrm{Li}(p,\alpha)^4\mathrm{He}$ reaction to destroy most of ^{7}Li produced. The reaction rate of the former has been deduced based on the direct reaction measurement for the energy range from thermal to 13.5 keV neutron energy, while above 13.5 keV it has been determined based on the inverse reaction using detailed balance; however, the inverse reaction measurement does not provide the the $^7\mathrm{Be}(n,p_1)^7\mathrm{Li}^*(0.478\ \mathrm{MeV})$ reaction cross section. Since the relevant energy is considered up to about 2 MeV in the BBN calculation, investigation on the $^7\mathrm{Be}(n,p_1)^7\mathrm{Li}^*$ reaction cross section is required.

We have carried out experiment of the $^9\mathrm{Be}(^3\mathrm{He},\alpha)^8\mathrm{Be}^*(p)^7\mathrm{Li}$ reaction at 30 MeV to deduce Γ_{p1}/Γ_{p0} ratio, the ratio between the proton decay widths to the ground state and to the first excited state of ^{7}Li, for each relevant resonance state of ^{8}Be. The experiment was performed using the magnetic spectrograph ENMA at the Tandem accelerator facility in Japan Atomic Energy Agency (JAEA). Resonance states populated by the $(^3\mathrm{He},\alpha)$ reaction were determined by measuring the magnetic rigidity of α particles at zero degree, and decay-protons were measured in coincidence by

silicon strip detectors surrounding the target. We have succeeded in separating the decay events to the first excited state of ^{7}Li from the ones to the ground state, and have found that the $^{7}\mathrm{Be}(n, p_1)^{7}\mathrm{Li}^{*}(0.478\ \mathrm{MeV})$ reaction has a significant contribution to the total cross section. In this thesis the experimental results will be discussed.

Brief introductions of the cosmological lithium problem are summarized in Chapter 2. Based on the problem posed in Chapter 2, the motivation and purpose to perform the measurement of the $^{9}\mathrm{Be}(^{3}\mathrm{He}, \alpha)^{8}\mathrm{Be}^{*}(p)^{7}\mathrm{Li}$ reaction will be explained in Chapter 3. For the details of the experimental aspects such as the properties of experimental apparatus will be shown in Chapter 4, followed by the explanation of procedure, and the analysis on the experimental data will be discussed in Chapter 5. In Chapter 6, the summary of this thesis will be presented, and also, prospect for the future works will be explained.

Chapter 2

Introduction

The predicted abundance of ^{7}Li by the Big Bang Nucleosynthesis (BBN) calculation is overestimated by a factor of three to four when compared with the observed abundance. Even though, the BBN calculation is believed as one of the strong and reliable probes for the early universe. In this chapter 2, brief introductions related to the "cosmological lithium problem" are presented. Important parameters will be introduced in Section 2.1 along with historical/observational stories. Following this, the result of the BBN calculation will be shown in Section 2.2; the lithium problem will be posed. Some approaches to solve the problem will be explained in Section 2.3 and 2.4.

2.1 Standard Big Bang Nucleosynthesis

2.1.1 General Aspects

The standard Big Bang model is based on two assumptions: Albert Einstein's general relativity, and the cosmological principle which states that the distribution of matter in the universe filled with a perfect fluid is homogeneous and isotropic when viewed on a large scale. Here, the geometry of the universe is described by the Friedmann-Lemaître-Robertson-Walker (FLRW) metrics

$$ds^2 = -dt^2 + a^2(t)\left[\frac{dr^2}{1-kr^2} + r^2(d\theta^2 + \sin\theta d\phi^2)\right] \quad , \tag{2.1}$$

where $a(t)$ is the cosmic scale factor which relates to the red-shift parameter z through $1 + z = 1/a(t)$, and $k = +1, 0, -1$ represent closed, flat and open universes, respectively. The Einstein field equation from the general relativity is written in the form of

$$G_{\mu\nu} + \Lambda g_{\mu\nu} = 8\pi G T_{\mu\nu} \quad , \tag{2.2}$$

where G and Λ are, respectively, the gravitational and the cosmological constants, and $T_{\mu\nu}$ is the energy-momentum tensor. $G_{\mu\nu}$ is the Einstein tensor which is given in terms of the Ricci tensor $R_{\mu\nu}$ and Ricci scalar R as

$$G_{\mu\nu} = R_{\mu\nu} - \frac{1}{2} g_{\mu\nu} R \quad . \tag{2.3}$$

Ricci tensor $R_{\mu\nu}$ is expressed in terms of Christoffel symbols $\Gamma^{\sigma}_{\mu\nu}$ and their derivatives as

$$R_{\mu\nu} = \frac{\partial \Gamma^{\lambda}_{\lambda\mu}}{\partial x^{\nu}} - \frac{\partial \Gamma^{\lambda}_{\mu\nu}}{\partial x^{\lambda}} + \Gamma^{\lambda}_{\mu\sigma}\Gamma^{\sigma}_{\nu\lambda} - \Gamma^{\lambda}_{\mu\nu}\Gamma^{\sigma}_{\lambda\sigma} \quad . \tag{2.4}$$

For the FLRW metrics the Einstein field equation yields two types of Friedmann equations: The first equation is derived from the (ij) component in Eq.(2.2)[1]. It represents the energy conservation in the form of

$$\dot{\rho} = -\frac{3\dot{a}}{a}\left(\rho + P\right) \quad , \tag{2.5}$$

where ρ is the total mass-energy density which sums the contributions from all cosmic components (see below). P is the pressure of the universe. Here and so as in the following context, a dot subscript refers to a derivative with respect to the cosmic time t.

The other equation is derived from the (00) component. The expression governs the expansion of the universe in the form of

$$\left(\frac{\dot{a}}{a}\right)^2 + \frac{k}{a^2} = \frac{8\pi G\rho}{3} + \frac{\Lambda}{3} \quad , \tag{2.6}$$

which can also be expressed in terms of the contributions from the universal components as

$$\begin{aligned} H^2(t) \equiv \left(\frac{\dot{a}}{a}\right)^2 &= \frac{8\pi G(\rho_{\rm R} + \rho_{\rm M})}{3} - \frac{k}{a^2} + \frac{\Lambda}{3} \\ &= H_0^2\left[\frac{\Omega_R}{a^4} + \frac{\Omega_M}{a^3} + \frac{\Omega_k}{a^2} + \Omega_\Lambda\right] \quad . \end{aligned} \tag{2.7}$$

The function $H(t)$ is the expansion rate of the universe, the present value of which is called Hubble's constant $H_0 = h \times 100\mathrm{km/s/Mpc}$ with $h \approx 0.68$. The subscripts of the mass-energy densities $\rho_{\rm R}$ and $\rho_{\rm M}$, respectively, correspond to the relativistic (R) and non-relativistic (M) matters. Λ refers to the "vacuum energy" or to the so-called "dark energy". In the second line of Eq. (2.7), Ω_i is the density parameter of a component i of the universe. Namely, there are four universal components (relativistic and non-relativistic matters, curvature and cosmological constant) whose density parameters are given by

$$\Omega_R = \frac{8\pi G\rho_R}{3H_0^2} \equiv \frac{\rho_R}{\rho_{\rm crit}} \quad , \tag{2.8}$$

$$\Omega_M = \frac{8\pi G\rho_M}{3H_0^2} \equiv \frac{\rho_M}{\rho_{\rm crit}} \quad , \tag{2.9}$$

$$\Omega_k = -\frac{k}{H_0^2} \quad , \tag{2.10}$$

$$\Omega_\Lambda = \frac{\Lambda}{3H_0^2} \quad , \tag{2.11}$$

where $\rho_{\rm crit}$ is the critical density

$$\rho_{\rm crit} \equiv \frac{3H_0^2}{8\pi G} = 1.88h^2 \times 10^{-29}\mathrm{g/cm^3} \quad . \tag{2.12}$$

[1] Indeed this is derived simultaneously with Eq. (2.6).

Eq. (2.7) for the present condition (taking $a(t_0) = 1$) yields

$$\Omega_R + \Omega_M + \Omega_k + \Omega_\Lambda = 1 \quad . \tag{2.13}$$

Here, the present state of the universe is interesting to know. (1) The curvature is considered to be nearly flat, so $\Omega_k \sim 0$. (2) Relativistic matter contains photons and $N_\nu = 3$ neutrinos, the density parameter of which is negligibly small $\Omega_{\mathrm{R}} \sim 10^{-5}$. (3) Non-relativistic matter contains baryons and cold dark matter (CDM), the density parameter of which is deduced to $\Omega_{\mathrm{M}} \sim 0.3$ (including the baryonic contribution $\Omega_{\mathrm{b}} \sim 0.05$) based on the measurement of the CMB radiation. This surprisingly implies that almost over 80% of the non-relativistic matter component is dominated by unknown CDM. Furthermore, the universe is mostly composed of another unknown matter, (4) The dark energy whose density parameter is $\Omega_\Lambda \sim 0.69$.

2.1.2 Thermal History of the Early Universe

Temperature transition plays an important role in BBN and also in the theoretical prediction. It is interesting and convenient to introduce the relation between temperature, time and the scale factor a through the thermal history of the early universe when it was in sufficiently hot and dense state. The temperature under consideration here starts from $T > 10^{11}$ K corresponding to the energy scale of about $k_B T > 10$ MeV (Note that the temperature T denotes the photon temperature T_γ). At this early stage when $a \ll 1$, the universe was totally dominated by the relativistic matters which were in equilibrium. Therefore, in Eq. (2.7), the curvature k, vacuum energy Λ, and non-relativistic matter ρ_M are neglected, and the equation yields

$$H^2(t) \equiv \left(\frac{\dot{a}}{a}\right)^2 = \frac{8\pi G \rho_{\mathrm{R}}}{3} \quad . \tag{2.14}$$

When integrating both sides with cosmic time t, the relation between the scale factor and time can be found as

$$a \propto \sqrt{t} \quad . \tag{2.15}$$

As follows, the conservation of entropy is considered: The expansion of the universe is considered adiabatic, and this requires that the total entropy $s(T)$ stay constant, i.e.

$$s(T)a^3 = \text{constant} \quad , \tag{2.16}$$

where the entropy is written by considering the thermodynamics as

$$s(T) = \frac{\rho(T) + P(T)}{T} \quad . \tag{2.17}$$

The same as in the Friedmann equation, the thermodynamics can be described in terms of only relativistic matters with $m \ll k_B T$. Namely, photons, e^--e^+ and $N_\nu = 3$ species of neutrinos and anti-neutrinos are considered in order to deduce thermodynamic quantities. The number density $n(p)\mathrm{d}p$ of these species of fermions or bosons with mass m and momentum between p and $p + \mathrm{d}p$ is given by Fermi-Dirac or Bose-Einstein distributions

$$n(p, T) = \frac{g}{2\pi^2 \hbar^3} \frac{p^2}{\exp\left(\frac{\sqrt{p^2+m^2}-\mu}{k_B T}\right) \pm 1} \quad , \tag{2.18}$$

where g is the spin degree of freedom of particles and anti-particles (e.g. $g = 1$ for neutrinos, $g = 2$ for photons, and $g = 4$ for electron-positron pairs), and μ is the chemical potential. The positive $(+)$ and negative $(-)$ signs are for fermions and bosons, respectively. The mass-energy density and the pressure are then given by the integrals

$$\rho(T) = \int_0^\infty n(p,T)\sqrt{p^2+m^2}dp \quad , \tag{2.19}$$

and

$$P(T) = \int_0^\infty n(p,T)\frac{p^2}{3\sqrt{p^2+m^2}}dp \quad . \tag{2.20}$$

By inserting these equations into Eq. (2.17), the entropy can be deduced. For highly relativistic condition in which m and μ can be neglected compared to the temperature, the mass-energy density and the entropy can be deduced from the integrals to

$$\rho(T) = \frac{\pi^2 k_B^4}{30\hbar^3} g_* T^4 \quad , \tag{2.21}$$

$$s(T) = \frac{2\pi^2 k_B^4}{45\hbar^3} g_{*s} T^3 \quad , \tag{2.22}$$

where g_* and g_{*s} are the total spin degree of freedom defined as

$$g_* = \sum_B g_B (\frac{T_B}{T})^4 + \sum_F \frac{7}{8} g_F (\frac{T_F}{T})^4 \quad , \tag{2.23}$$

$$g_{*s} = \sum_B g_B (\frac{T_B}{T})^3 + \sum_F \frac{7}{8} g_F (\frac{T_F}{T})^3 \quad , \tag{2.24}$$

with notations B and F corresponding to boson and fermion, respectively. Thus, if $T_F = T_B = T$, such an environment in which all species are in equilibrium with a common temperature, the conservation law of entropy, Eq. (2.16), requires

$$s(T)a^3 \propto T^3 a^3 = \text{constant.} \tag{2.25}$$

This demonstrates the fact that the temperature decreases inversely proportional to the scale factor as

$$T \propto \frac{1}{a} \quad , \tag{2.26}$$

and thus the relation between the time and temperature can be found together with Eq.(2.15) as

$$t \propto \frac{1}{T^2} \quad . \tag{2.27}$$

Following the derivations above, the relation between the temperature and the cosmic scale factor, and furthermore the time is to be deduced through the thermal history, depending on the relativistic components of the universe.

- At 10^{10} K$\leq T \leq 10^{11}$ K, corresponding to $\sim$1 MeV$\leq k_B T \leq \sim$10 MeV, all relativistic matters, namely photons, e^--e^+ pairs, $N_\nu = 3$ neutrinos and anti-neutrinos are tightly coupled through electromagnetic and weak interactions: The interaction rates are short enough compared with the expansion rate ($\Gamma_{EM}, \Gamma_{weak} \gg H$), so that all species are in equilibrium with a common temperature T. The

TABLE 2.1: Temperature deviation of neutrino from photon after decoupling. The temperature of $T = 10^{11}$ K is set to the initial point.

T (K)	T/T_ν	t (sec)
10^{11}	1.000	0
6×10^{10}	1.000	0.0177
3×10^{10}	1.001	0.101
2×10^{10}	1.002	0.239
10^{10}	1.008	0.998
6×10^{9}	1.022	2.86
3×10^{9}	1.080	12.66
2×10^{9}	1.159	33.1
10^{9}	1.345	168
3×10^{8}	1.401	1980
10^{8}	1.401	1.78×10^{4}
10^{7}	1.401	1.78×10^{6}
10^{6}	1.401	1.78×10^{8}

spin degree of freedoms are then obtained from Eq. (2.23) and Eq.(2.24) as

$$\begin{aligned} g_{*s} = g_* &= g_\gamma + \frac{7}{8}(g_e + g_\nu) \\ &= 2 + \frac{7}{8}(4 + 2 \times 3) = 10.75 \quad . \end{aligned} \tag{2.28}$$

This leads to the relation between the cosmic time and the temperature

$$t \sim 1 \text{ sec} \left[\frac{\mathrm{T}}{10^{10}\mathrm{K}} \right]^{-2} \quad . \tag{2.29}$$

- At $T \simeq 10^{10}$K, corresponding to $k_B T \simeq 1$ MeV, neutrinos are nearly full-decoupled from other species so that their entropy is conserved separately. Hence their temperature T_ν starts deviating from T. After the e^--e^+ annihilation which will be discussed in the next item, the ratio of T to T_ν converges to $T/T_\nu = (11/4)^{1/3} = 1.401$. The transition of the temperature ratio, and the time required for the temperature to drop from 10^{11} K are available in Table 2.1 which is adopted from the textbook of Weinberg [2].

- At 10^8 K$\leq T \leq 10^{10}$ K, corresponding to approximately 0.01 MeV$\leq k_B T \leq 1$ MeV, e^--e^+ pairs start annihilating and almost all of them are converted into photons (leaving the same tiny amount of electrons as protons to keep the electric neutrality of the universe). Since neutrinos are already fully decoupled at this time, whole entropy of the e^--e^+ pairs is transferred to photons: By neglecting the tiny remnants of electrons, the conservation of entropy before and after the annihilation is expressed as

$$\begin{aligned} & (\frac{7}{8} \times g_e + g_\gamma) T_{\text{before}}^3 = g_\gamma T_{\text{after}}^3 \\ \leftrightarrow \quad & (\frac{7}{8} \times 4 + 2) T_{\text{before}}^3 = 2 T_{\text{after}}^3 \\ \leftrightarrow \quad & T_{\text{before}} = (\frac{4}{11})^{1/3} T_{\text{after}}. \end{aligned} \tag{2.30}$$

On the other hand, the entropy of neutrinos is conserved separately and the conservation is expressed as

$$T_\nu = T_{\text{before}} = (\frac{4}{11})^{1/3} T_{\text{after}}. \tag{2.31}$$

Consequently, after e^-- e^+ annihilation the spin degree of freedoms yield

$$\begin{aligned} g_* &= g_\gamma + \frac{7}{8} g_\nu (\frac{T_\nu}{T})^4 \\ &= 2 + \frac{7}{8} \times 2 \times 3 \times (\frac{4}{11})^{4/3} \simeq 3.363 \quad , \end{aligned} \tag{2.32}$$

and

$$\begin{aligned} g_{*s} &= g_\gamma + \frac{7}{8} g_\nu (\frac{T_\nu}{T})^3 \\ &= 2 + \frac{7}{8} \times 2 \times 3 \times \frac{4}{11} \simeq 3.909 \quad . \end{aligned} \tag{2.33}$$

This leads to the relation between the cosmic time and the temperature,

$$t \sim 1.78 \text{ sec} \left[\frac{\mathrm{T}}{10^{10} \mathrm{K}} \right]^{-2} \quad . \tag{2.34}$$

In this period, electrons gradually become non-relativistic as the temperature falling to $k_B T \leq m_e$. While photons, neutrinos and anti-neutrinos are fully decoupled, only electrons are coupled with photons by interacting effectively and exchanging energy of the order of $(k_B T)^2 / m_e$ until the temperature drops to $\sim 10^5$ K. After that, they just elastically scatter each other.

- At any moment in the thermal history, the energy spectrum of photon keeps the form of Eq. (2.18) with $m = \mu = 0$, $g = 2$ and $p = h\nu$, where ν is the frequency,

$$n(T, \nu) d\nu = \frac{8\pi \nu^2 d\nu}{\exp\left(\frac{h\nu}{k_B T}\right) - 1} \quad . \tag{2.35}$$

This expression is called Planck spectrum or the black-body spectrum. Around $T = 10^4$ K, the contribution of non-relativistic matter to the cosmic mass-energy density becomes equal or larger than that of relativistic matter. From this point, the universe is referred as the matter-dominated universe. Furthermore, as the universe keeps expanding and cooling, when the temperature drops down to around $3,000$ K, electrons are bound to nuclides (recombination epoch). Therefore, electrons do not scatter anymore with photons, which is referred as the last scattering when the universe finally become transpicuous and photons start traveling freely and expanding, while energy spectrum keeps the form of Eq. (2.35). These photons are so-called CMB radiation [3] with $T = 2.725 \pm 0.002$ K which is the measurable oldest light.

2.1.3 Nucleosynthesis

BBN occurs in the environment of expanding and cooling universe such that properties are governed by the Friedmann equation and the thermodynamics described so far. The temperature under consideration is from 10^{10} K down to few 10^8 K, which

corresponds to the descriptions of the first three items of the previous subsection. Regarding the radiation-dominant epoch, the number of baryons (proton and neutron) was very tiny compared to photons. Thus, the nuclear reaction rate depends crucially on their relative number density which is given by

$$\eta = \frac{n_b}{n_\gamma} \quad , \tag{2.36}$$

and this η is in principle the only free parameter in the BBN calculation. There are only thirteen reactions considered important in the reaction networks during the BBN period as shown in Fig. 2.1. In this section, the history of the synthesis of various light elements will be explained along with the thermal conditions described in the previous section. In the following, the number density distribution at temperature T for a non-relativistic particle i takes the Maxwell-Boltzmann expression

$$n_i = g\left(\frac{m_i}{2\pi k_B T}\right)^{\frac{2}{3}} \exp\left(-\frac{m_i - \mu_i}{k_B T}\right) \quad . \tag{2.37}$$

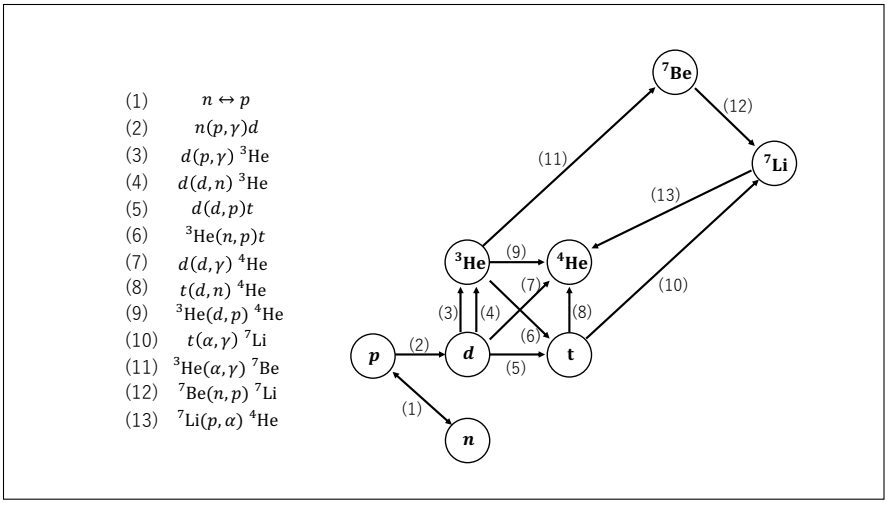

FIGURE 2.1: BBN reaction network. Only these 13 reactions are considered important.

- At $T \geq 10^{10}$ K, corresponding to $k_B T \geq 1$ MeV, the weak interactions listed below are in equilibrium since they occur rapidly enough compared to the expansion rate ($\Gamma_{weak} > H$):

$$\begin{aligned} p + e^- &\leftrightarrow n + \nu_e \\ p + \bar{\nu}_e &\leftrightarrow n + e^+ \end{aligned} \quad , \tag{2.38}$$

  thus the chemical potential is conserved as $\mu_p + \mu_e = \mu_n + \mu_{\nu_e}$. In this equilibrium the ratio of proton and neutron number densities is given by

$$\frac{n_n}{n_p} \sim \exp\left(-\frac{Q}{k_B T}\right) \quad , \tag{2.39}$$

where $Q = 1.293$ MeV which is the mass difference between neutron and proton. At very high temperature $k_B T \gg 1$ MeV the ratio is $n_n/n_p = 1$. As the temperature decreases, weak interaction rate gradually becomes equal to or slower than the expansion rate, resulting the processes being frozen at $k_B T \simeq 0.8$ MeV. The number density ratio at this time is fixed to $n_n/n_p \simeq 1/6$. Furthermore, after this freeze-out, free neutrons decay to protons with the mean lifetime of about $\tau_n = 880.2$ sec [4], and the ratio becomes $1/7$ at the time when the nucleosynthesis sufficiently starts around $k_B T = 0.1$ MeV.

- Deuterons (d) start being synthesized first through the $n(p,\gamma)d$ reaction. Since the binding energy, an amount representing the stability of nuclei, is 2.2 MeV the synthesis can begin from the time when the temperature is still high, even around $T = 10^{10}$ K (and thus $k_B T = 1$ MeV). However, it is $k_B T \leq 0.07$ MeV when the production is considered to begin sufficiently, and this period is referred as the time when the deuteron-bottleneck opens. The reason of this late beginning of synthesis is that there are plenty of photons in the *tale* part of the Planck distribution given in Eq.(2.35), which have higher energy than the binding energy to cause photodissociation. As soon as the bottleneck opens, other formations of light-elements, such as triton (t), ^{3}He, ^{4}He and so on occur rapidly through those reactions shown in Fig. 2.1. The synthesis of mass number $A = 3$ are namely,

$$\begin{aligned} &d(d,p)t, \qquad d(p,\gamma)^3\mathrm{He}, \\ &d(d,n)^3\mathrm{He}, \quad {}^3\mathrm{He}(n,p)t, \end{aligned}$$

followed by the ^{4}He production

$$t(d,n)^4\mathrm{He}, \qquad d(d,\gamma)^4\mathrm{He}, \qquad {}^3\mathrm{He}(d,p)^4\mathrm{He} \quad .$$

Since ^{4}He has the highest binding energy per nucleon among all isotopes lighter than carbon, most neutrons are incorporated into ^{4}He formation. In the ultimate case that all neutrons are consumed for ^{4}He, the mass fraction of ^{4}He is simply given by

$$Y_p = \frac{(2m_n + 2m_p)\cdot n_n/2}{m_n n_n + m_p n_p} \simeq \frac{2\frac{n_n}{n_p}}{\frac{n_n}{n_p}+1} = \frac{2\cdot\frac{1}{7}}{\frac{1}{7}+1} = 0.25 \quad , \tag{2.40}$$

which is closely consistent with the deduced value from observations, $Y_p = 0.2449 \pm 0.004$ [5]. The synthesis of heavier elements are regulated because of (1) the absence of stable nuclei with mass number $A = 5$ and 8, and of (2) the large Coulomb barriers for the reactions between charged particles. The important reactions for the formation of ^{7}Li and ^{7}Be are

$$t(\alpha,\gamma)^7\mathrm{Li}, \qquad {}^3\mathrm{He}(\alpha,\gamma)^7\mathrm{Be}, \qquad {}^7\mathrm{Be}(n,p)^7\mathrm{Li} \quad .$$

However, one must note that most of the produced ^{7}Li during the BBN period is destroyed immediately by the following reaction:

$${}^7\mathrm{Li}(p,\alpha)^4\mathrm{He} \quad .$$

2.2 BBN Calculation Reveals the Lithium Problem

On the basis of the discussion so far, the following two aspects should be emphasized in the BBN calculation:

1. It is based on well-established theories.
2. Only a relatively small number of nuclear reactions are considered important.

It is the time (thus temperature) evolution of the abundances of light elements which is of interest in the practical calculation. For the nucleosynthesis under consideration here, it is assumed that only two-body reactions, $i + j \leftrightarrow k + l$, occur since the number density of baryons or nuclei is tiny in the early epoch[2]. For a nuclide i, then, the abundance evolution is expressed in terms of the number fraction $Y_i = n_i/n_b$ as

$$\dot{Y}_i = \sum_{j,k,l} N_i \left(\Gamma_{kl\to ij} \frac{Y_l^{N_l} Y_k^{N_k}}{N_l! N_k!} - \Gamma_{ij\to kl} \frac{Y_i^{N_i} Y_j^{N_j}}{N_i! N_j!} \right) \quad , \tag{2.41}$$

where N_i is the number of reacting particles. $\Gamma_{kl\to ij}$ is the reaction rate of the $k + l \to i + j$ reaction given by

$$\Gamma_{kl\to ij} = n_b \langle \sigma v \rangle_{kl\to ij} \quad , \tag{2.42}$$

where, the thermally averaged reaction cross section $\langle \sigma v \rangle_{kl\to ij}$ is written as

$$\langle \sigma v \rangle_{kl\to ij} = \int_0^\infty \sigma(v)\, \phi_{\mathrm{MB}}(v)\, v dv \tag{2.43}$$

with the Maxwell-Boltzmann distribution

$$\phi_{\mathrm{MB}}(v)\, v dv = \sqrt{\frac{8}{\pi\mu}} \frac{1}{(k_B T)^{3/2}} e^{-\frac{E}{k_B T}} E dE \quad . \tag{2.44}$$

As can be seen obviously in the equations above, precise information of the reaction cross sections at the relevant energy to the BBN scale are necessary for the calculation in the first place. The nuclear cross sections propagate the uncertainties directly to the final predictions. Neutron lifetime τ_n also plays a key role for the synthesis since it controls the neutron-proton ratio, and neutrons are also important source of nuclear reactions in the absence of Coulomb barriers. As well as such direct influences, the number of neutrino family may affect the spin degree of freedom defined in the thermal history, thus the expansion rate of the universe or the temperature transition may differ. However, such quantities, in turn, have been the cornerstones of the BBN calculation with substantial precision after the thorough investigations in the past [6, 7]. Thus, the BBN calculation is able to include them just as physical inputs with certain knowledge of their uncertainties.

In the Fig. 2.2 adopted from the published paper by Coc [8], the abundance predictions for deuteron (D), ^{3}He, ^{4}He and ^{7}Li as functions of η are shown with blue curves. The errors in the abundance curves come mainly from the uncertainties in the thermonuclear reaction rates. Note that ^{7}Li abundance is plotted as a sum of ^{7}Li and ^{7}Be abundances, since ^{7}Be decay into ^{7}Li long after the BBN ceases. Similarly, tritons decay to ^{3}He, thus the sum of both is plotted in the figure for ^{3}He.

[2] Even including the three-body reactions, it does not have much effect on each of the final abundance predictions.

Meanwhile, the green bands in the figure represent the corresponding observed abundances. Observations are done on the metal-poor objects in general. The deuterium abundance has been determined from the observation on the high-redshift clouds for Lyman-α spectrum in the light emission from high-redshift quasars, and the most recent value is deduced to $\mathrm{D/H} = (2.53 \pm 0.04) \times 10^{-5}$ [9]. The ^{4}He abundances are deduced from the observation on metal-poor stars in the $\mathrm{H_{II}}$ region. The value has been determined by Aver *et al.* to $Y_p = 0.2449 \pm 0.004$. The ^{3}He abundance is reported as $^3\mathrm{He/H} = (0.9\text{-}1.3) \times 10^{-5}$ [10]. Finally, the ^{7}Li abundance has been measured in extremely metal-poor stars and in low-metallicity MS stars. The value is deduced to $^7\mathrm{Li/H} = (1.58 \pm 0.3) \times 10^{-10}$ [11].

In the beginning of this 21st century, the measurement on the CMB radiations brought a breakthrough to the interpretation of the BBN calculation results: the value of the sole free parameter η, which can be rewritten as $\eta = 2.74 \times 10^{-8}\Omega_\mathrm{b}h^2$ in terms of the baryonic density parameter Ω_b, has been deduced precisely. There are two noteworthy observations by WMAP and Planck missions. From the most recent measurement by the Planck Surveyor [12], the baryonic density parameter has been found to $\Omega_\mathrm{b}h^2 = 0.02225 \pm 0.00016$, and thus η has been deduced. This value is implemented directly into the BBN calculation and it corresponds to the crossing vertical yellow line in the Fig. 2.2. Therefore, the BBN calculation has no free parameter anymore, and a comparison for each light element can be performed explicitly.

It is found that there is a great agreement for deuterium (D) abundance, and fine agreements for ^{3}He, ^{4}He abundances. These quantitative concordances represent a great success of the standard Big Bang Model. However, it appears that only for ^{7}Li, the abundance predicted by the BBN calculation is overestimated by a factor of three to four. A quick look for the comparison for the abundances is adopted directly from the paper published by Coc et al. [8] which is given in the Table. 2.2.

TABLE 2.2: Comparison between the predicted abundance and the observed abundance of several light elements (D, ^{3}He, ^{4}He and ^{7}Li) adopted from the paper of Coc *et al.* [8].

	Prediction	Observasions	Ref. Obs.
D/H	$(2.45 \pm 0.05) \times 10^{-5}$	$(2.53 \pm 0.04) \times 10^{-5}$	[9]
^{3}He$/H$	$(1.07 \pm 0.03) \times 10^{-5}$	$(0.9 - 1.3) \times 10^{-5}$	[10]
^{4}He	0.2484 ± 0.0002	0.2449 ± 0.0040	[5]
^{7}Li$/H$	$(5.61 \pm 0.26) \times 10^{-10}$	$(1.58 \pm 0.31) \times 10^{-10}$	[11]

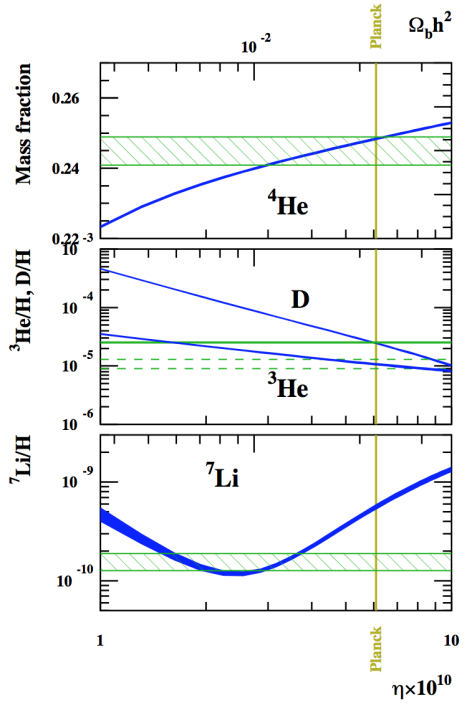

FIGURE 2.2: BBN calculation by Coc *et al.*[8] Blue curve and green area, respectively, correspond to the predicted abundance and the observed abundance of light elements. The vertical yellow line across the figure denotes the baryon-to-photon ratio η deduced by the Planck mission to measure the CMB anisotropy.

2.3 Role of ^{7}Be Abundance in the Lithium Problem

In Fig. 2.3 [13], time evolutions of light-element abundances are shown when the deduced baryon-to-photon ratio is implemented in the calculation. The horizontal axis corresponds to the temperature, and thus the cosmic time. The vertical axis is the relative abundances of light elements with respect to proton (H). Both axises are arranged in logarithmic scale. Among the light elements the notation Y_p denotes the mass fraction of ^{4}He.

To approach the lithium problem, the ^{7}Li abundance evolution has to be looked carefully. In Fig. 2.3, it can be seen that although there is a rapid synthesis of ^{7}Li mainly by the $t(\alpha, \gamma)^7$Li reaction which starts from the time at $T \sim 0.1$ MeV, most

of the products are destroyed immediately. This is mostly due to the reaction of $^7\mathrm{Li}(p,\alpha)^4\mathrm{He}$, resulting the bump near the time at $k_BT = 0.08$ MeV. Consequently, during the BBN period ^{7}Li is created roughly of the order of $^7\mathrm{Li/H} \sim 10^{-11}$, which is somewhat smaller than observed abundance, $(^7\mathrm{Li/H})_{obs} = (1.58 \pm 0.3) \times 10^{-10}$. However, there is another production process which enhances ^{7}Li abundance as mentioned before: ^{7}Be synthesized during the BBN period decays to ^{7}Li through electron-capture decay after BBN ceases. At the time when BBN freezes out, the abundance of ^{7}Be is more than a factor of 10 larger than that of ^{7}Li. Thus, the most dominant contribution to the final abundance of ^{7}Li comes from the abundance of ^{7}Be synthesized in BBN. This contribution may cause the overestimation in the theoretical prediction for the ^{7}Li abundance as shown in the Fig. 2.2.

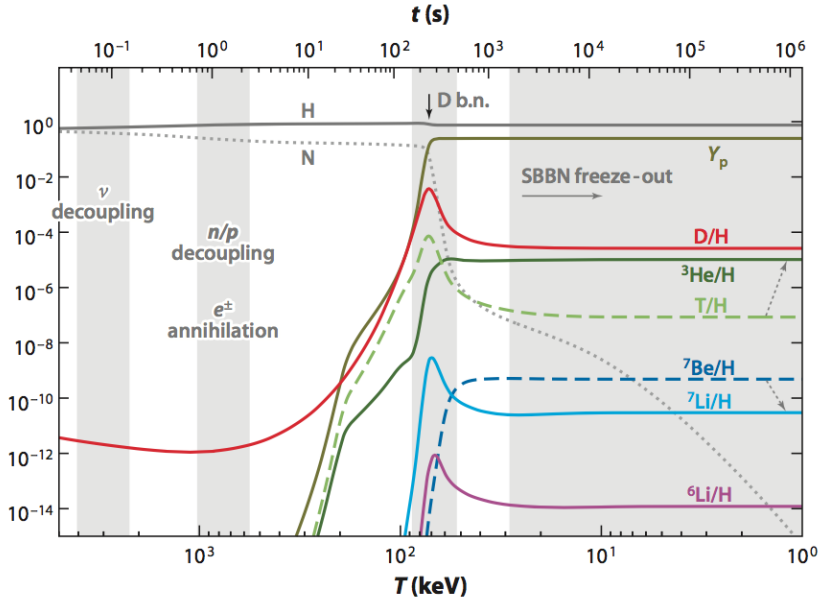

FIGURE 2.3: Time (temperature) evolution of the light-element abundances [13]. Y_p is the mass fraction of ^{4}He. "D b.n." denotes the time when the *deuteron bottleneck* opens. The dot-arrows represent the decay directions of T and ^{7}Be into ^{3}He and ^{7}Li, respectively.

2.4 Investigation on Possible Solutions

Inspired by the fact discussed in the previous section, one may have an idea that the lithium problem may be solved if any scenarios happened which decreases the abundance of ^{7}Be during the BBN period. From the perspective of nuclear physics, this implies that the cross sections for either productive or destructive reactions of ^{7}Be implemented in the BBN calculation do not satisfy the actual situation, so that they have to be revised or any other unknown reactions, such as resonances to destroy ^{7}Be, have to be explored.

Regarding this approach, there are mainly three important nuclear reactions which have been investigated thoroughly. First, the $^3\mathrm{He}(\alpha,\gamma)^7\mathrm{Be}$ reaction is the dominant channel for the production of ^{7}Be. This reaction has got a great deal of attention as a key information to predict the solar neutrino spectra, which drove many experimental and theoretical works to obtain the cross section in the past. As a result of comparing the approaches from both nuclear physics and astronomy sides, it was

found that there is no possibility to solve the lithium problem through this channel [14].

For the destruction process, the neutron-induced reactions play the most important role during BBN. The $^{7}\mathrm{Be}(n,\alpha)^{4}\mathrm{He}$ reaction is of the secondary importance whose branching ratio occupies about 2.5 % for the BBN scale. Due to the scarce of experimental data and analysis, the implemented reaction rate was determined based on Wagoner's estimation presented in 1969 [15]; even though a large uncertainty might be assumed in it. In addition, the estimation considered only the direct reaction contribution, thus the resonant contribution was not implemented. Recently, the cross section has been revised by the measurement of inverse reaction using detailed balance, in specific the $^{4}\mathrm{He}(\alpha,n)^{7}\mathrm{Be}$ reaction, by Kubono *et al.* [16]. Their result, however, showed a lower reaction rate compared to Wagoner's. Also, the reaction has been also studied by the direct reaction measurement performed at the n_TOF facility, CERN [17] and by the time reversal reaction measurement at RCNP, Osaka University [18]. These researches have been excluded the possibility to solve the lithium problem from this channel.

The third reaction is the $^{7}\mathrm{Be}(n,p)^{7}\mathrm{Li}$ reaction which is of the primary interest in this thesis. This reaction plays the most important role in the destruction process since the branching ratio is about 95 % for the BBN scale. It seems to enhance the $^{7}\mathrm{Li}$ abundance, however, almost all of $^{7}\mathrm{Li}$ are destroyed immediately by the $^{7}\mathrm{Li}(p,\alpha)^{4}\mathrm{He}$ reaction during the BBN period, that is, the reaction rate of the $^{7}\mathrm{Be}(n,p)^{7}\mathrm{Li}$ reaction is much slower than that of the $^{7}\mathrm{Li}(p,\alpha)^{4}\mathrm{He}$ reaction at the relevant energy to the BBN scale [19]. The details of this reaction will be discussed in the next chapter for clarifying the purpose of our experiment.

Chapter 3

Motivation and Purpose

In Chapter 2, it was suggested that if ^{7}Be abundance, the main source of ^{7}Li after BBN ceases, decreased during the BBN period the cosmological lithium problem may be solved. In this chapter, the possibility of the primarily important reaction for the destruction process, namely the $^7\mathrm{Be}(n,p)^7\mathrm{Li}$ reaction, to solve the problem will be discussed.

3.1 $^7\mathrm{Be}(n,p)^7\mathrm{Li}$ reaction

Figure 3.1 shows the level scheme of the $^7\mathrm{Be}(n,p)^7\mathrm{Li}$ reaction given in the unit of MeV. At the BBN energy scale, the excited states of ^{8}Be surrounded by the red dashed-line are considered to be populated. Γ is the total width of each excited state, as well as Γ_n and Γ_p are the partial widths of neutron and proton channels, respectively. The properties, such as the spin-parity and the level/partial widths, of the excited states are listed in Table 3.1 [20, 21].

There are only a few direct measurements on this reaction performed in the past, because of the difficulty in the treatment of the radioactive ^{7}Be sample which can be a large background in an experiment. Hanna [22] measured for the first time the cross section near the reaction threshold using a thermal neutron beam extracted from the BEPO reactor. However, in the result a relatively large uncertainty of about 15 % is a point of concern. Koehler *et al.* [23] measured the total cross section in the energy range from thermal to 13.5 keV neutron energy as shown in Fig. 3.2. They also succeeded in separating the p_0 group and the p_1 group, the decay branches in the outgoing channel from ^{8}Be to the ground state and the first excited state of ^{7}Li, respectively, near the 2^- (18.91 MeV) resonance peak. The cross section ratio between the p_1 group and p_0 group was reported to $\sigma_{p_1}/\sigma_{p_0} = (1.0 \pm 0.3)\%$ at the thermal energy. Their result was also in agreement with the other measurement [24], and they concluded that the weighted mean of the cross section ratio for the entire energy range of their experiment was $\sigma_{p_1}/\sigma_{p_0} = 0.0118 \pm 0.0005$. Recently, another direct measurement was performed at the n_ToF facility, CERN for the energy range up to 325 keV [20]. The cross section data showed 35% higher than that of the prior result [23] at low energy. However, the contribution of the $^7\mathrm{Be}(n,p_1)^7\mathrm{Li}^*$ reaction could not be evaluated separately in their measurement.

Meanwhile, the cross section has also been deduced based on the inverse reaction, the $^7\mathrm{Li}(p,n)^7\mathrm{Be}$ reaction, using detailed balance. This inverse reaction has been a great use as the source of neutron beam for *e.g.* calibrating nuclear reactors. Therefore, many experiments have been performed to investigate the cross section for wide energy and angular domains. Some experimental data of the total cross section as a function of proton energy are compiled in the Fig. 3.3 [25–27]. In the paper

published by Liskien and Paulsen in 1975 [28], plenty of such experimental data on the cross sections are compiled, and furthermore they derived the best values for the Legendre coefficients based on the experimental differential cross sections. Such substantial works allowed to study the nuclear structure and to evaluate the cross section of the $^{7}\mathrm{Be}(n, p_0)^{7}\mathrm{Li}$ reaction at relevant energies to the BBN scale. However, one must notice that the cross section of the $^{7}\mathrm{Be}(n, p_1)^{7}\mathrm{Li}^{*}(0.478\mathrm{MeV})$ reaction cannot be derived from the inverse reaction measurement.

As a conclusion, since the relevant energy is considered up to about $E_n = 2$ MeV, investigation on the cross section of the $^{7}\mathrm{Be}(n, p_1)^{7}\mathrm{Li}^{*}$ reaction is required.

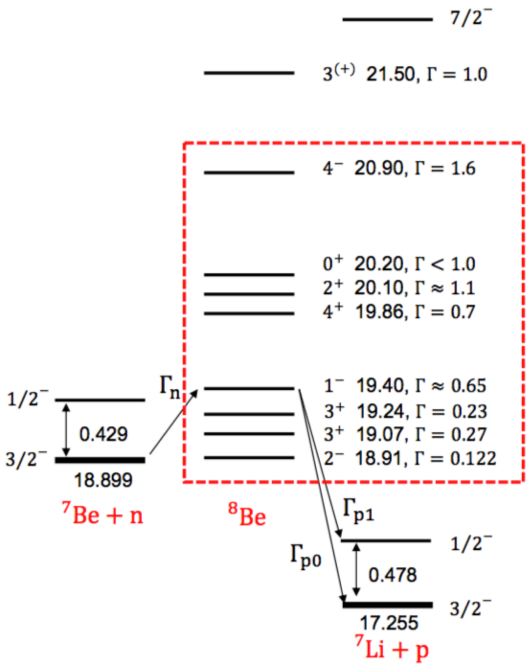

FIGURE 3.1: The level scheme of the $^{7}\mathrm{Be}(n, p)^{7}\mathrm{Li}$ reaction in MeV. Excited states of ^{8}Be surrounded by the red-dashed line are considered to be populated in the BBN scale. Partial width of proton decays are denoted by Γ_{p0} andΓ_{p1} corresponding to the decay destinations.

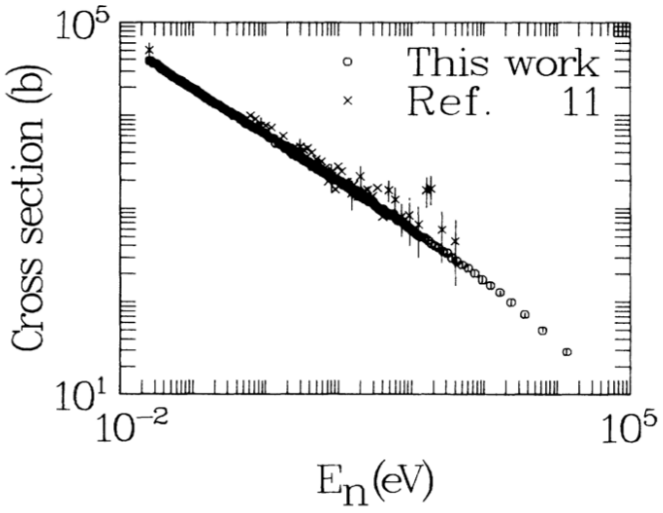

FIGURE 3.2: The ^{7}Be(n,p) reaction cross section data measured by Koehler et al.[23] ("This work") and Glendenov et al ("Ref.11").

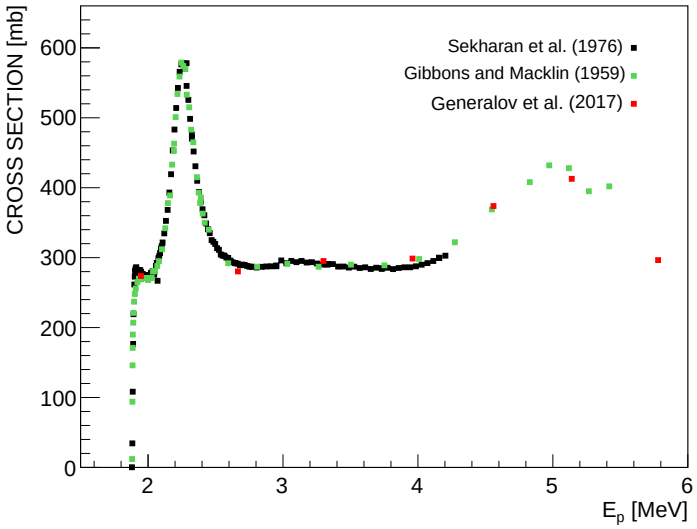

FIGURE 3.3: The total cross section of the ^{7}Li$(p,n)^7$Be reaction. Experimental data are adopted from the papers of Sekharan [25], Gibbons [26] and Generalov [27]. A rapid increase can be seen just above the reaction threshold ($E_{th} \sim 1.88$ MeV), which is due to the 18.91 MeV (2^-) resonance, followed by the main peak near $E_p = 2.3$ MeV due to the 19.24 MeV (3^+) resonance.

3.2 The ^{9}Be$(^3$He$,\alpha)^8$Be$^*(p)^7$Li reaction

For a single resonance channel in the ^{7}Be$(n,p)^7$Li reaction, the cross section is given by the (single level) Breit-Wigner expression [29]

$$\sigma_{(n,p)}(E_n) = \frac{\lambda_n^2}{4\pi} \sum g(J) \frac{\Gamma_n \Gamma_p}{(E_n - E_R)^2 + \Gamma^2/4} \quad , \tag{3.1}$$

TABLE 3.1: List of the property of ^{8}Be excite states [20, 21].

I^π	E_X [MeV]	Γ [MeV]	Γ_p [MeV]	Γ_n [MeV]	Γ_α [MeV]
2^+	16.626	0.11	0.000	0.000	0.110
2^+	16.922	0.074	0.000	0.000	0.074
1^+	17.64	0.011	0.011	0.000	0.000
1^+	18.15	0.138	0.138	0.000	0.000
2^-	18.91	0.122	0.061	0.061	0.000
3^+	19.07	0.27	0.271	0.001	0.000
3^+	19.235	0.227	0.114	0.114	0.000
1^-	19.4	0.645	0.320	0.320	0.000
4^+	19.86	0.7	0.210	0.001	0.490
2^+	20.1	0.88	0.127	0.100	0.573
0^+	20.2	0.72	0.150	0.150	0.360
4^-	20.9	1.6	0.800	0.800	0.000

where J is the statistical spin degree, λ_n is the wave length of the entrance channel, E_R is resonant energy. For the inverse reaction, the symbol n is replaced by p. Both Γ_n and Γ_p can be given in the energy dependent expression with reduced width γ_r and penetrability factor P_l as

$$\Gamma_{n(p)} = 2P_l\gamma_r^2 \quad . \tag{3.2}$$

The penetrability factor is given by

$$P_l = \frac{kR}{F_l(kR,\eta)^2 + G_l(kR,\eta)^2} \quad , \tag{3.3}$$

where F_l and G_l are the regular and irregular Coulomb functions, respectively, and η is the Sommerfeld parameter.

The wealth of data of the ^{7}Li$(p,n)^7$Be reaction provides the information of the partial widths Γ_n and Γ_{p0} for each of the excited states of ^{8}Be. In addition, the application of the reciprocity theorem to the cross sections provides the cross sections of the inverse ^{7}Be$(n,p_0)^7$Li reaction. Therefore, if the branching ratio of Γ_{p1}/Γ_{p0} is determined for each resonance state of ^{8}Be, the cross section of the ^{7}Be$(n,p_1)^7$Li$^*(0.478$ MeV$)$ reaction can be deduced.

This is the goal of our experiment: to measure the ^{9}Be$(^3$He$,\alpha)^8$Be$^*(p)^7$Li reaction. The interesting resonance states of ^{8}Be can be populated by the ^{9}Be$(^3$He$,\alpha)^8$Be reaction whose excitation energy can be deduced by measuring the magnetic rigidity of scattering α particle. A measurement of the kinetic energy of decay protons provides the information of the ^{7}Li state. In addition, a measurement of angular distribution will provide the information of the spin-parity state of each ^{8}Be and ^{7}Li nuclei. The experimental aspects will be described more from the next chapter.

3.3 Expected Enhancement

An investigation on the influence of the ^{7}Be$(n,p_1)^7$Li$^*(0.478\,$MeV$)$ reaction to the ^{7}Li + ^{7}Be abundance in the BBN calculation was performed with the PArthENoPE code developed by INFN in Italy [30, 31]. The implemented conditions are following:

- Neutron lifetime $\tau_n = 880.2$ sec
- Number of neutrino family $N_\nu = 3$
- $\Omega_b h^2 = 0.02225$
- Number of nuclide considered = 9 : n, p, D, T, ^{3}He, ^{4}He, ^{6}Li, ^{7}Li, ^{7}Be
- Number of reaction considered = 40

To know the expected enhancement of the reaction rate to solve the lithium problem, the present reaction rate implemented in the BBN calculation was multiplied by a constant. The Fig. 3.4 shows the result. The abundance, the red points on the figure, decreases with respect to the increase of factor, and it matches with the observed value when the factor is about three to four. This demonstrates that if the reaction rate of the $^7\mathrm{Be}(n, p_1)^7\mathrm{Li}^*(0.478\ \mathrm{MeV})$ reaction is just two or three times larger than that of present, the lithium problem may be solved. Furthermore, the transition of D, ^{4}He and ^{7}Li abundances are shown before (left) and after (right) the multiplication by a factor of 3.5 in Fig. 3.5. The yellow bands correspond to the observed values. This figure confirms that the multiplication of the reaction rate does not influence other abundances.

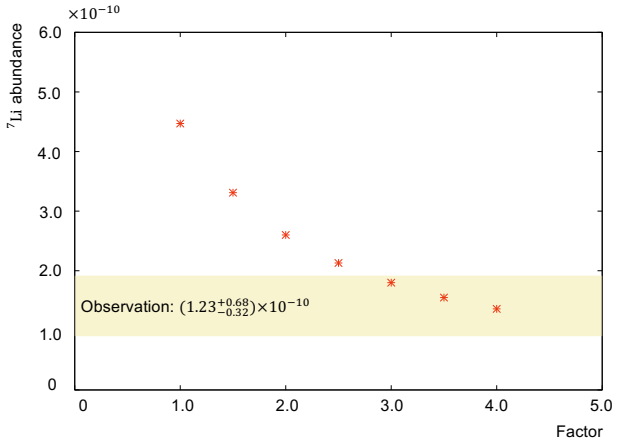

FIGURE 3.4: Transition of ^{7}Be abundance with respect to the multiplication factor of the $^7\mathrm{Be}(n, p)^7\mathrm{Li}$ reaction rate. The PArthENoPE code developed by INFN [30, 31] was used for the calculation.

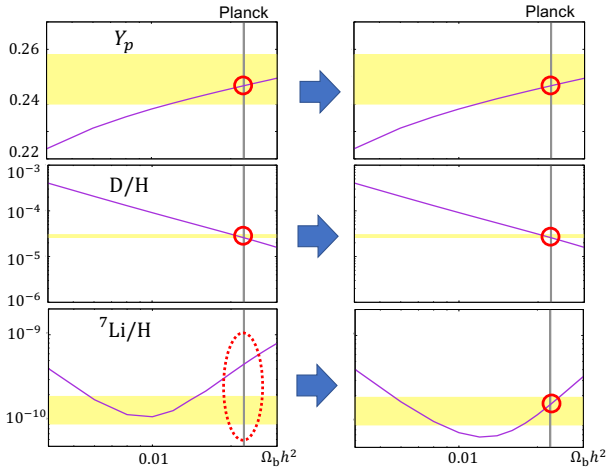

FIGURE 3.5: Change in the light-element abundances before (left) and after (right) the multiplication of the $^7\mathrm{Be}(n,p)^7\mathrm{Li}$ reaction rate. The purple curves are the predictions, whereas the yellow areas represent the abundances deduced from the observation.

Chapter 4

Experimental Setups and Preparation

In Chapter 3, it was demonstrated that a measurement of $\Gamma_{p_1}/\Gamma_{p_0}$, the ratio between the partial widths of proton decay from each excited state of ^{8}Be to the ground state (p_0 group) and to the first excited state (p_1 group) of ^{7}Li, allows to evaluate the cross section of the $^7\mathrm{Be}(n, p_1)^7\mathrm{Li}^*(0.478\ \mathrm{MeV})$ reaction. In order to achieve this, we have carried out the experiment of the $^9\mathrm{Be}(^3\mathrm{He}, \alpha)^8\mathrm{Be}^*(p)^7\mathrm{Li}$ reaction at 30 MeV using the magnetic spectrograph ENMA at the Tandem accelerator faculty in JAEA. Resonance states of ^{8}Be compound nucleus populated by the $(^3\mathrm{He}, \alpha)$ reaction were determined by measuring the magnetic rigidity $B\rho$ of α particles at zero degree, and decay-protons were measured in coincidence by three silicon strip detectors surrounding the target.

In this chapter, the properties of experimental setups and facility used for the measurement will be presented. Also, the preparation works such as detector calibration will be explained.

4.1 Tandem Accelerator and Magnetic Spectrograph ENMA

The Tandem accelerator is a folded electrostatic accelerator as shown in Fig. 4.1. The high voltage is generated by carrying electric charges on the pellet chain, which is adjustable from 2.5 MV to 20 MV. Ion source is placed at the high voltage terminal and $^3\mathrm{He}^{2+}$ get accelerated by the high voltage towards the ground. The high voltage for the measurement was tuned to 15 MV so that the ^{3}He beams at 30 MeV were available. The beam current was averagely about 7 nA for the measurement.

For the study of nuclear reactions, beams from the tandem accelerator are transported to the L3 beam line [32] where the magnetic spectrograph ENMA is placed at zero degree. The incident beam is focused at the target position. Figure 4.2 shows the photograph of the beam spot taken right before the measurement. The beam spot was tuned to a rectangular shape with 4 mm high and 3 mm wide. The angular acceptance of the ENMA spectrograph is ± 60 mrad and ± 70 mrad for horizontal and vertical sides, respectively. It can be adjusted by the vertical and horizontal slits between the target chamber and the ENMA spectrograph. During the measurement, it was set to $\pm 2^\circ$ (± 35 mrad) for the horizontal direction and $\pm 3^\circ$ (± 52 mrad) for the vertical direction, respectively.

The ENMA spectrograph [33–35] consists of two dipole magnets, a quadrupole magnet and three multipole magnets (Q-M1-D1-M2-D2-M3 system) as shown in Fig. 4.3. The first Q magnet which is placed right after the ENMA entrance has a focusing

power in vertical direction. The M1 magnet has a sextupole and a octupole components. It is designed to cancel the higher order aberrations due to the vertical beam spreads. The D1 and D2 sector magnets are to separate charged particles according to the magnetic rigidity $B\rho$ given by

$$B\rho = p/q \quad , \tag{4.1}$$

where p and q, respectively, are the momentum and the electric charge of a particle, B is the magnitude of the magnetic field applied and ρ is the curvature radius of the trajectory. The magnetic fields at D1 and D2 were measured by the NMR probing, and the value was recorded before and after the measurement run. The central curvature radius of both dipole magnets is 110 cm. The exit surface of D1 magnet, both entrance and exit surfaces of D2 magnet are specially curved to cancel the higher order aberrations such as $(x|aa)$, $(x|bb)$, $(x|a\delta)$ and $(x|yb)$ coefficients, together with M1 magnet. The M2 magnet has multipole fields up to decapole. It is installed between the D1 and D2 magnets for correcting the kinematic momentum shift from k = -0.7 to 2.0, where $k = dp/d\theta/p$. The kinematic shift here, is defined as an effective shift in the focal position away from the designed one caused by the variation in energy of particles as a function of the scattering angle; particles entering the ENMA spectrograph at larger angles are deflected more than those entering at smaller angles, thus the focus is shifted farther. The M3 magnet has a quadrupole and a sextupole components. It is applied for changing the dispersion given in the unit of cm/%. This is quite useful in a measurement of an excitation spectrum. One can set a low dispersion to observe the overall spectrum, and then can set higher dispersion to investigate the spectrum in detail. However, this M3 magnet was not used in our measurement.

These setups enable the ENMA spectrograph to have significant specifications such as a momentum-resolving power of about $\Delta p/p = 1/7400$ for the solid angle up to 16 msr. Other properties which should be emphasized here are, the horizontal magnification is 1.7 and the dispersion along the focal plane is 12.6 cm/%. Specifications of ENMA spectrograph are listed in Table. 4.1. After passing the spectrograph, beams are focused near the entrance window (25 μm thick kapton foil) of the focal chamber, which will be discussed in the later section regarding the focal plane position. The incident tilt angle is designed to be 45°, and the focal plane is expected to be straight.

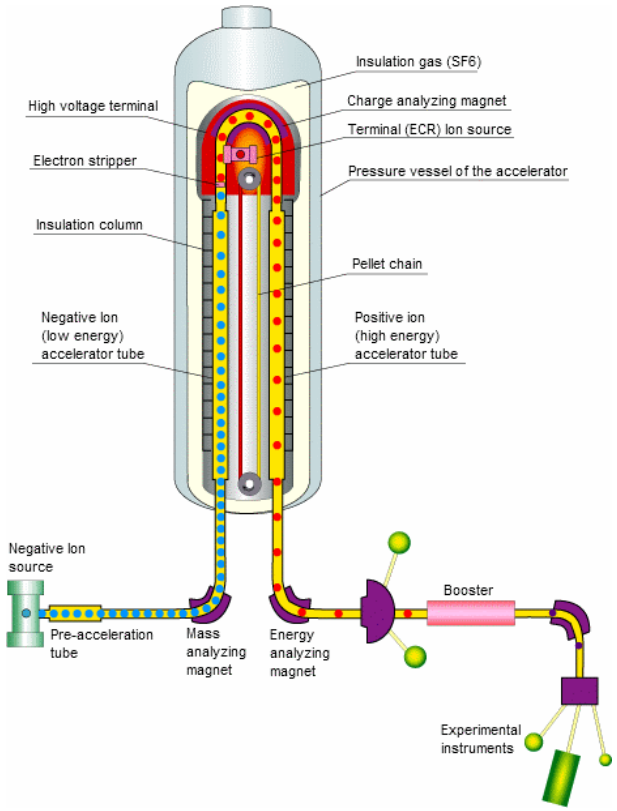

FIGURE 4.1: Schematic drawing of the Tandem accelerator [32]. Blue dots are negatively charged ions, which turn into positively charged ions represented by red dots after the electron stripper.

FIGURE 4.2: A photograph of the beam spot taken right before the measurement. Beams were irradiated on the macor plate with measurement grids printed on it.

TABLE 4.1: Standard specification of ENMA spectrograph

System	Q-M-D-M-D-M
Central orbit radius	110 cm
Flight path length	780 cm
Total deflection angle	152°
Focal plane tilt angle	45°
Focal plane length	130 cm, straight
Maximum $B\rho$	1.7 Tm
Momentum resolving power $p/\Delta p$	7400
Horizontal angular acceptance	±60 mrad
Vertical angular acceptance	±70 mrad
Solid angle	16 msr
Horizontal magnification (x | x)	1.7
Vertical magnification (y | y)	2.1
Dispersion along focal plane (x | δ)	1260 cm

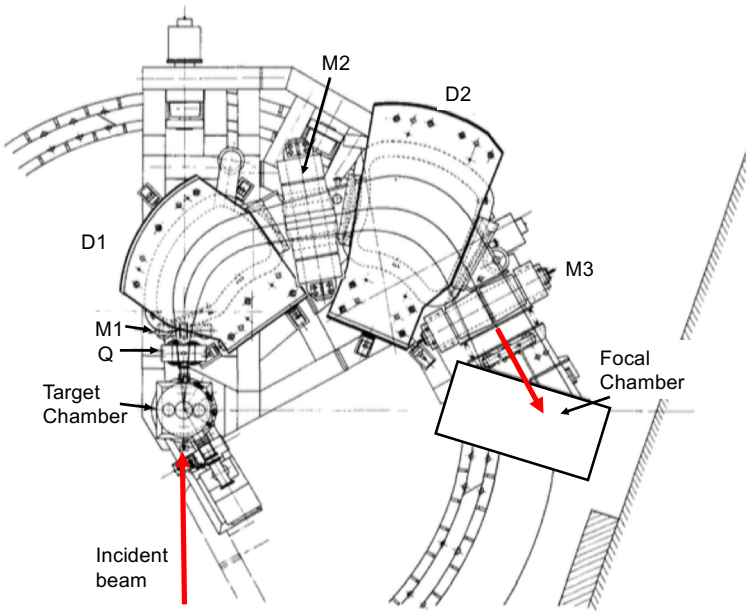

FIGURE 4.3: Schematic drawing of the magnetic spectrograph ENMA.

4.2 Target Chamber

Fig. 4.4 shows a schematic drawing of the target chamber. The incident ^{3}He beam provided by the Tandem accelerator was focused on the target placed at the center of the chamber whose pressure was kept in vacuum during the measurement. The beam intensity was measured by the faraday cup and the telescope detector placed at $\theta = 22^{\circ}$ respect to the beam direction. The counts of the telescope detector was once calibrated with the faraday cup placed at $\theta = 0^{\circ}$, so that the beam count in the faraday cup can be calculated from the one of the telescope silicon detector during the measurement. The monitor silicon detector was used only for making the faint primary beams, to monitor the number of particles entering ENMA spectrograph. Properties of the other materials will be described in detail below.

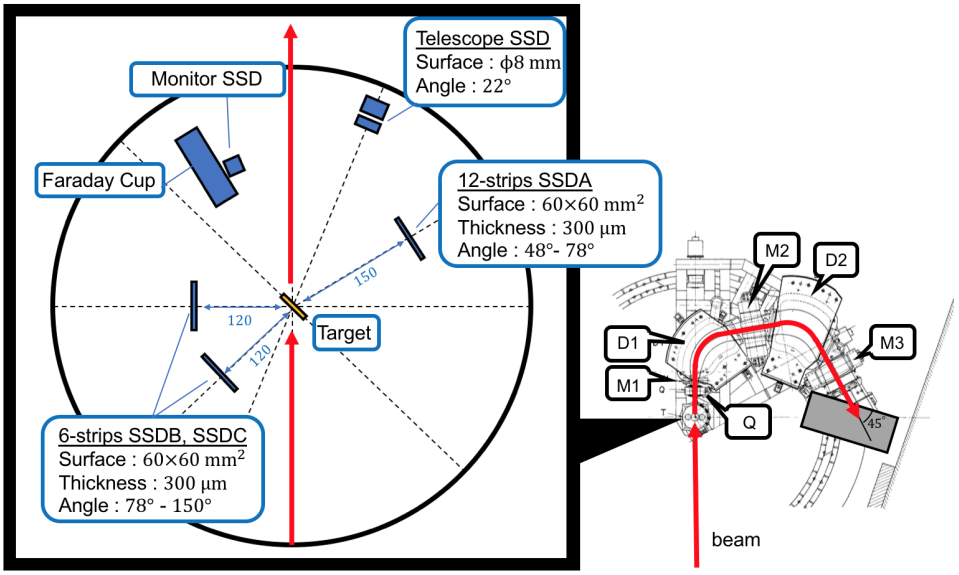

FIGURE 4.4: Schematic drawing of the target chamber.

4.2.1 Targets

^{9}Be, carbon, kapton $(C_{22}H_{10}N_2O_5)_n$ and mylar $(C_{10}H_8O_4)_n$ targets were mounted on a movable ladder. Fig. 4.5 shows the photograph of the target system. Their properties are listed in Table. 4.2. The 1 μm thick ^{9}Be foil contains 1.1 % of ^{12}C and 1.6 % of ^{16}O contaminants. The derivation procedure of the impurity should be referred to Appendix A. Therefore, 1.2 μm thick mylar and 1 mm thick carbon foils were used for the background measurement. The areal density of mylar foil was determined by weighing and the measurement of thickness. Those reference targets are considered ideally pure and homogeneous. The area of ^{9}Be target is 10 mm in diameter and all other targets are 8 mm in diameter. The target ladder was inclined at 45 degrees with respect to the beam direction so that a wide range of the angular distribution, including at 90 degrees, of decay protons could be measured with three silicon strip detectors surrounding the target.

TABLE 4.2: Property of the targets.

Name	Composition	Thickness [μm]	Areal density [$\mu g/cm^2$]
^{9}Be	^{9}Be (1.1 % of ^{12}C, 1.6 % of ^{16}O)	1.0	185.0
Kapton	$(C_{22}H_{10}N_2O_5)_n$	7.84	1113.
Mylar	$(C_{10}H_8O_4)_n$	1.20	167.64
^{12}C	^{12}C	10^3	167

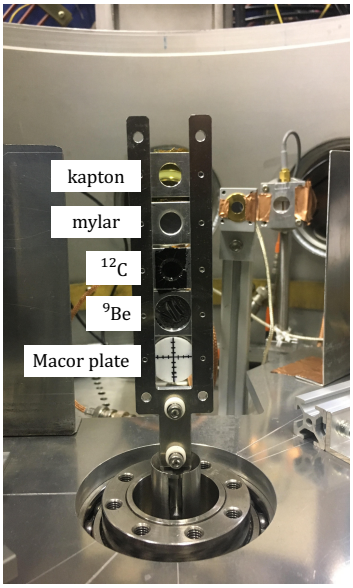

FIGURE 4.5: Photography of the target system.

4.2.2 Silicon Strip Detector

Three silicon strip detectors (SSDA, B, C) were installed in the chamber with surrounding the target as shown in Fig. 4.4. Each detector has 60×60 mm^2 sensitive area and 300 μm thickness. The SSDA has twelve vertical strips, each 5 mm wide. It is placed 150 mm from the target with its center being at $\theta = 59^\circ$ with respect to the beam direction. Both SSDB and SSDC have six vertical strips, each 10 mm wide, and are placed 120 mm from the target. The center of SSDB is at $\theta = 90^\circ$ and that of SSDC is at $\theta = 136^\circ$. This configuration allows a wide angular domain of proton-decays to be measured, from $\theta = 48^\circ$ to $\theta = 150^\circ$. In Table. 4.3 the values of the central angle and the solid angle of each strip are listed.

Bias voltage of 60 V was applied to each SSD to enlarge the depletion zone (I-layer). In general, the required energy to produce one hole-electron pair in the I-layer is 3.62 eV at the room temperature. Resulting electrons and holes are attracted along with the applied electric field, which become electric signals traveling through a flat cable to a charge-sensitive preamplifier (mesytec MPR-16L) which was connected outside

TABLE 4.3: Configurations of the SSD strips. Displayed angles correspond to the centers.

SSDA					
strip	Angle [°]	$\Delta\Omega$ [$\times 10^{-2}$ sr]	strip	Angle [°]	$\Delta\Omega$ [$\times 10^{-2}$ sr]
1	69.4±0.3	1.24±0.03	7	58.0±0.2	1.31±0.03
2	67.5±0.3	1.26±0.03	8	56.1±0.2	1.30±0.03
3	65.7±0.3	1.28±0.03	9	54.2±0.3	1.29±0.03
4	63.8±0.3	1.29±0.03	10	52.3±0.3	1.28±0.03
5	61.9±0.2	1.30±0.03	11	50.5±0.3	1.26±0.03
6	60.0±0.2	1.31±0.03	12	48.6±0.3	1.24±0.03
SSDB			SSDC		
1	78.2±0.4	3.79±0.13	1	124.2±0.4	3.79±0.13
2	82.9±0.3	3.95±0.13	2	128.8±0.3	3.95±0.13
3	87.6±0.3	4.03±0.13	3	133.6±0.3	4.03±0.13
4	92.4±0.3	4.03±0.13	4	138.3±0.3	4.03±0.13
5	97.1±0.3	3.95±0.13	5	143.1±0.3	3.95±0.13
6	101.8±0.4	3.79±0.13	6	147.7±0.4	3.79±0.13

the chamber.

During the measurement, the leak current in each SSD was monitored. The maximum leak current was 0.9 μA for SSDB at the end of measurement, which corresponds to a 0.9 V of voltage-drop which may give a negligible effect on the energy resolution.

The ^{8}Be resonance states of interest decay through gamma, proton, neutron, and alpha channels. The particle identification was performed by measuring the kinetic energy and the time-of-flight (ToF) of particles, which will be discussed in the later chapter.

4.3 Focal Plane Chamber

Figure 4.6 shows a schematic drawing of the focal plane chamber. After passing through the ENMA spectrograph, beams of interesting charged particles are focused near the entrance window of the focal chamber. The chamber was filled with isobutane (C_4H_{10}) gas at room temperature with a pressure of 150 mbar. In Table 4.4, the property of isobutane gas at 20°C and 760 Torr is listed [36]. The E_x, E_i and w_i are the excitation and ionization energies and the average energy required to produce an electron-ion pair, respectively. A 25 μm thick kapton foil was used as the entrance window. At the downstream of the window, two slits of aluminum plates were attached on the wall in order to regulate the horizontal domain of particle trajectory, conforming with the width of the plastic scintillator (90 cm) placed at the end of beam line. Particles are detected sequentially by the wire chambers and the plastic scintillator whose properties will be described in the following subsections.

TABLE 4.4: Property of isobutane gas at 20°C and 760 Torr [36]

Property	Unit	Value
Z		34
A		58
Density $\times 10^{-3}$	g/cm^3	2.59
E_x	eV	6.5
E_i	eV	10.6
w_i	eV	23

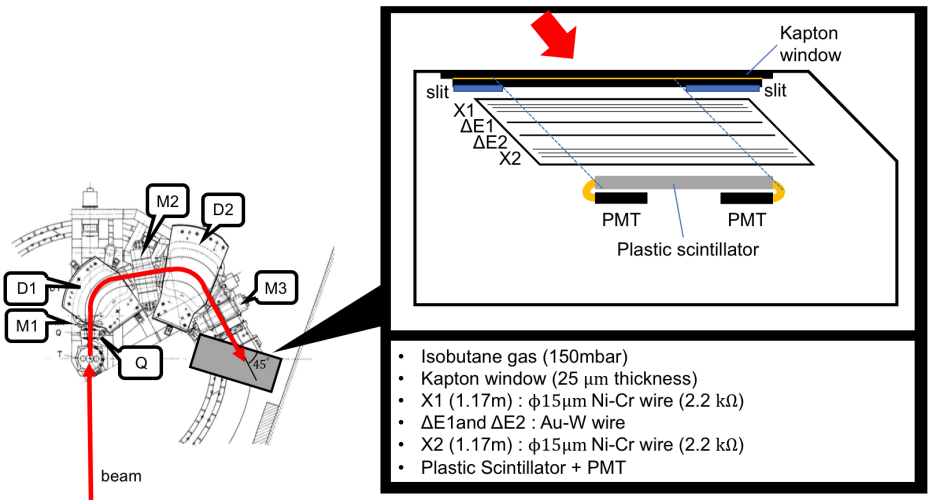

FIGURE 4.6: Schematic drawing of the focal chamber.

4.3.1 Wire Chamber

The wire chamber consists of 4 sets of anode wires and a cathode plate as depicted in the Fig. 4.7 and Fig. 4.8. The shape of chamber is a parallelogram whose angle of apex is 45 degrees, which conforms with the incident tilt angle of the beam trajectory from ENMA spectrograph. Charged particles passing through the chamber ionize the isobutane gas along with their trajectories. The resulting ions and electrons are accelerated by the electric field between the anode wires and the cathode, causing an avalanche, and are collected at the nearest wire, resulting in a measurable charge signal whose amplitude is proportional to the the number of electron-ion pairs generated by the ionization.

Two sets of three Ni-Cr resistance wires combined in parallel were installed 9 cm apart, and named as X1 and X2. Each single wire is 15 μm in diameter, and has a 6.6 kΩ resistance. A high voltage of 950 V was applied on both X1 and X2 and -800 V was applied on the cathode plate. Signals are transferred to both left and right side by resistance dividing so that the horizontal (X-)position of the particle trajectory

can be characterized by the parameter X_{pos} which is given by

$$X_{pos} = \frac{Right}{Right + Left} \quad . \tag{4.2}$$

Between X1 and X2, two Au-W wires with 25μm diameter, named as $\Delta E1$ and $\Delta E2$, were installed for measuring the energy loss of charged particles in the gas. A high voltage of 750 V was applied on both $\Delta E1$ and $\Delta E2$, and the same cathode plate as X-wires was used. Signals are transferred to only one side of each wire. In addition to the energy loss information, these wires provide the vertical (Y-)position information of particle trajectories by ToF measurement between $\Delta E1(\Delta E2)$ and the plastic scintillator. The relation is given by

$$y = v_d \times t_d + y_{off} \quad , \tag{4.3}$$

where v_d is the drift velocity, t_d is the drift time and y_{off} is the calibration offset.

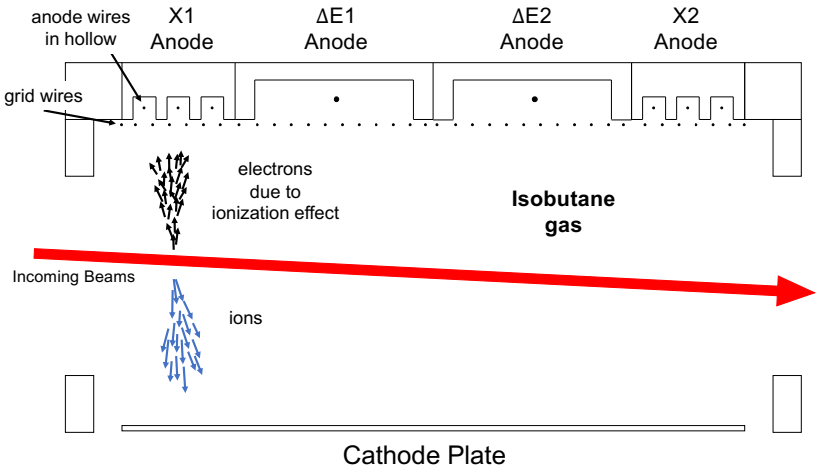

FIGURE 4.7: Schematic view from the left side of the wire chamber.

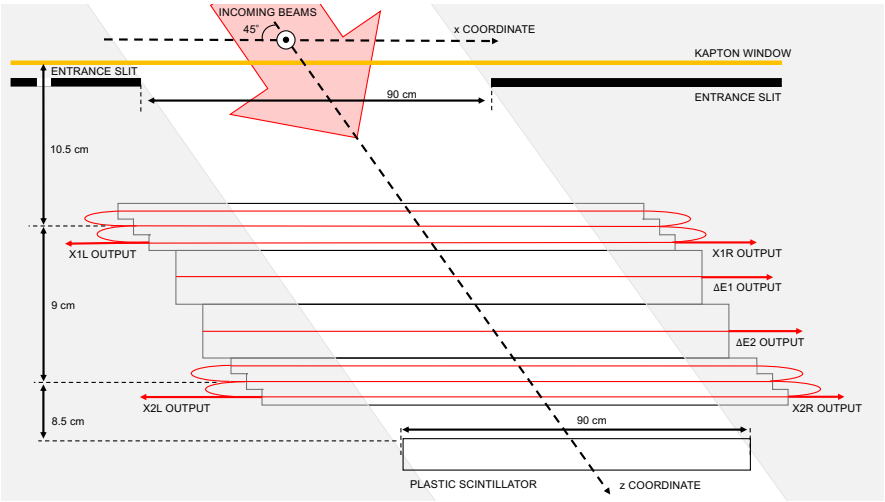

FIGURE 4.8: Schematic view from the top of the wire chamber.

4.3.2 Plastic Scintillator

A 90 cm wide plastic scintillator in rectangular shape with two photomultipliers (PMT) connected at both edges was placed at the end of the beam line. The energy loss of charged particles in the scintillator causes the excitations of the atoms and molecules which compose the scintillator, which results in the emission of light. This light is transmitted through the fiber light guides to the PMTs in which the light is converted into photoelectron which is amplified by the sequential multiplier system. The signals are converted into digital by the QDC, a charge sensitive ADC, then acquired in the DAQ. Since this signal transfer is very quick in this detector, it was applied for the common stop signal in the data acquisition system to measure coincident events of α particles at focal chamber along with decay protons at the target chamber.

The energy of particles are measured according to the light intensity whose magnitude is proportional to the energy deposit. Depending on the horizontal position at which charged particles are detected in the plastic scintillator, a difference occurs in the light intensity detected in the left and right PMTs. The intensity Q is given by

$$Q_{\text{left}} = A \cdot \exp\left(-\frac{L+x}{\lambda}\right) \quad , \quad Q_{\text{right}} = A \cdot \exp\left(-\frac{L-x}{\lambda}\right) \tag{4.4}$$

where A is the magnitude, L is the half length of the plastic scintillator measured from the left side edge and λ is the attenuation length. The square root of the product of Q_{left} and Q_{right} provides an information of the magnitude independent of the particle position x. It is given by

$$< A >= \sqrt{Q_{\text{left}} \cdot Q_{\text{right}}} = |A| \cdot \sqrt{\exp\left(-\frac{L}{\lambda}\right)} \quad . \tag{4.5}$$

The timing information of the plastic scintillator was taken as the average between the left and right signals as

$$T = \frac{1}{2}(T_{\text{left}} + T_{\text{right}}) \quad . \tag{4.6}$$

4.4 Data Acquisition

The data acquisition system used in the measurement is schematically displayed in Fig 4.9 and 4.10.

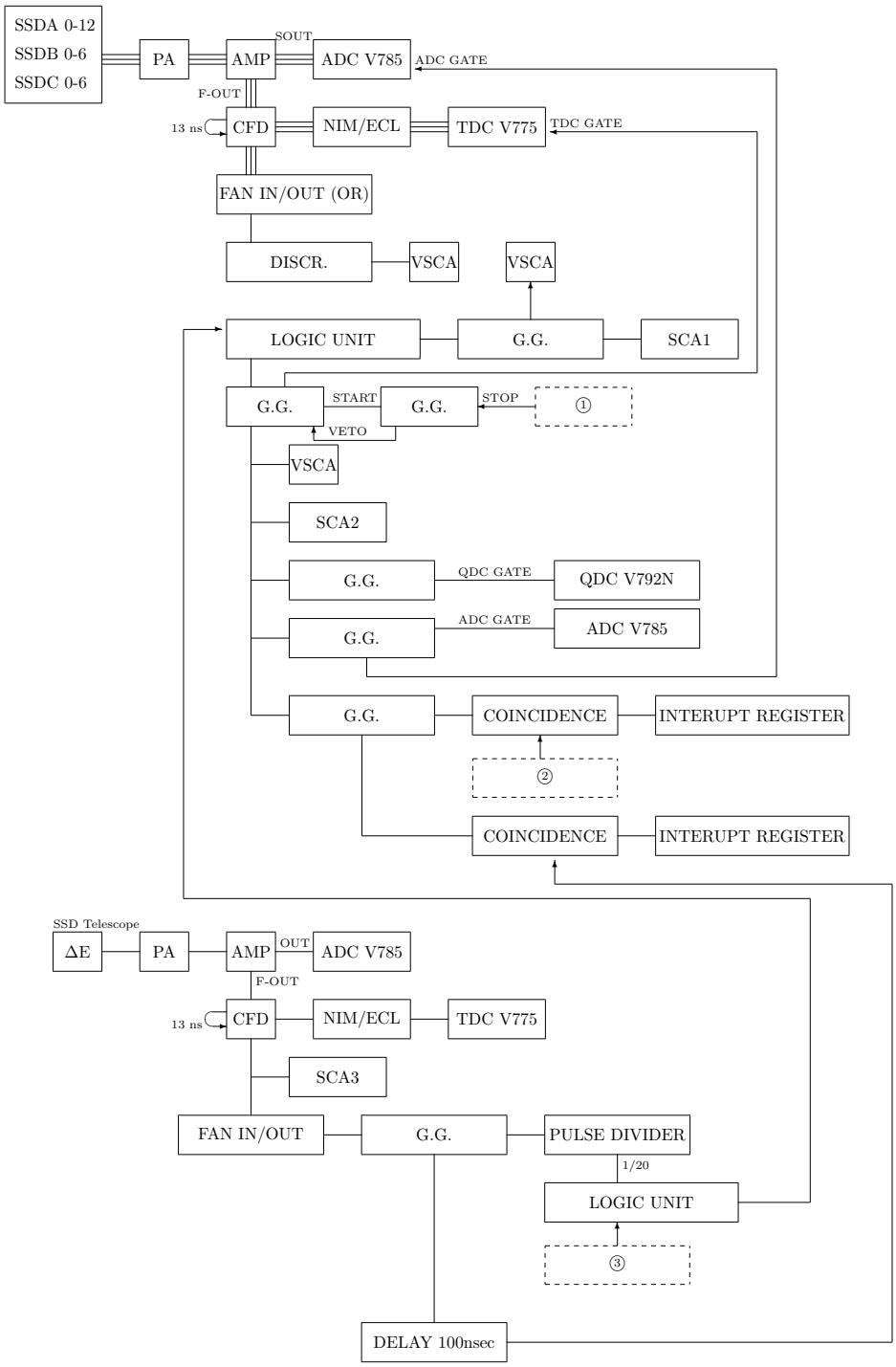

FIGURE 4.9: Block diagram of the experimental data acquisition system.

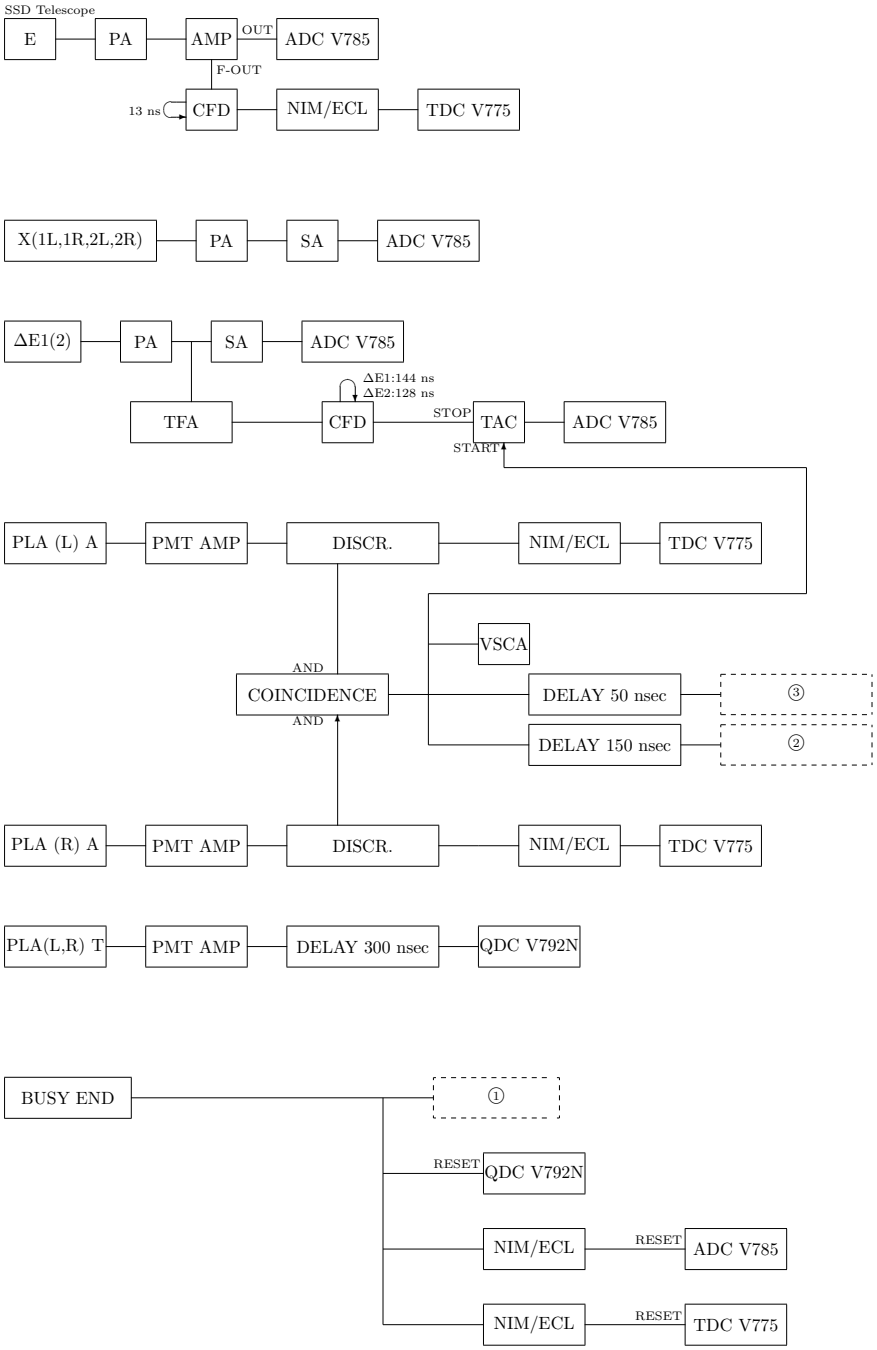

FIGURE 4.10: Block diagram of the experimental data acquisition system.

4.5 Two-body Kinematics

In order to estimate the magnetic rigidity of α particles and the energy spectrum of decay protons, a simulation using the relativistic two body kinematics of the $^{9}\mathrm{Be}(^{3}\mathrm{He},\alpha)^{8}\mathrm{Be}^{*}(p)^{7}\mathrm{Li}$ reaction was carried out.

TABLE 4.5: The mean energy and magnetic rigidity $B\rho$ of α particle corresponding to the excited state of ^{8}Be. The resonances from $E_X =$ 18.91 MeV to 20.9 MeV are the energy region of interest.

^{8}Be			α	
I^π	E_X [MeV]	Γ [MeV]	E [MeV]	$B\rho$ [Tm]
2^+	16.626		31.889	0.815
2^+	16.922		31.615	0.811
1^+	17.64		30.947	0.803
1^+	18.15		30.471	0.797
2^-	18.91	0.122	29.759	0.787
3^+	19.07	0.27	29.609	0.785
3^+	19.235	0.227	29.453	0.783
1^-	19.4	0.645	29.297	0.781
4^+	19.86	0.7	28.863	0.775
2^+	20.1	0.88	28.636	0.772
0^+	20.2	0.72	28.541	0.771
4^-	20.9	1.6	27.876	0.762

4.5.1 Initial Reaction ($^9\mathrm{Be} + {}^3\mathrm{He} \rightarrow {}^8\mathrm{Be}^* + \alpha$)

The energy and magnetic rigidity of scattering α particles were calculated for each resonance state of ^{8}Be as shown in Table 4.5. The settings in the present simulation are as follows: A 30 MeV ^{3}He particle reacted with a ^{9}Be atom which was at rest, resulting a scattering α particle and a residual ^{8}Be. In order to obtain a good outlook results we assumed that the reaction went by a delta functional respondence. Any energy loss or struggling in target were not considered since the energy loss in target was small. The scattering angle of the α particle was limited within the angular acceptance of the entrance slit of ENMA spectrograph, which is $\theta \leq 2^\circ$; on the other hand the azimuthal symmetry was considered. The widths of ^{8}Be energy levels were not considered.

Figure 4.11 shows the calculated magnetic rigidities for each case in which each resonance state of ^{8}Be from $E_X = 18.91$ MeV to 20.9 MeV is populated. Each peak has a narrow spread due to the scattering angle. The mean $B\rho$ values were obtained by fitting with a Gaussian function. The results are listed in the Table 4.5 as well as the corresponding kinetic energies in MeV. Moreover, from the angular distribution of ^{8}Be shown in Fig. 4.12, it was found that ^{8}Be moves backward respect to the beam direction. This movement skews the angular distribution and causes energy spread of decay protons, which will be shown in the next section.

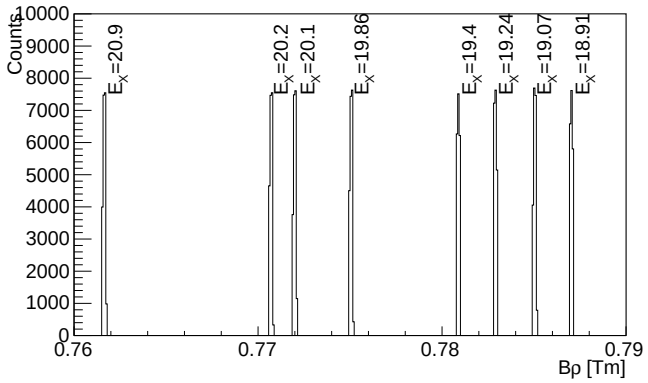

FIGURE 4.11: $B\rho$ distribution of α particle corresponding to the excited state of ^{8}Be.

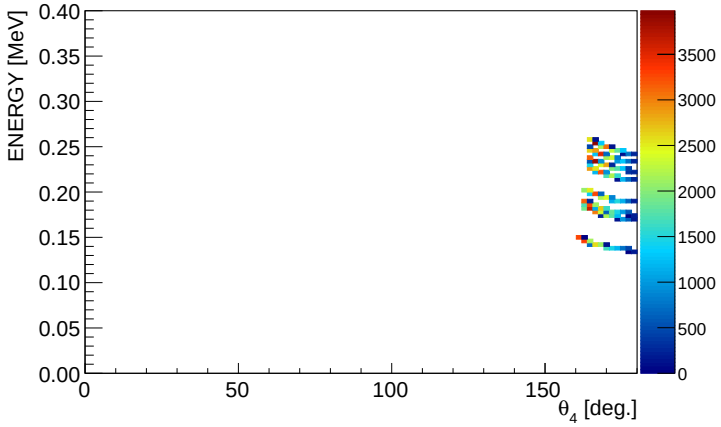

FIGURE 4.12: Angular distribution of ^{8}Be.

4.5.2 Sequential Decay Reaction ($^{8}\mathrm{Be}^{*} \rightarrow {}^{7}\mathrm{Li} + p$)

The ^{8}Be moving backward to the beam direction, resulted from the initial reaction, decays to ^{7}Li which is in either the ground state or the first excited state by emitting a proton. To simulate the angular distribution of kinetic energy of decay proton, the scattering angle θ_{cm} of decay-proton in the rest frame of ^{8}Be, was chosen according to the Legendre polynomial P_L up to the 3rd order. These polynomials are

$$\begin{aligned} P_0 &= 1 \quad , \\ P_1 &= \cos\theta_{cm} \quad , \\ P_2 &= \frac{1}{2}\left(3\cos^2\theta_{cm} - 1\right) \quad , \\ P_3 &= \frac{1}{2}\left(5\cos^3\theta_{cm} - 3\cos\theta_{cm}\right) \quad . \end{aligned} \tag{4.7}$$

These polynomials are considered to reflect the angular distribution of wave function with respect to the angular momentum L (=0, 1, 2, 3) in quantum mechanics. Figure 4.13 shows the angular distribution of protons in the laboratory system for each case that each excited state of ^{8}Be, from $E_X = 18.91$ MeV to $E_X = 20.9$ MeV, decays to ^{7}Li. The upper curve corresponds to the decay reaction that the ground

state of ^{7}Li is populated, and the lower curve to the first excited state. From these results, the kinetic energy of proton can be found in the range from 0.5 MeV to 4 MeV, while the distribution get skewed upper as the angle gets larger.

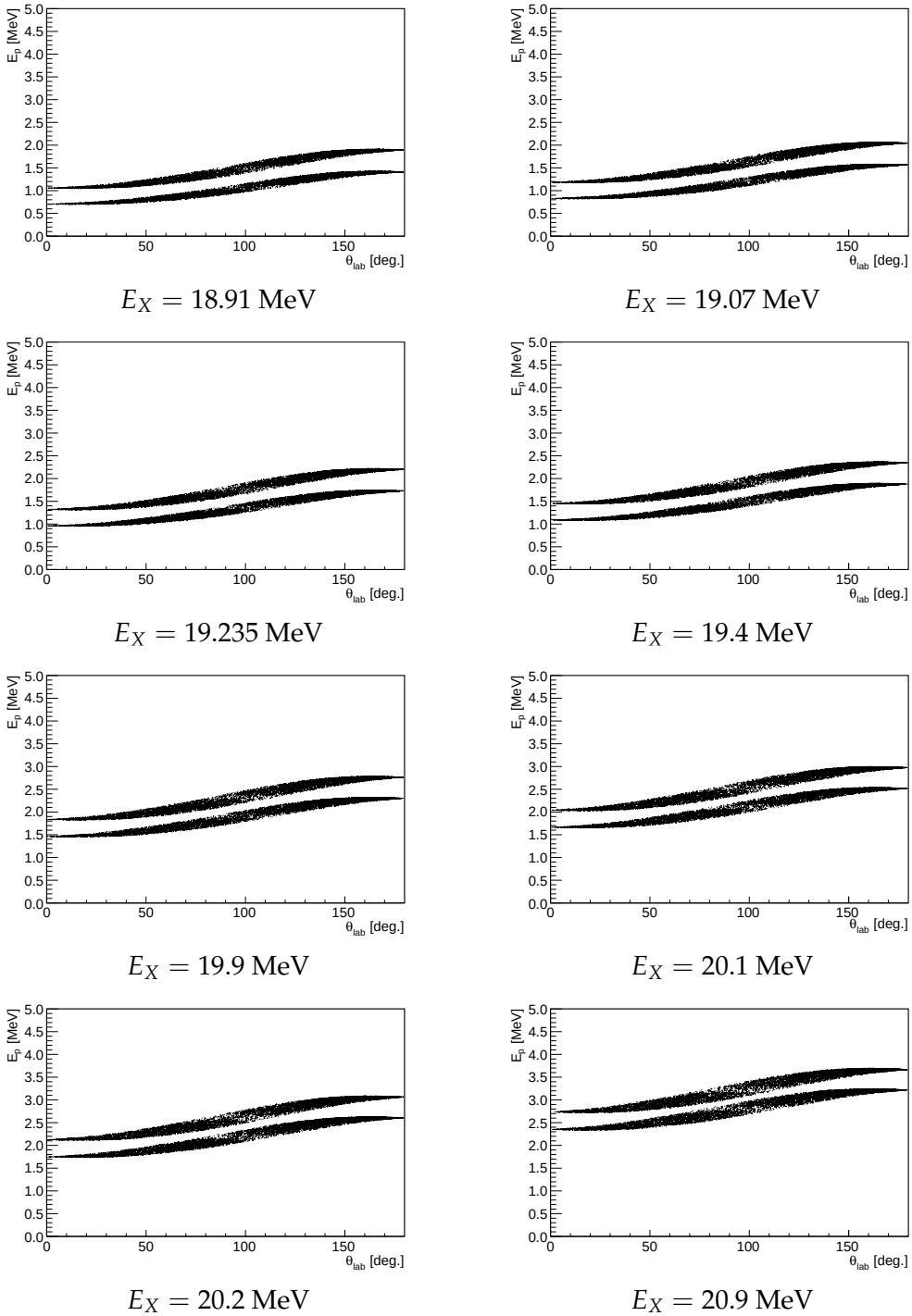

$E_X = 18.91$ MeV $E_X = 19.07$ MeV

$E_X = 19.235$ MeV $E_X = 19.4$ MeV

$E_X = 19.9$ MeV $E_X = 20.1$ MeV

$E_X = 20.2$ MeV $E_X = 20.9$ MeV

FIGURE 4.13: Angular distribution of decay protons emitted from ^{8}Be moving backward.

4.6 Calibration

4.6.1 ADC Linearity

For the measurement, an ADC (CAEN V785) whose maximum range is 4096 ch was used for the data processing from SSD and wire chambers (X1, X2, $\Delta E1$ and $\Delta E2$). The linearity and pedestal of this ADC were checked for each channel with a research pulser, the magnitude of output signal of which is proportional to the variable dial number. Figure 4.14 shows the corresponding spectrum for SSDA's strip-1 when the research pulser dial was changed from 90000 to 10000 by intervals of 10000, and in addition when the dial was 5000. The leftmost peak corresponds to the pedestal. The red triangles represent the peak positions. Figure 4.15 shows the plots of peak channels against the corresponding dial values. Data points were fitted with a linear function as depicted with a redline in the figure. The lower part of Fig. 4.15 shows the residual deviation from the calibration line of each deduced dial values using the raw ADC data. The deviation was averagely less than RP dial of 100 for all channels of SSD, which corresponds to the energy deviation of about 10 keV. This deviation is smaller than the energy resolution of SSD, thus no correction terms for the linear function were required. For the further data processing, the unit of data are converted and treated in a unit of dial.

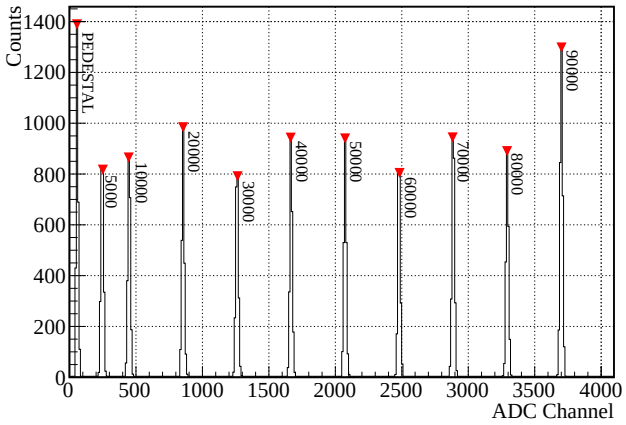

FIGURE 4.14: Research pulser spectrum of SSDA-1.

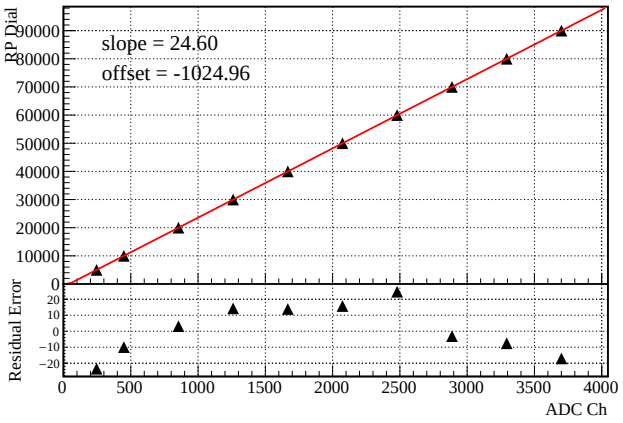

FIGURE 4.15: ADC linearity check against the research pulsar inputs.

TABLE 4.6: Properties of SSD strips. The energy resolution $\Delta E/E$ and the measurable minimum energy are given.

SSDA			SSDB		
strip	$\Delta E/E$ [%]	E_{min} [MeV]	strip	$\Delta E/E$ [%]	E_{min} [MeV]
1	1.19	0.045	1	0.67	0.035
2	0.79	0.020	2	0.72	0.035
3	0.72	0.012	3	1.45	0.047
4	0.79	0.032	4	0.66	0.036
5	0.75	0.024	5	0.68	0.057
6	0.77	0.012	6	0.65	0.056
			SSDC		
7	0.62	0.029	1	0.67	0.051
8	0.66	0.034	2	0.65	0.053
9	0.68	0.029	3	0.58	0.059
10	0.71	0.032	4	0.67	0.051
11	0.76	0.019	5	0.59	0.060
12	0.79	0.028	6	0.87	0.061

4.6.2 SSD Energy Calibration

Based on the simulation of two-body kinematics described before, the kinetic energy of decay proton is found within the range from 0.5 MeV to 4 MeV. Thus, an alpha source of ^{241}Am was used for the energy calibration for the SSD. It emits mainly 5 alpha lines, the most abundant decay branch of which is at 5.486 MeV (84% of branching ratio). This energy was matched with the mean ADC channel value of the measured spectrum such as shown in Fig. 4.16. The mean value was obtained by fitting the spectrum with a Gaussian function, which corresponds to the red curve. According to this process, data taken in SSD strips are treated in MeV unit.

Regarding the pedestal which is at the left end in Fig. 4.14, the minimum measurable energy at each strip can be evaluated. It was found that energy information larger than about 100 keV can be detected properly in the measurement. This minimum limit is low enough compared with the expected minimum energy of decay protons ($E_p = 0.5$ MeV) calculated from the simulation.

The energy resolution of each SSD strip was evaluated from the Gaussian fitting. Using the deviation σ and the mean value μ obtained in the fitting yields the energy resolution at full-width-half-maximum (FWHM), which is given by

$$\frac{\Delta E}{E} = \frac{2.35\sigma}{\mu} \times 100 \ \ [\%]. \tag{4.8}$$

The energy resolutions of SSD strips are listed in Table 4.6. Overall condition looked fine except for SSDB-3.

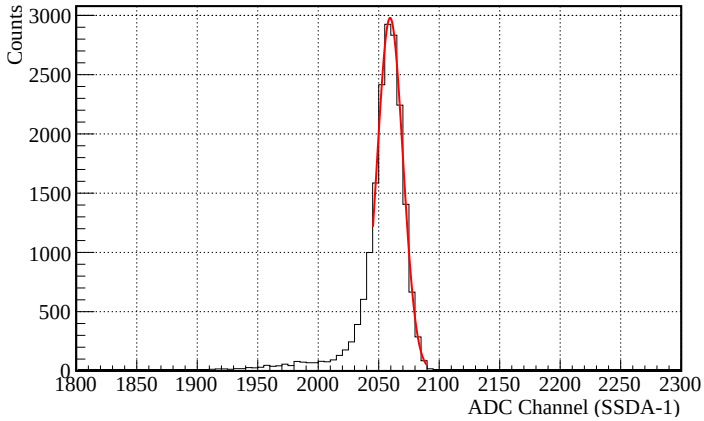

FIGURE 4.16: An example histogram for the energy calibration with α source ^{241}Am.

4.6.3 Time Calibration

A TDC (CAEN V775) was used for the data processing of timing information from each strip of SSD and from the plastic scintillator. The time calibration of TDC was carried out by inputting test pulses at intervals of 10 nsec into each channel of TDC with a time calibrator. Figure 4.17 shows the corresponding spectrum for the channel of SSDA's strip-1 as an example. The red triangles represent the peak positions. In the same way to deduce the calibration parameters as the energy calibration was done, data points were fitted with the linear function as shown in Fig. 4.18. Timing data will be treated in nsec unit.

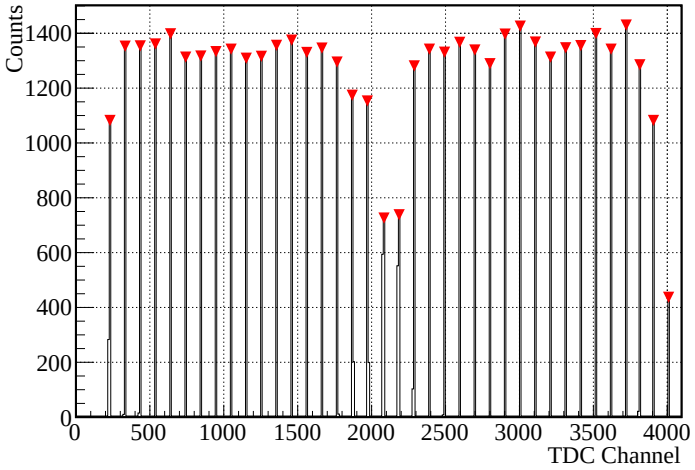

FIGURE 4.17: An example spectrum for the time calibration with the time calibrator input.

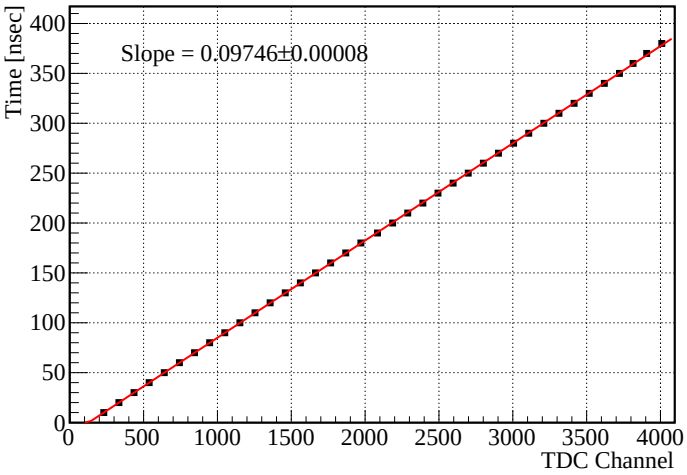

FIGURE 4.18: An example graph of the calibration line for TDC.

4.6.4 Primary Beam Measurement

Charge signals at X1 and X2 are transmitted by resistance dividing to both left and right sides, and the particle position is detected by $Right/(Left + Right)$ at each wire. Primary beams were measured at X1 and X2 to calibrate the position information of latter to that of former. This calibration was done under the assumption that the incident tilt angle of primary beams was independent of the magnetic rigidities. The magnetic field strength in D1 and D2 sector magnets were changed for different values; letting the primary beams passing through the central orbit of the ENMA spectrograph ($B\rho = 0.686$ Tm) be 0%, the field strength was changed by about $\pm 2\%$ (corresponding to the settings which the central orbit is set to particles of 0.672 and 0.700 Tm for positive and negative sign, respectively). Figure 4.19 a) and b) shows the measured spectra at X1 and X2, respectively. Using the x-positions of primary beams at both X1 and X2, the calibration function was obtained as shown in Fig. 4.20 to

$$X2'_{pos} = 28.627 + 0.958 \times X2_{pos} = X1_{pos} \quad . \tag{4.9}$$

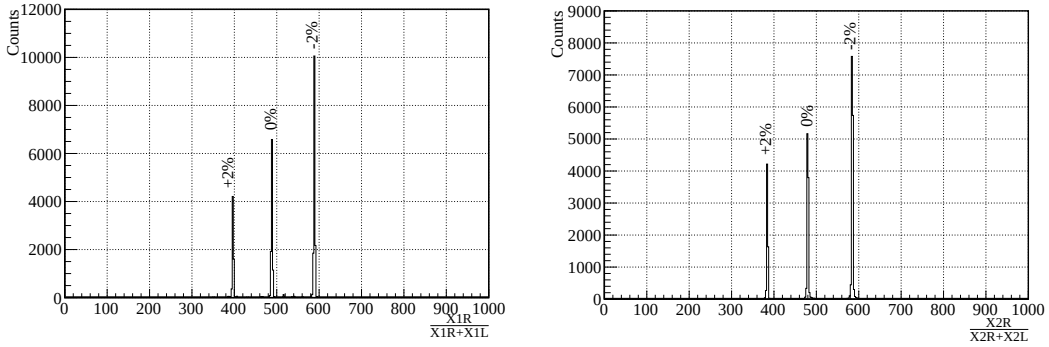

a) X1 spectrum b) X2 spectrum

FIGURE 4.19: Primary beam measurement. The percentage represents the shift in the magnetic field strength of D1 and D2 magnets from the setting that α particles travels on the central trajectory (0 %).

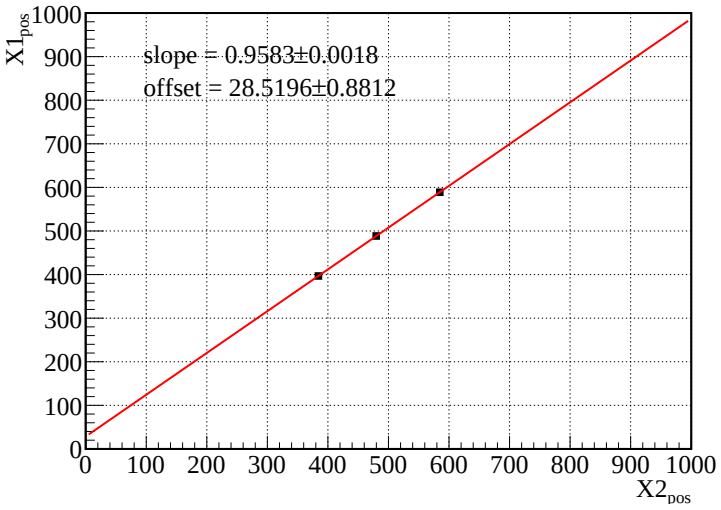

FIGURE 4.20: The calibration line for X1 and X2 obtained from the primary beam measurement.

Chapter 5

The ^{9}Be(^{3}He, α)^{8}Be*(p)^{7}Li Reaction Measurement

With the setups described in the previous chapter, the ^{9}Be(^{3}He, α)^{8}Be*(p)^{7}Li reaction measurement at 30 MeV was performed. Particles with $B\rho = 0.791$ Tm were set to the central orbit of the ENMA spectrograph. This setting allowed an excitation energy (E_X) spectrum of ^{8}Be to be measured for the approximate range from 16.5 MeV up to 20.5 MeV at the focal plane as shown in Fig. 5.1 a); the derivation of the spectrum will be explained in the following subsections. The rest of the aimed range from 20.5 MeV to 20.9 MeV was unexpectedly not achievable in this measurement because of the systematic problem as follows: when a lower $B\rho$ (for example = 0.786 Tm) was set for the central orbit to include the whole energy range of interest, there was a flood of background particles mixed into the data acquisition as shown in Fig. 5.1 b). This is probably due to a situation that beam with low $B\rho$ scattered on the inner surface of duct of the ENMA spectrograph, resulting a background shower of secondary particles.

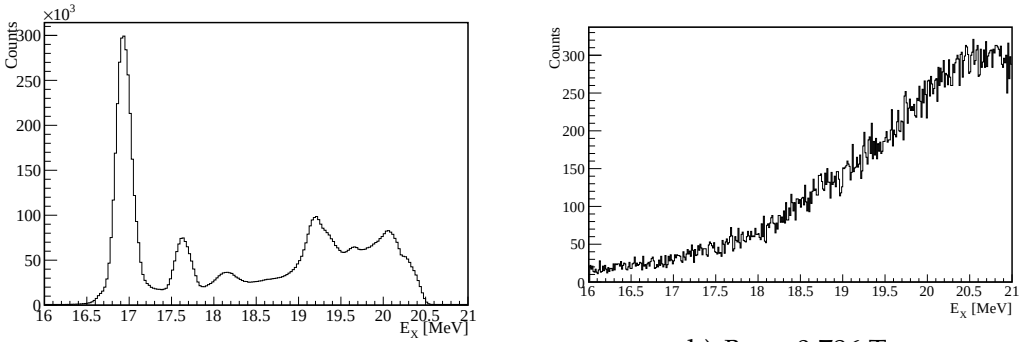

a) $B\rho = 0.791$ Tm

b) $B\rho = 0.786$ Tm

FIGURE 5.1: Excitation spectrum of the ^{9}Be(^{3}He, α)^{8}Be reaction at the focal plane. Left figure (a) shows the spectrum obtained in this experiment and the right figure (b) shows the spectrum in which the resonance peaks are no longer visible by the background particles.

5.1 ^{8}Be Excitation Energy Spectrum at Focal Plane

The resonance states of ^{8}Be populated by the ^{9}Be(^{3}He, α)^{8}Be reaction were determined according to the magnetic rigidity of α particles measured at the focal plane chamber. In this section, the procedure to obtain the excitation spectrum shown in Fig. 5.1 a) will be explained.

5.1.1 α Particle Selection

From the initial reaction between ^{3}He and ^{9}Be, not only α particles but also other light particles such as protons, deuterons and tritons may be produced. These events are likely to be mixed and detected at the focal plane chamber as background signals. The elastic/inelastic scattering events are not detected since the magnetic rigidity of the ^{3}He beam is already $B\rho = 0.686$ Tm, which is lower than the minimum of the measurement range ($B\rho \sim 0.77$ Tm). See Appendix B for the lists of nuclear reactions and leading particles, which are likely/unlikely to be detected at the focal plane chamber. In the tables, the magnetic rigidity and the energy were calculated from the two body kinematics in which leading particles are assumed to be scattered at zero degree.

To select ^{4}He events, the ΔE-E technique was applied. Energy loss of a charged particle in a medium is in short given by

$$\Delta E \propto \frac{z^2}{\beta^2} \propto \frac{Mz^2}{E}, \tag{5.1}$$

where z, β, M and E are the electric charge, velocity, mass and the kinetic energy of the detected particle, respectively in the non-relativistic limit. Figure 5.2 represents a correlation diagram of ΔE information of $\Delta E1$ of the wire chamber and E information of the plastic scintillator. The upper graph shows the raw data, and four peaks can be seen. They represent protons (p), deuterons (D), tritons (T) and α particles, from left to right, respectively. The lower figure of Fig. 5.2 shows the result after the α particle selection.

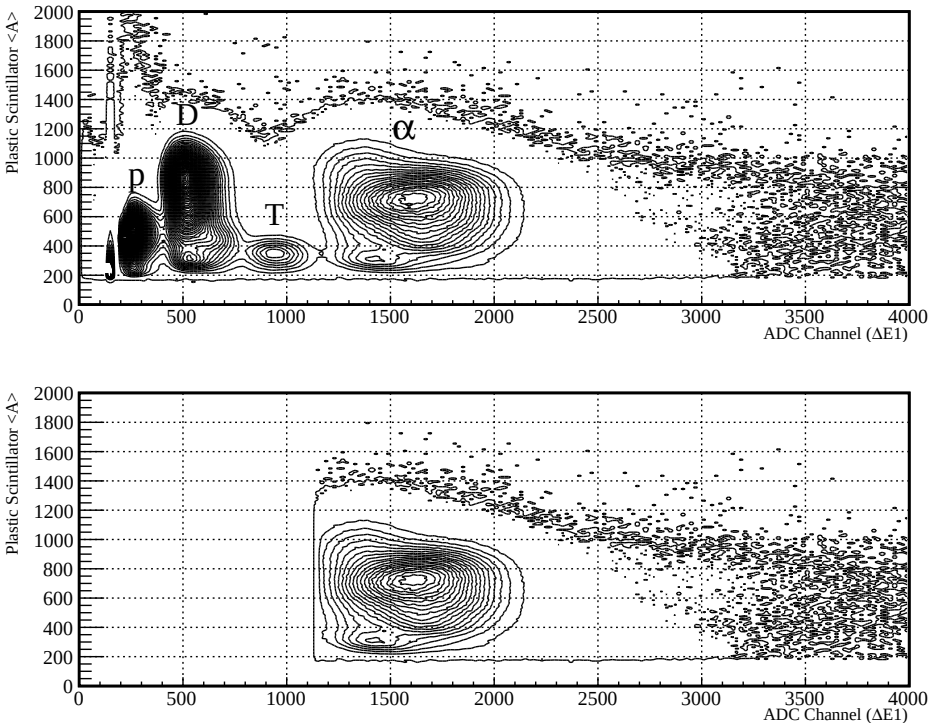

FIGURE 5.2: A ΔE-E correlation diagram between the ΔE information of $\Delta E1$ of the wire chamber and E information of the plastic scintillator. α particle events are selected as shown in the lower figure.

5.1.2 Focal Plane

Here, the line of the trajectory of the central orbit of the ENMA spectrograph entering the focal plane chamber is defined as z-axis. The focal plane is known to be tilted by 45 degrees. To check the focal plane, the horizontal position at each z plane was reconstructed by using the position information at $X1$ and $X2$ for event by event. The formula used here is given by

$$X_{\mathrm{pos}}(z) = \frac{X2_{\mathrm{pos}} - X1_{\mathrm{pos}}}{10} \times z + X1_{\mathrm{pos}} \quad , \tag{5.2}$$

where the distance between X1 and X2 along the z-axis was set to 10 for instance (corresponding to $9\sqrt{2}$ cm). The z value was changed by 1 from -35 to 15. At each spectrum at each z, the rightmost peak which represents the excited state of ^{8}Be at $E_X = 16.92$ MeV, as indicated in Fig. 5.4(a), was fitted with a Gaussian to evaluate the FWHM value; the minimum value was found at $z_{\mathrm{foc}} = -10$, i.e. at the position 9 cm upstream from X1 which was near the entrance window of the focal plane chamber. This minimum width corresponds to the "waist" of the beam, however, its position almost coincides with the expected position of the focal plane according to the specification of the ENMA spectrograph, so that this plane was defined as the focal plane in our measurement.

With the focal plane spectrum obtained, the distance between both edges of the spectrum was defined to be the same width of the entrance slits, 90 cm wide, so that the position information can be evaluated as a variable in the unit of length. In this spectrum, the larger position corresponds to the outer orbit in ENMA spectrograph, which is, the higher $B\rho$ of α particles, in other words, the lower excitation energy of ^{8}Be.

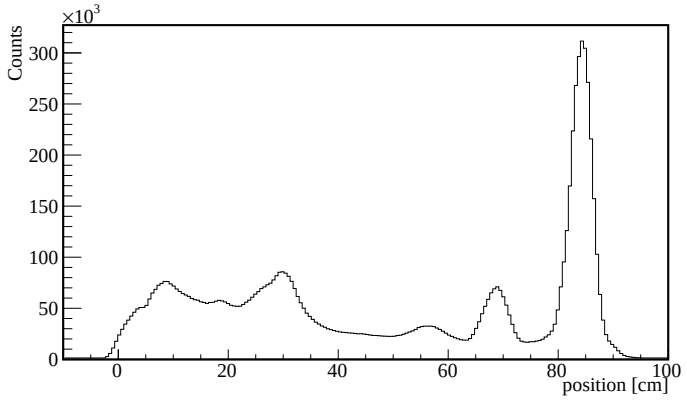

FIGURE 5.3: Raw spectrum of the α particles from the ^{9}Be(^{3}He, α)^{8}Be reaction at the focal plane.

5.1.3 Position to $B\rho$

In Fig. 5.4 a), three peaks are indicated with arrows. They correspond to the cases in which ^{8}Be is in the excited states of 16.92 MeV (2^{+}), 17.64 MeV (1^{+}) and 18.15 MeV (1^{+}) from right to left, respectively. Mean values of the peaks were obtained by fitting with a Gaussian and matched with the corresponding $B\rho$ values of α particles listed in Table 4.5. In addition, α spectra from the measurements with the carbon and the mylar targets, which were performed with the same experimental settings as the ^{9}Be run, were obtained as shown in Fig. 5.4 b) and c). The peaks with arrows

correspond to the several different states of ^{11}C and ^{15}O from the ^{12}C(^{3}He, α)^{11}C reaction and the ^{12}C(^{3}He, α)^{11}C reaction. For the use as calibration data, the peaks of ^{11}C($3/2^{-}$, g.s.), ^{11}C($1/2^{-}$, 2.0 MeV) and ^{15}O($3/2^{-}$, 6.176 MeV) were taken. The corresponding $B\rho$ of α particles are, respectively, 0.811, 0.786 and 0.772 Tm. With these 6 calibration data mentioned, the calibration function was obtained by fitting with the 3rd order polynomials, in order to convert the unit of cm to the unit of Tm, as

$$B\rho\ [\mathrm{Tm}] = 0.7679 + 5.579 \times 10^{-4}x - 1.604 \times 10^{-6}x^{2} + 1.304 \times 10^{-8}x^{3} \quad . \tag{5.3}$$

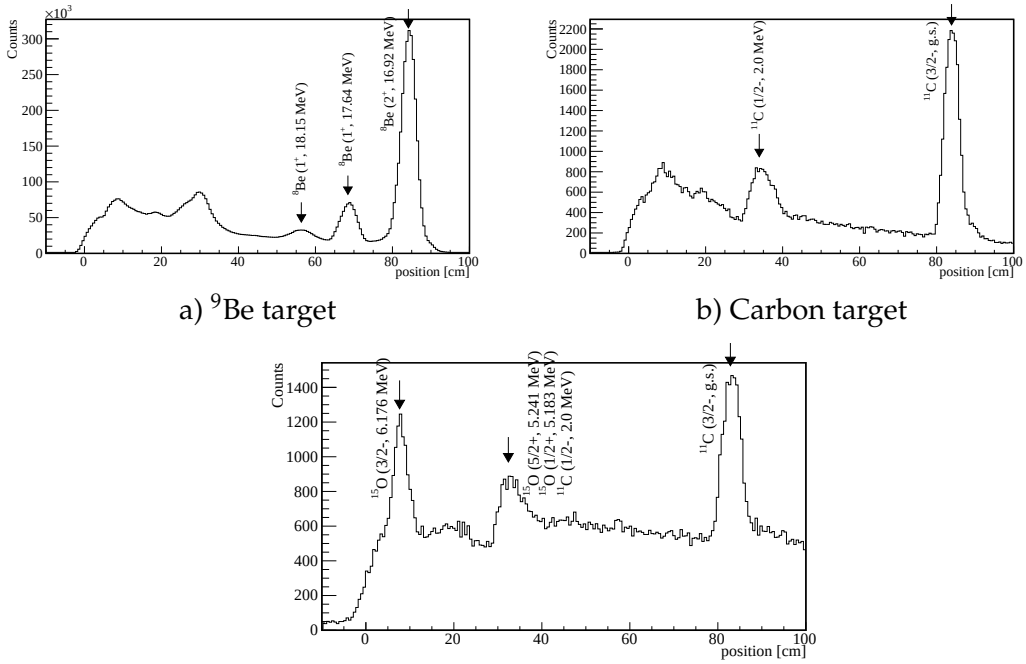

a) ^{9}Be target

b) Carbon target

c) Mylar target

FIGURE 5.4: α particle spectrum at the focal plane obtained from the measurement runs with ^{9}Be, carbon and mylar targets.

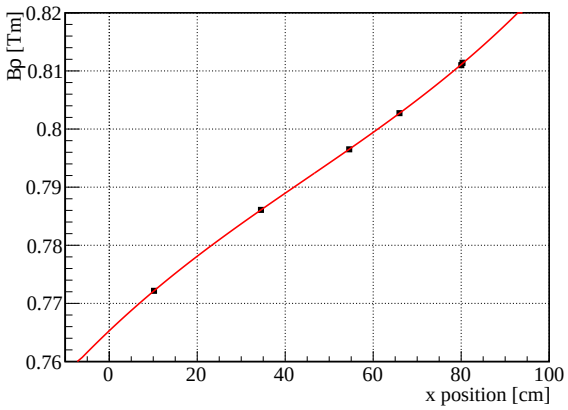

FIGURE 5.5: Calibration curve to convert the unit of length to the one of magnetic rigidity.

5.1.4 Background

In Fig. 5.4 a), background signals due to the ^{12}C and ^{16}O contaminants in the ^{9}Be target are mixed as well. In order to evaluate the background signals, the spectra shown in Fig. 5.4 b) and c) were multiplied by the factors derived in comparison with the measurement run with ^{9}Be target as follows: 1) the abundance ratios which are, respectively, 1.1 % and 1.6 % for ^{12}C and ^{16}O, 2) the total beam counts and 3) the target thickness. As a result, the total background ratio due to the contaminant was about 3% near the 18.91 MeV resonance peak, and about 1% for the higher energy region. Since those background signals due to carbon and oxygen contaminants can be excluded in analysis with a gate condition at SSD, it was judged that they can be neglected in the subsequent analysis. [37]

5.1.5 Excitation Energy Spectrum

Using the magnetic rigidity of α particles, the excitation energy E_X of ^{8}Be was calculated event by event regarding the invariant mass of the ^{9}Be(^{3}He, α)^{8}Be reaction. The calculation was done with an assumption that the scattering angle of α particle is at zero degree. As a result, the position information of α particles was converted to the excitation energy of ^{8}Be in MeV as shown in Fig. 5.6. The arrows represent the resonances of ^{8}Be even if they are not seen as peaks clearly.

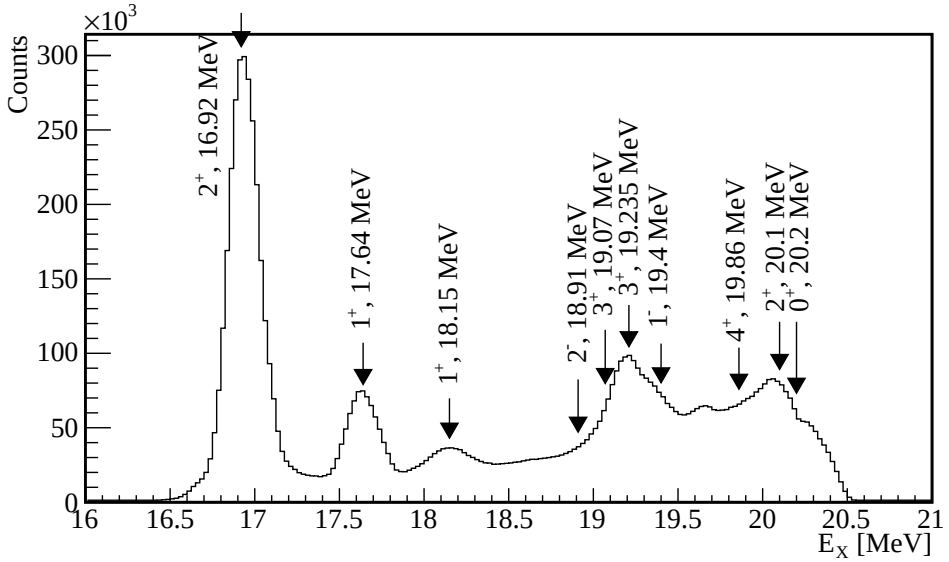

FIGURE 5.6: Excitation energy spectrum. Arrows indicate the resonances of ^{8}Be

5.2 E-ToF Correlation at SSD

In the sequential decay reaction, resonance states of ^{8}Be decay through gamma, proton, neutron and alpha channels. In addition to these decay particles, elastically/inelastically scattering ^{3}He particles are detected at the SSD strips. The particle identification can be carried out by measuring the energy loss and the time-of-flight (ToF) of particles. The ToF is given by

$$ToF = \frac{L}{\beta} \quad , \tag{5.4}$$

where L is the flight length and β is the speed. Together with the notation of energy loss, $\Delta E \propto z^2/\beta^2$, a correlation between ToF and energy loss allows to identify particles. In our measurement, the ToF of decay particles are determined by the time difference between the plastic scintillator and the CFD output of SSD strips as shown in Fig. 5.7.

In this particle identification, the difference in the decay channels of each resonance state of ^{8}Be [20, 21] was used as a gate condition: ^{8}Be(2^{+}, 16.92 MeV) is reported to decay only through α and γ channels according to Table 3.1. Therefore, the E-ToF diagram plotting the data measured simultaneously with the event satisfying the cut condition of E_X from 16.8 MeV to 17.2 MeV should show the distribution of α and ^{3}He particles. Fig. 5.8 a) shows the corresponding chart which has a peak on the right upper side. It can be understood that this peak is populated by α particles by changing the cut condition to include ^{8}Be(1^{+}, 17.64 MeV) and ^{8}Be(1^{+}, 19.4 MeV) events instead. These resonances are reported to decay only through γ and proton channels. Fig. 5.8 b) and c) show the result in which the α peak almost vanished and there is a new peak in the left upper side. This can be considered as protons. The peak in b) corresponds to the proton decay leading to the ground state of ^{7}Li. The peak in c) contains both proton events leading to the ground state and 1st excited state of ^{7}Li. Therefore, the gated area was taken for the ToF range from 300 nsec to 350 nsec with respect to the vertical axis, and for the energy range from 0.4 MeV to 5 MeV with respect to the horizontal axis in the Fig. 5.8 d), respectively.

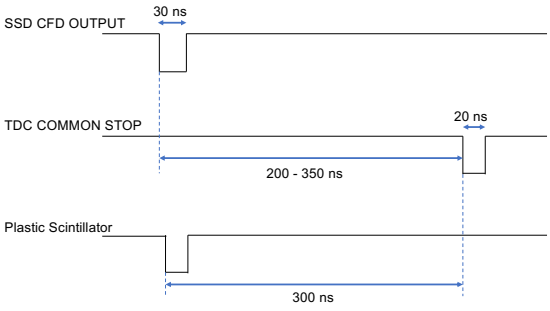

FIGURE 5.7: TDC adjustment

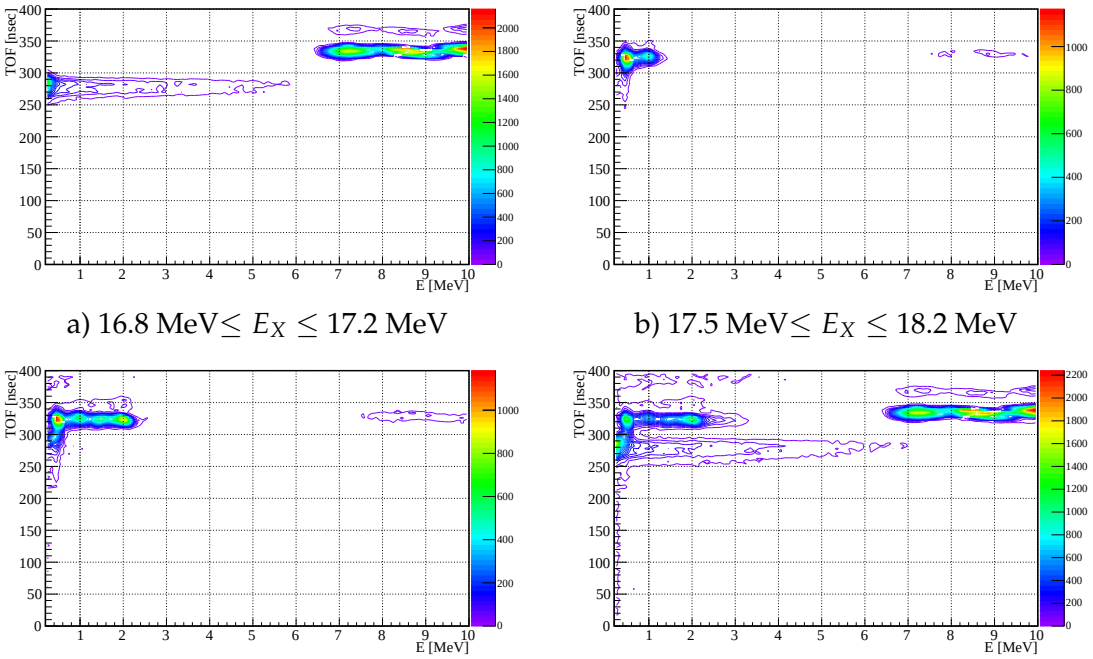

a) 16.8 MeV$\leq E_X \leq$ 17.2 MeV

b) 17.5 MeV$\leq E_X \leq$ 18.2 MeV

c) 17.5 MeV$\leq E_X \leq$ 19.4 MeV

d) 16.8 MeV$\leq E_X$

FIGURE 5.8: $E - ToF$ gated

5.3 Result and Analysis

Diagrams of correlation between the excitation energy E_X of ^{8}Be and the energy of decay-proton measured in coincidence are shown in Fig. 5.9 - 5.11. The former variable corresponds to the horizontal axis and the latter to the vertical axis, and both axises are given in the unit of MeV. Especially in the diagrams of SSDA strips, two curves going up to the right can be observed. The upper curve corresponds to the proton-decay to the ground state of ^{7}Li (p_0 events), and the lower curve corresponds to the proton-decay to the first excited state (p_1 events), which is the target of our experiment. This p_1 events are for the first time separated clearly and observed in our measurement. In the diagram of SSDB, the yields at strip-1 and strip-2 are too low and the resolution at strip-3 is terribly bad, thus they will be excluded from further analysis.

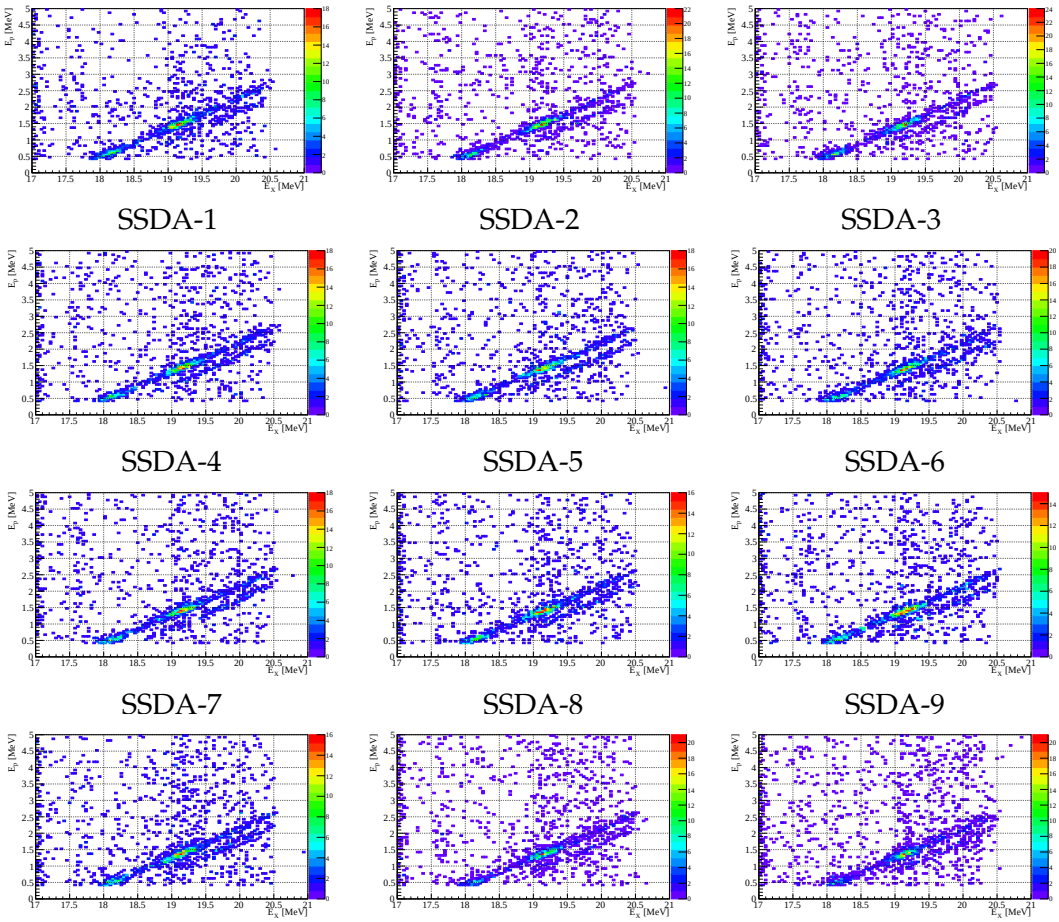

FIGURE 5.9: SSDA Results

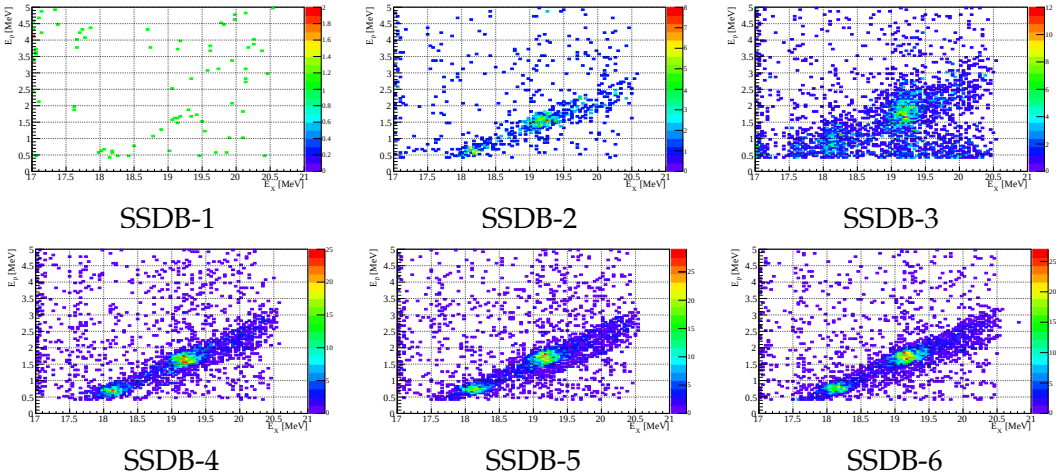

FIGURE 5.10: SSDB Results

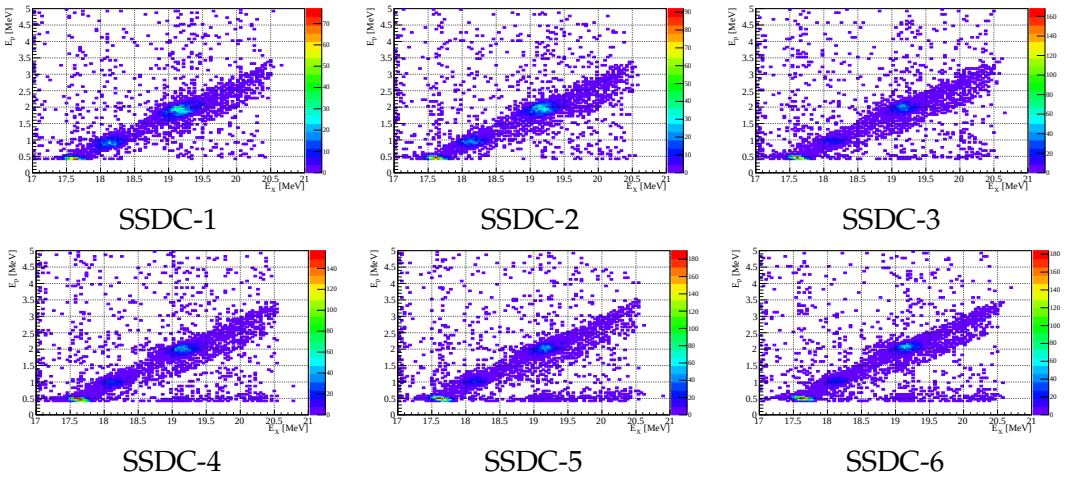

FIGURE 5.11: SSDC Results

5.3.1 ^{7}Li Excitation Energy

The population of ^{7}Li states lead by the proton-decays of each excited state of ^{8}Be is of interest. First of all, the scale of the vertical axis will be converted in order to make it more convenient for further analysis. From the two body kinematics of the sequential decay reaction ($^{8}\mathrm{Be}^{*} \rightarrow {}^{7}\mathrm{Li} + p$), the excitation energy E'_X of ^{7}Li can be deduced under the assumption that the residual ^{8}Be nucleus recoils backward to the beam direction in average at 180° (which is the same assumption that the scattering angle of α particle is at zero degree in the initial reaction). Then, E'_X is given by the function of three measurable quantities; $B\rho$ of α particles, the kinetic energy E_p and the scattering angle θ_p of decay-protons in the laboratory system. The function is given by

$$E'_X = \sqrt{(m_{^8\mathrm{Be}} + E_X)^2 + m_p^2 - 2\cdot(m_p + E_p)\cdot E_{^8\mathrm{Be}} - 2\sqrt{(E_{^8\mathrm{Be}})^2 - (m_{^8\mathrm{Be}} + E_X)^2}\cdot\sqrt{E_p\,(E_p + 2m_p)}\cdot\cos\theta_p} - m_{^7\mathrm{Li}}\ , \quad (5.5)$$

where E_X and $E_{^8\mathrm{Be}}$ are, respectively, the excitation energy and the total energy of ^{8}Be which both can be calculated by using the magnetic rigidity $B\rho$ of α particle. The angle θ_p takes the values of SSD strip angles listed in Table 4.3, depending on the strips at which decay-protons are detected. The calculation was done for event by event in the offline analysis. Then, all the vertical axis in Fig. 5.9 - 5.11 were replaced by the excitation energy of ^{7}Li as the resulting diagrams are shown in Fig. 5.12 - 5.14.

It will be clearer to project the data in the range of E_X greater than 18.7 MeV with respect to the horizontal axis to the vertical axis, to see the population of the states of ^{7}Li by the proton-decays. The resulting histograms are shown in Fig. 5.15 - 5.17. Two peaks can be seen in each spectrum which correspond to the ground state and the first excited state ($E'_X = 0.478$ MeV) of ^{7}Li. Therefore, we have succeeded in measuring the proton-decay events of ^{8}Be resonances both to the ground and first excited states of ^{7}Li separately in our measurements.

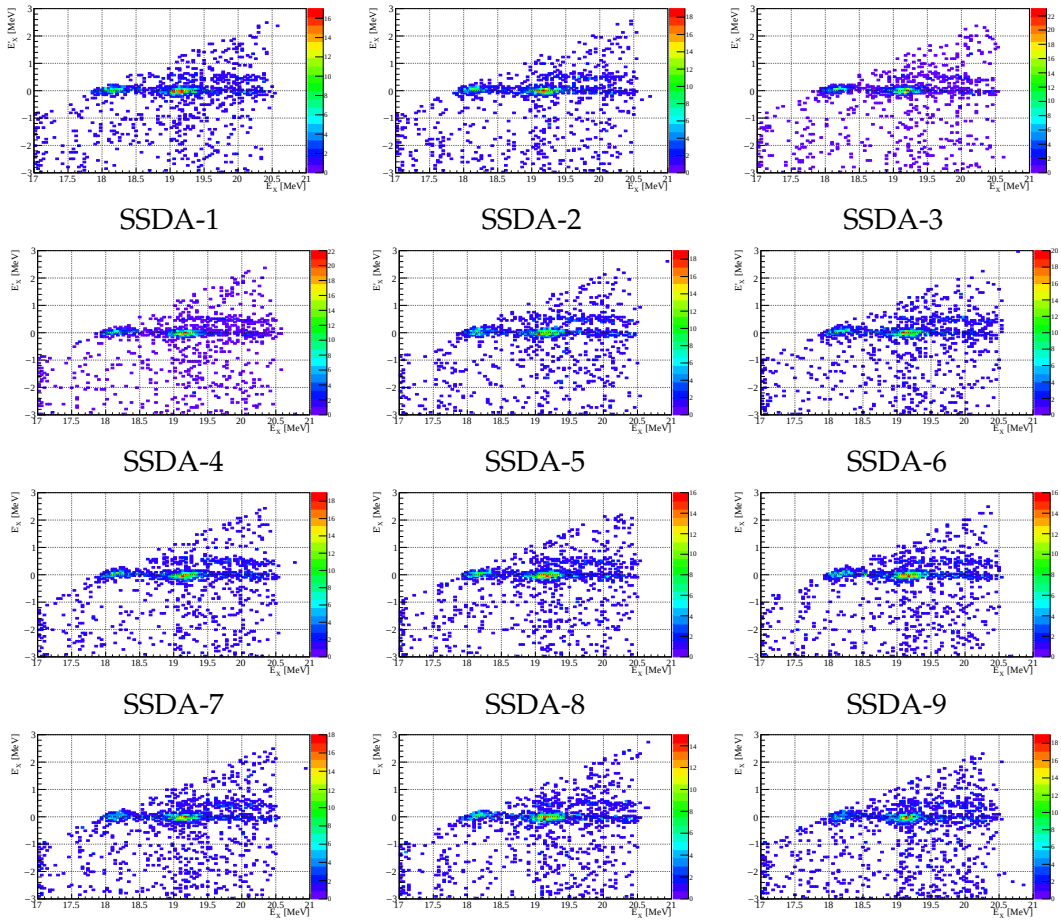

FIGURE 5.12: SSDA Results

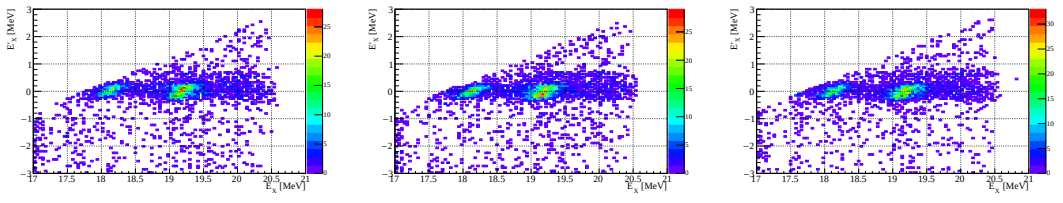

FIGURE 5.13: SSDB Results

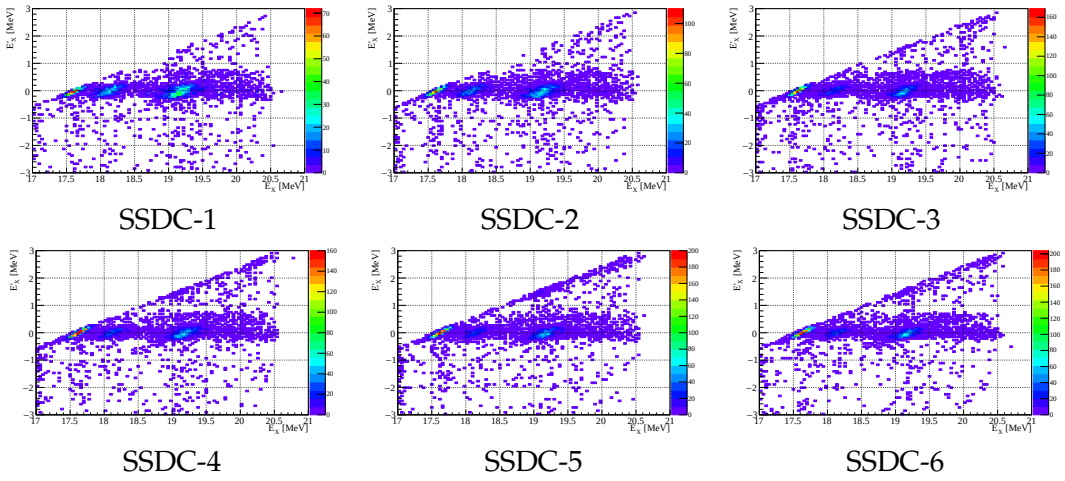

FIGURE 5.14: SSDC Results

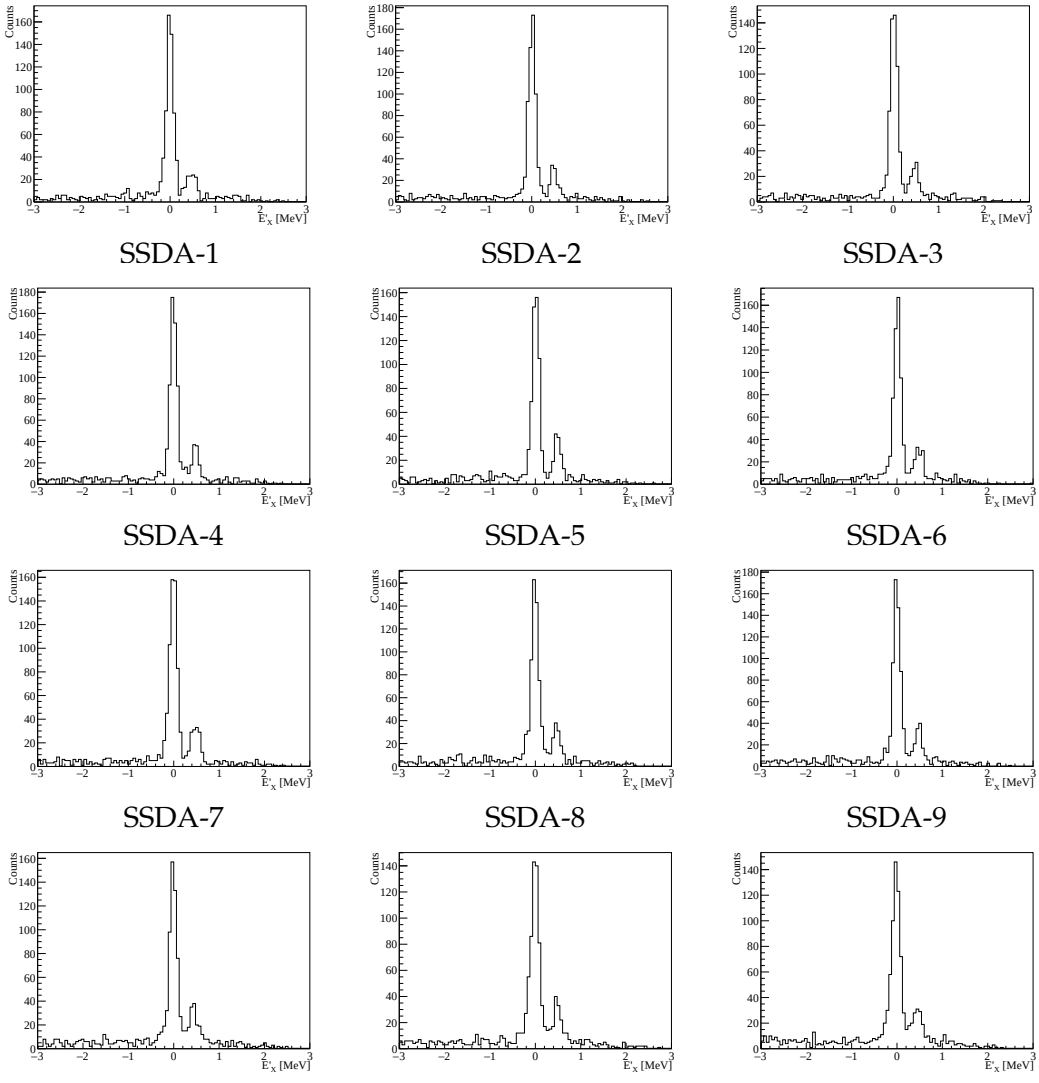

SSDA-1 SSDA-2 SSDA-3

SSDA-4 SSDA-5 SSDA-6

SSDA-7 SSDA-8 SSDA-9

SSDA-10 SSDA-11 SSDA-12

FIGURE 5.15: SSDA Results

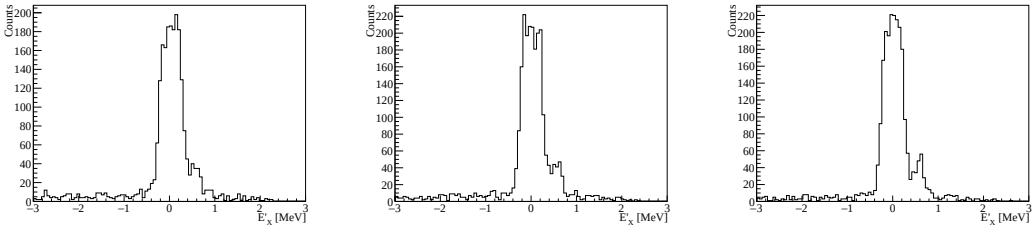

SSDB-4 SSDB-5 SSDB-6

FIGURE 5.16: SSDB Results

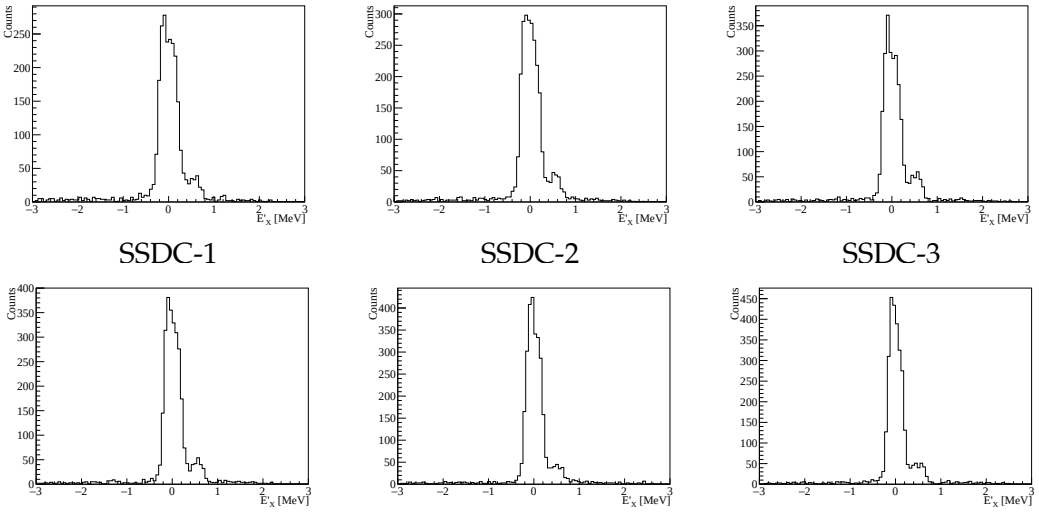

SSDC-1 SSDC-2 SSDC-3

SSDC-4 SSDC-5 SSDC-6

FIGURE 5.17: SSDC Results

5.3.2 Angular Distribution

The differential cross section $d^2\sigma/d\Omega_\alpha dE_X$ in the rest frame of ^{8}Be will be deduced. For the further analysis, due to the low yields at each single SSD strip, data taken at SSDA strip 1-6, 7-12, SSDB strip 4-6, SSDC strip 1-3 and 4-6 were combined together into 5 groups to obtain angular distribution.

The same as in the previous subsection, histograms of the excitation energy E'_X of ^{7}Li were made for each E_X range of ^{8}Be sliced every 100 keV bins from 18.75 MeV to 20.35 MeV for each of combined strip groups. Then, the histograms were fitted with the double Gaussians plus a constant to obtain the yields $Y_{g.s}$ and Y_{1st} of p_0 and p_1 events. By using the yields obtained, the differential cross section in the laboratory system is deduced as

$$\frac{d^3\sigma}{d\Omega^2 dE_X} = \frac{Y_{g.s(1st)}}{N_b \times N_t \times d\Omega_\alpha \times d\Omega_p} \ \ [\mu b/sr^2/100\ \text{keV}] \quad . \tag{5.6}$$

N_b is the total number of beam particles calculated from the counts of the silicon telescope detector which were calibrated with the faraday cup,

$$\begin{aligned} N_b &= (\text{Faraday cup count}) \times 10^{-10} \times \frac{1}{\text{z} \times \text{e}} \\ &= 16206589 \times 10^{-10} \times \frac{1}{2 \times 1.6 \times 10^{-19}} \\ &= 4.96 \times 10^{15} \quad . \end{aligned} \tag{5.7}$$

The number of target particle in a unit surface N_t [/cm^2] is defined as

$$N_t = \frac{\rho \times N_A}{A} \quad , \tag{5.8}$$

where $\rho = 185\ \mu$g/cm^2 is the areal density of 1 μm thick ^{9}Be target, $N_A = 6.02 \times 10^{23}$ is the Avogadro's number and $A = 9$ is the mass number. Considering that the target

is inclined 45° with respect to the beam direction, it yields

$$N_t = 1.75 \times 10^{19} \ [/\mathrm{cm}^2] \quad . \tag{5.9}$$

$d\Omega_\alpha$ is the solid angle of the entrance of ENMA spectrograph which was opened for $\pm 2^\circ$ wide and $\pm 3^\circ$ high, thus it is given by

$$d\Omega_\alpha = 4 \times \sin^{-1}\left(\sin(2^\circ \times \frac{\pi}{180^\circ})\sin(3^\circ \times \frac{\pi}{180^\circ})\right) = 7.31 \times 10^{-3} \ [\mathrm{sr}] \quad . \tag{5.10}$$

The $d\Omega_p$ is the solid angle of the half surface of each SSD. It is given by

$$d\Omega_p = 7.69 \times 10^{-2} \ [\mathrm{sr}] \tag{5.11}$$

for SSDA, and

$$d\Omega_p = 1.18 \times 10^{-1} \ [\mathrm{sr}] \tag{5.12}$$

for SSDB and SSDC, respectively.

Using the deduced differential cross section in the laboratory system, the procedure of converting it to that in the rest frame of ^{8}Be will be described below. Note that it is assumed that ^{8}Be moves backward with respect to the beam direction at 180°. The subscript *lab* and *cm* represent the laboratory system and the rest frame of ^{8}Be, respectively.

The scattering angle of decay-protons in the center-of-mass system is given by

$$\theta_p^{cm} = \tan^{-1}\left(\frac{\sin\theta_p^{lab}}{\cos\theta_p^{lab} - \beta_G^{lab}/\beta_p^{lab}}\right) \quad , \tag{5.13}$$

where β_G^{lab} is the velocity of ^{8}Be, θ_p^{lab} and β_p^{lab} are the scattering angle and the velocity of decay-proton. The relation between the differential cross section in the laboratory system and that in the rest frame of ^{8}Be is given by

$$\left(\frac{d^3\sigma}{d\Omega^2 dE_X}\right)_{cm} = \left(\frac{d^3\sigma}{d\Omega^2 dE_X}\right)_{lab} \times |J| \quad . \tag{5.14}$$

The variable J is a jacobian which arises from the kinematical requirement in the transformation of two different frames. It is given by

$$|J| = \frac{|1 + \gamma\cos\theta_p^{cm}|}{(1 + 2\gamma\cos\theta_p^{cm} + \gamma^2)^{3/2}} \quad , \tag{5.15}$$

where γ is the fraction between the velocity of decay protons and that of ^{8}Be, which is $\gamma = \beta_G^{lab}/\beta_p^{cm}$. The variables defined in Eq. (5.13) and Eq. (5.15) were calculated for event by event, and the mean values were used for the transformation.

The results of this transformation are shown in Fig. 5.18 - 5.25. The red curve in each graph represents a series of Legendre polynomials up to third order which was applied for the fitting to the angular distribution. The function is given by

$$\left(\frac{d^3\sigma}{d\Omega^2 dE_X}\right)_{cm} = \sum_{L=0}^{3} A_L P_L(\cos\theta_p^{cm}) \quad , \tag{5.16}$$

where

$$
\begin{aligned}
P_0 &= 1 \\
P_1 &= \cos\theta_p^{cm} \\
P_2 &= \frac{1}{2}(3\cos^2\theta_p^{cm} - 1) \\
P_3 &= \frac{1}{2}(5\cos^3\theta_p^{cm} - 3\cos\theta_p^{cm}) \quad .
\end{aligned}
\tag{5.17}
$$

The fitting results of the coefficients A_L are listed in Table 5.1.

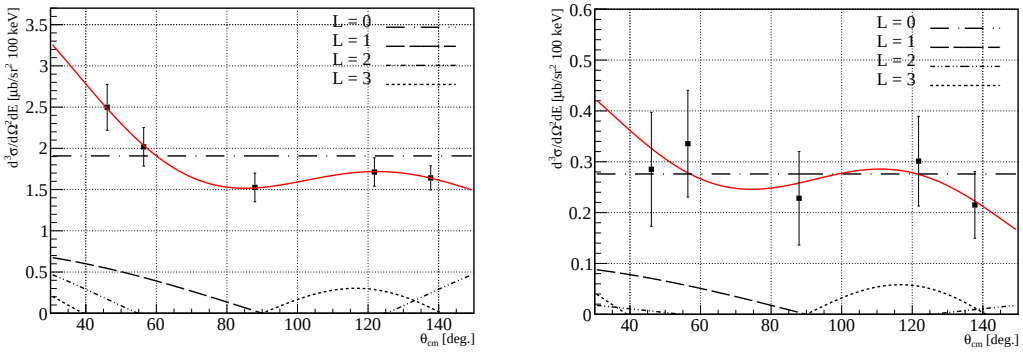

a) ground state b) 1st ex. state

FIGURE 5.18: Differential Cross Sections in CM system for $18.75 \leq {}^{8}\mathrm{Be} \leq 18.85$ MeV

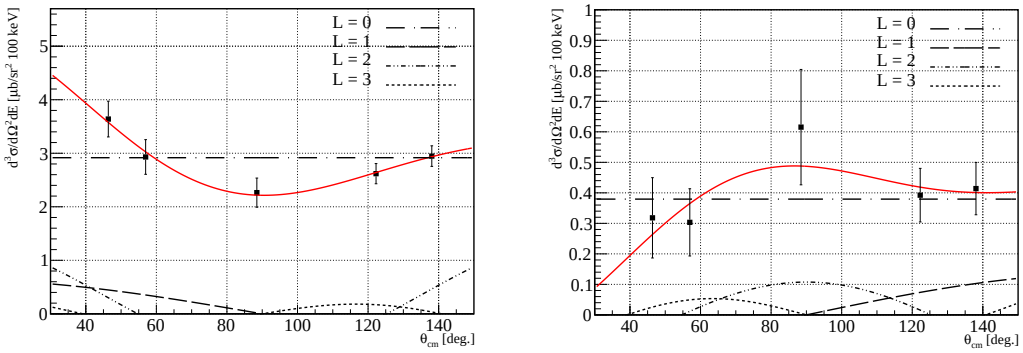

a) ground state b) 1st ex. state

FIGURE 5.19: Differential Cross Sections in CM system for $18.85 \leq {}^{8}\mathrm{Be} \leq 18.95$ MeV

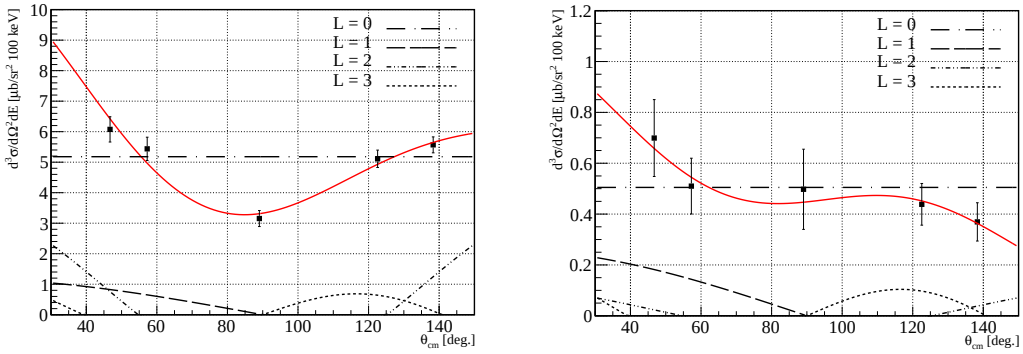

a) ground state b) 1st ex. state

FIGURE 5.20: Differential Cross Sections in CM system for 18.95 $\leq$ ^{8}Be $\leq$ 19.05 MeV

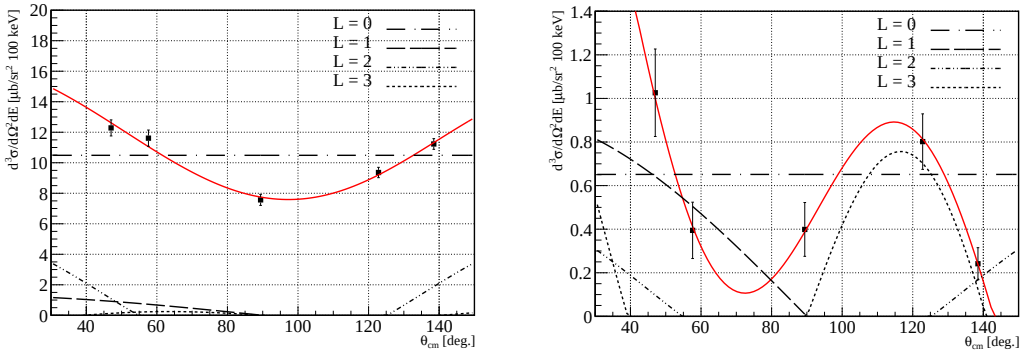

a) ground state b) 1st ex. state

FIGURE 5.21: Differential Cross Sections in CM system for 19.05 $\leq$ ^{8}Be $\leq$ 19.15 MeV

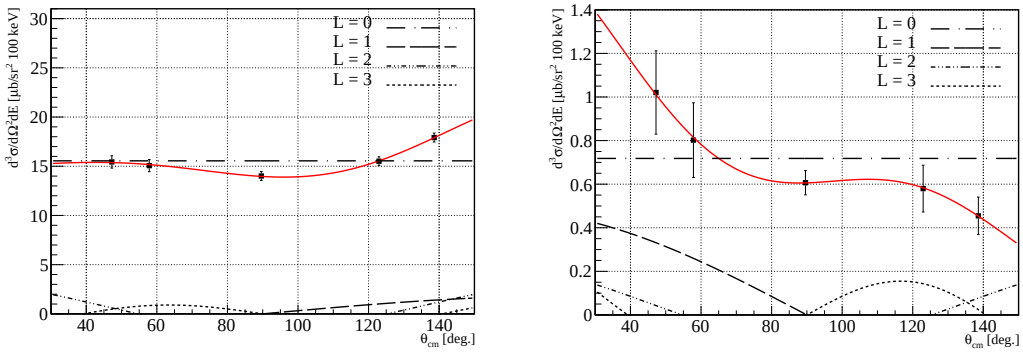

a) ground state b) 1st ex. state

FIGURE 5.22: Differential Cross Sections in CM system for 19.15 $\leq$ ^{8}Be $\leq$ 19.25 MeV

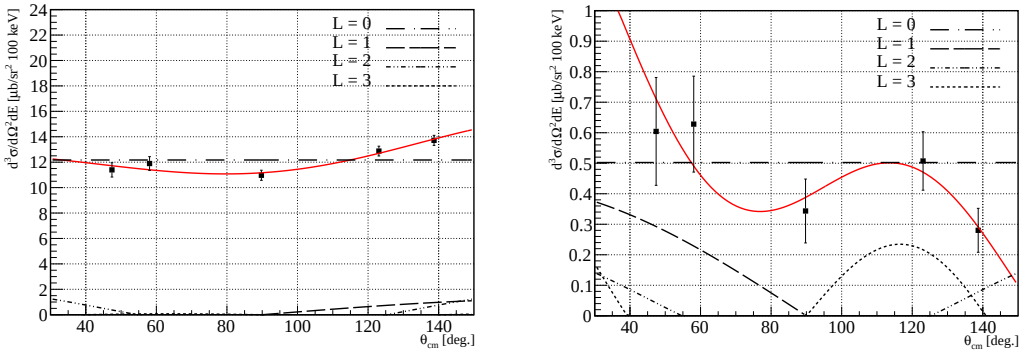

a) ground state b) 1st ex. state

FIGURE 5.23: Differential Cross Sections in CM system for $19.25 \leq {}^{8}\text{Be} \leq 19.35$ MeV

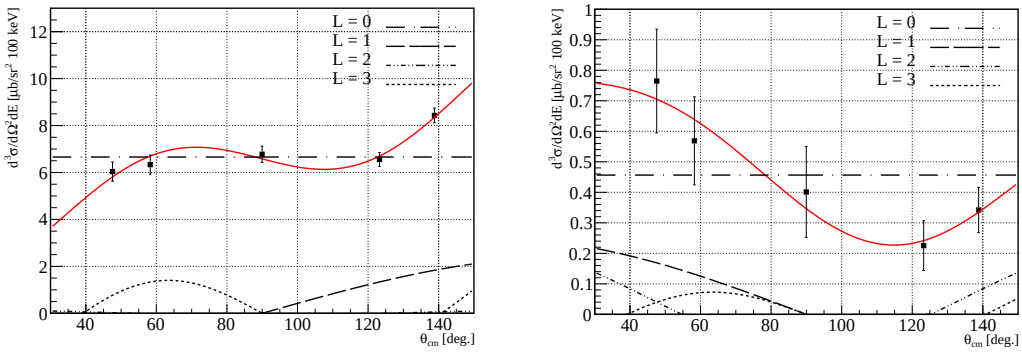

a) ground state b) 1st ex. state

FIGURE 5.24: Differential Cross Sections in CM system for $19.35 \leq {}^{8}\text{Be} \leq 19.45$ MeV

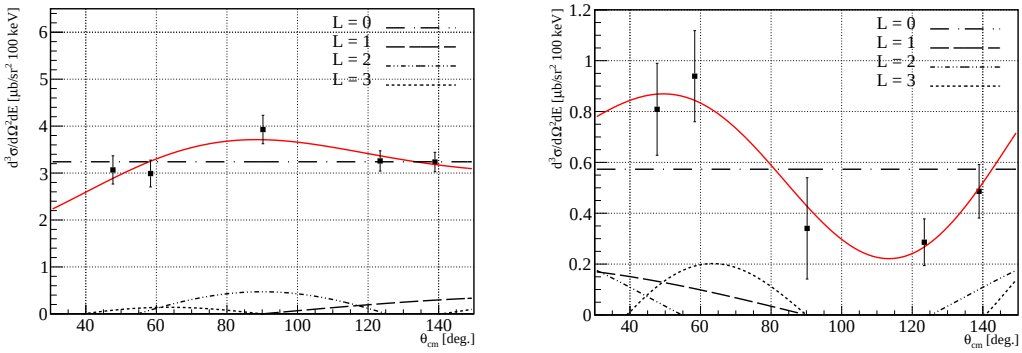

a) ground state b) 1st ex. state

FIGURE 5.25: Differential Cross Sections in CM system for $19.45 \leq {}^{8}\text{Be} \leq 19.55$ MeV

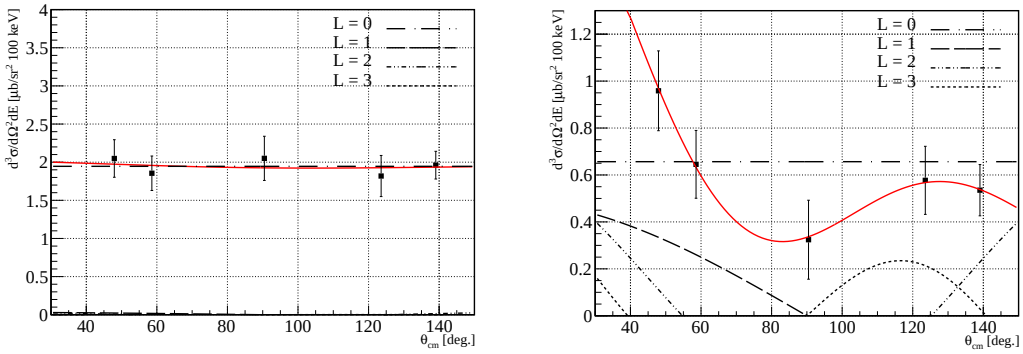

a) ground state b) 1st ex. state

FIGURE 5.26: Differential Cross Sections in CM system for $19.55 \leq {}^{8}\text{Be} \leq 19.65$ MeV

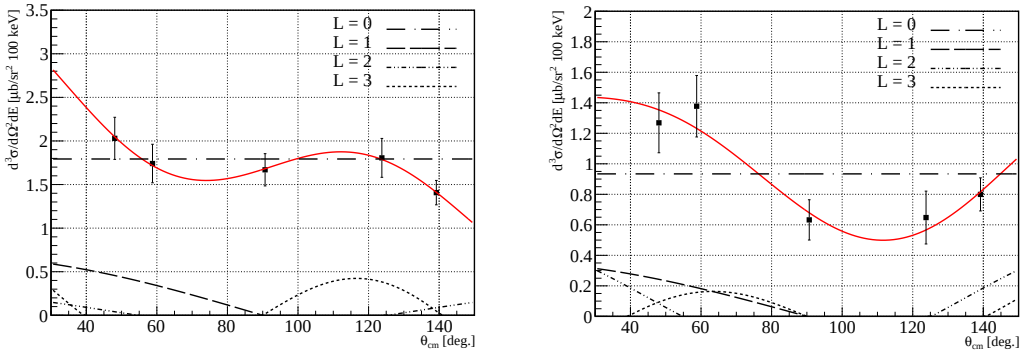

a) ground state b) 1st ex. state

FIGURE 5.27: Differential Cross Sections in CM system for $19.65 \leq {}^{8}\text{Be} \leq 19.75$ MeV

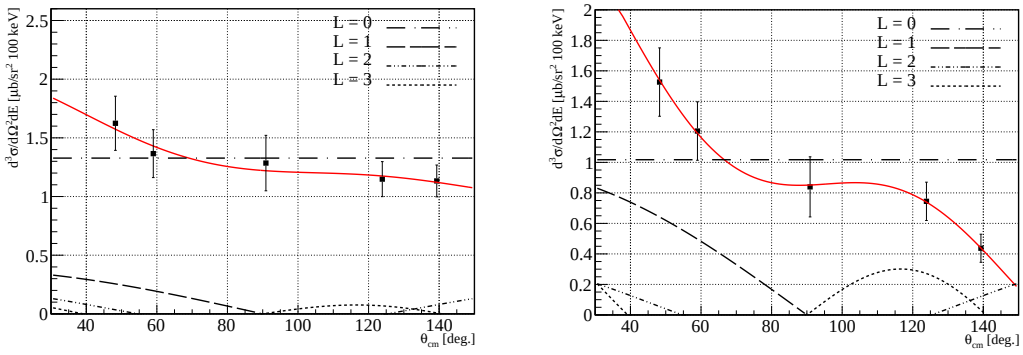

a) ground state b) 1st ex. state

FIGURE 5.28: Differential Cross Sections in CM system for $19.75 \leq {}^{8}\text{Be} \leq 19.85$ MeV

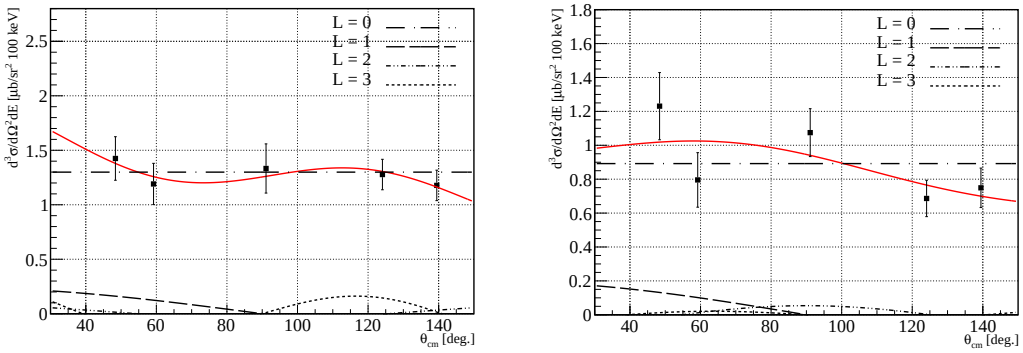

a) ground state b) 1st ex. state

FIGURE 5.29: Differential Cross Sections in CM system for $19.85 \leq {}^{8}\text{Be} \leq 19.95$ MeV

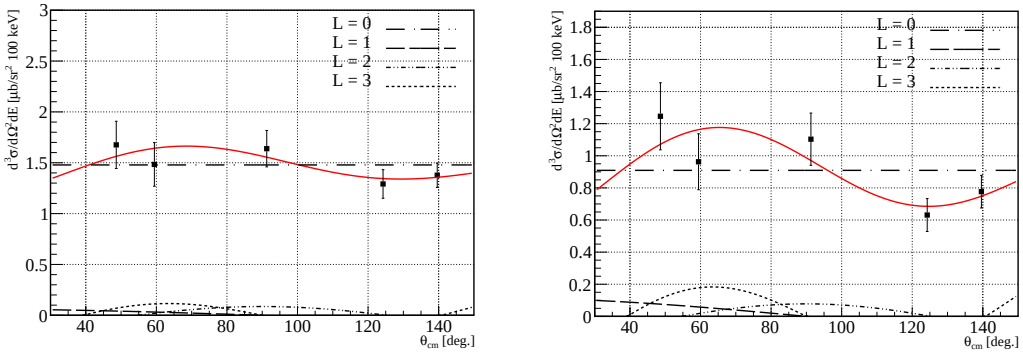

a) ground state b) 1st ex. state

FIGURE 5.30: Differential Cross Sections in CM system for $19.95 \leq {}^{8}\text{Be} \leq 20.05$ MeV

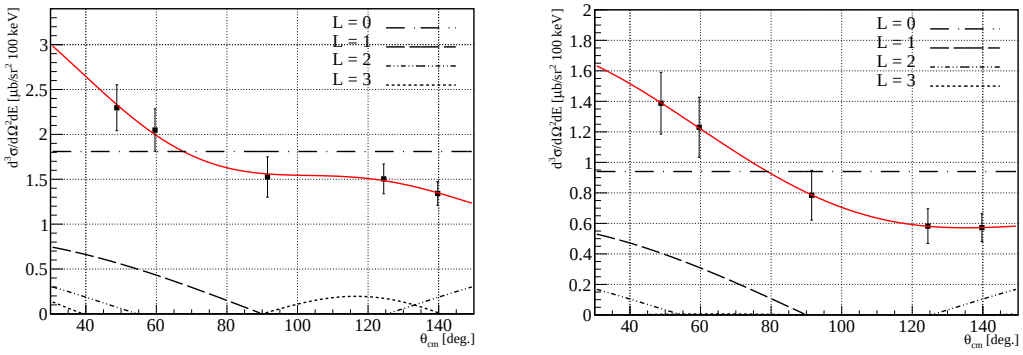

a) ground state b) 1st ex. state

FIGURE 5.31: Differential Cross Sections in CM system for $20.05 \leq {}^{8}\text{Be} \leq 20.15$ MeV

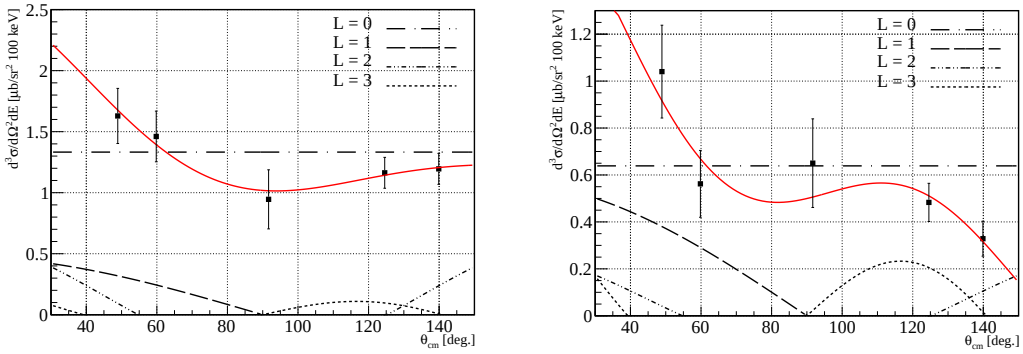

a) ground state b) 1st ex. state

FIGURE 5.32: Differential Cross Sections in CM system for $20.15 \leq {}^{8}\text{Be} \leq 20.25$ MeV

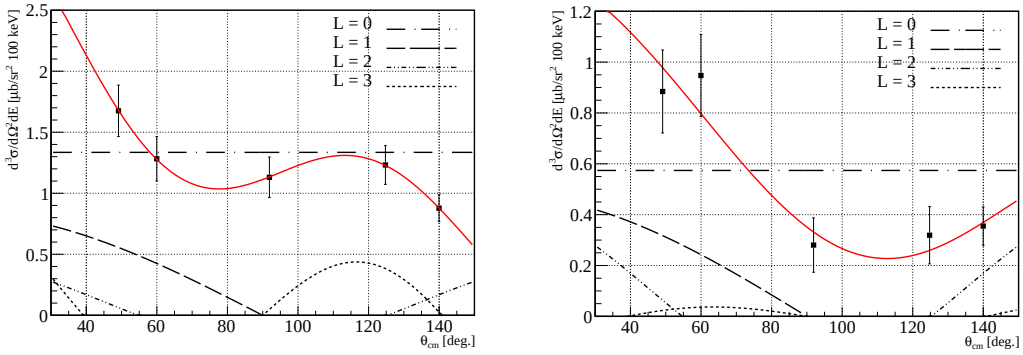

a) ground state b) 1st ex. state

FIGURE 5.33: Differential Cross Sections in CM system for $20.25 \leq {}^{8}\text{Be} \leq 20.35$ MeV

TABLE 5.1: Legendre Coefficients

$^8Be^* \rightarrow {}^7Li + p_0$				
E_X (MeV)	A_0	A_1	A_2	A_3
18.75-18.85	1.91 ± 0.10	0.78 ± 0.29	0.76 ± 0.31	0.68 ± 0.55
18.85-18.95	2.92 ± 0.12	0.65 ± 0.37	1.41 ± 0.45	0.41 ± 0.67
18.95-19.05	5.18 ± 0.16	1.20 ± 0.48	3.70 ± 0.50	1.53 ± 0.91
19.05-19.15	10.49 ± 0.20	1.35 ± 0.63	5.52 ± 0.67	-0.55 ± 1.16
19.15-19.25	15.55 ± 0.25	-1.86 ± 0.80	3.18 ± 0.84	-2.01 ± 1.48
19.25-19.35	12.17 ± 0.22	-1.28 ± 0.71	2.01 ± 0.75	-0.16 ± 1.29
19.35-19.45	6.66 ± 0.17	-2.44 ± 0.54	0.16 ± 0.61	-3.14 ± 1.00
19.45-19.55	3.24 ± 0.12	-0.39 ± 0.39	-0.94 ± 0.50	-0.31 ± 0.72
19.55-19.65	1.95 ± 0.12	0.03 ± 0.35	0.04 ± 0.45	4.15e-3$\pm$0.72
19.65-19.75	1.79 ± 0.11	0.68 ± 0.31	0.24 ± 0.35	0.95 ± 0.63
19.75-19.85	1.33 ± 0.09	0.38 ± 0.30	0.21 ± 0.39	0.17 ± 0.52
19.85-19.95	1.30 ± 0.09	0.24 ± 0.27	0.09 ± 0.37	0.36 ± 0.49
19.95-20.05	1.48 ± 0.09	0.06 ± 0.28	-0.17 ± 0.34	-0.26 ± 0.49
20.05-20.15	1.81 ± 0.11	0.86 ± 0.32	0.49 ± 0.41	0.44 ± 0.57
20.15-20.25	1.33 ± 0.09	0.49 ± 0.30	0.63 ± 0.41	0.24 ± 0.49
20.25-20.35	1.34 ± 0.09	0.85 ± 0.28	0.44 ± 0.33	0.98 ± 0.50
$^8Be^* \rightarrow {}^7Li^*(0.478\ \text{MeV}) + p_1$				
E_X (MeV)	A_0	A_1	A_2	A_3
18.75-18.85	0.28 ± 0.04	0.10 ± 0.13	0.03 ± 0.15	0.13 ± 0.26
18.85-18.95	0.38 ± 0.05	-0.14 ± 0.16	-0.22 ± 0.25	-0.12 ± 0.30
18.95-19.05	0.50 ± 0.05	0.27 ± 0.17	0.11 ± 0.24	0.23 ± 0.30
19.05-19.15	0.65 ± 0.07	0.94 ± 0.21	0.49 ± 0.24	1.69 ± 0.38
19.15-19.25	0.72 ± 0.07	0.49 ± 0.19	0.22 ± 0.16	0.35 ± 0.34
19.25-19.35	0.50 ± 0.06	0.43 ± 0.18	0.23 ± 0.21	0.52 ± 0.32
19.35-19.45	0.46 ± 0.06	0.25 ± 0.19	0.22 ± 0.25	-0.16 ± 0.31
19.45-19.55	0.57 ± 0.07	0.20 ± 0.22	0.29 ± 0.31	-0.45 ± 0.38
19.55-19.65	0.66 ± 0.07	0.50 ± 0.23	0.64 ± 0.28	0.53 ± 0.43
19.65-19.75	0.93 ± 0.09	0.36 ± 0.25	0.49 ± 0.27	-0.37 ± 0.51
19.75-19.85	1.02 ± 0.09	0.96 ± 0.26	0.33 ± 0.35	0.67 ± 0.44
19.85-19.95	0.89 ± 0.07	0.20 ± 0.24	-0.11 ± 0.28	-0.05 ± 0.40
19.95-20.05	0.91 ± 0.08	0.11 ± 0.25	-0.16 ± 0.31	-0.41 ± 0.39
20.05-20.15	0.94 ± 0.08	0.62 ± 0.24	0.27 ± 0.31	-0.01 ± 0.41
20.15-20.25	0.64 ± 0.07	0.58 ± 0.23	0.28 ± 0.33	0.52 ± 0.34
20.25-20.35	0.57 ± 0.07	0.49 ± 0.20	0.45 ± 0.23	-0.08 ± 0.37

TABLE 5.2: Cross Section

REACTION		^{9}Be(^{3}He, α)^{8}Be*(p_0)^{7}Li	^{9}Be(^{3}He, α)^{8}Be*(p_1)^{7}Li*(0.478 MeV)
E_X	Mean E_X	$\frac{d^2\sigma}{d\Omega dE}$	$\frac{d^2\sigma}{d\Omega dE}$
[MeV]	[MeV]	$[\mu b/sr/100\ keV]$	$[\mu b/sr/100\ keV]$
18.75-18.85	18.8	23.98 ± 1.21	3.47 ± 0.55
18.85-18.95	18.9	36.65 ± 1.54	4.77 ± 0.65
18.95-19.05	19.0	65.09 ± 1.96	6.34 ± 0.65
19.05-19.15	19.1	131.79 ± 2.54	8.18 ± 0.87
19.15-19.25	19.2	195.40 ± 3.15	8.69 ± 0.85
19.25-19.35	19.3	152.95 ± 2.78	6.31 ± 0.79
19.35-19.45	19.4	83.68 ± 2.11	5.74 ± 0.76
19.45-19.55	19.5	40.72 ± 1.57	7.20 ± 0.87
19.55-19.65	19.6	24.45 ± 1.53	8.25 ± 0.93
19.65-19.75	19.7	22.53 ± 1.35	11.74 ± 1.07
19.75-19.85	19.8	16.68 ± 1.17	12.78 ± 1.07
19.85-19.95	19.9	16.33 ± 1.07	11.21 ± 0.93
19.95-20.05	20.0	18.58 ± 1.16	11.43 ± 0.97
20.05-20.15	20.1	22.74 ± 1.33	11.81 ± 1.01
20.15-20.25	20.2	16.75 ± 1.14	8.03 ± 0.87
20.25-20.35	20.3	16.78 ± 1.16	7.21 ± 0.87

5.3.3 Differential Cross Section in the Rest Frame of ^{8}Be

With the coefficients obtained in the previous subsection, the integrated cross section over the solid angle Ω_p of decay-proton can be deduced as

$$\frac{d^2\sigma}{d\Omega_\alpha dE_X} = \int d\Omega_p \sum_{L=0}^{3} A_L P_L(\cos\theta_p^{cm}) \quad . \tag{5.18}$$

The deduced differential cross sections are listed in Table 5.2, and the data are plotted in Fig. 5.34(a) and (b) as a function of the excitation energy E_X for the reactions of ^{9}Be(^{3}He, α)^{8}Be*(p_0)^{7}Li and ^{9}Be(^{3}He, α)^{8}Be*(p_1)^{7}Li*(0.478 MeV), respectively. In Fig. 5.34(c), the ratios of the data in Fig. 5.34(b) divided by the ones in (a) are plotted. The deduced ratio is about 11% around 18.9 MeV, which is much larger than the conclusions of Koehler *et al.* [23]. This may be true, but there may be also a possibility that a new resonance state in ^{8}Be exists just below 18.91 MeV resonance, which causes the enhancement of the proton decay events to the first excited state in ^{7}Li. At 19.2 MeV, near the strongest peak observed in the ^{7}Li(p, n) reaction measurements, the ratio becomes about 5%. A peak of about 79% was observed around 19.8 MeV, which is clearly due to the 19.86 MeV resonance.

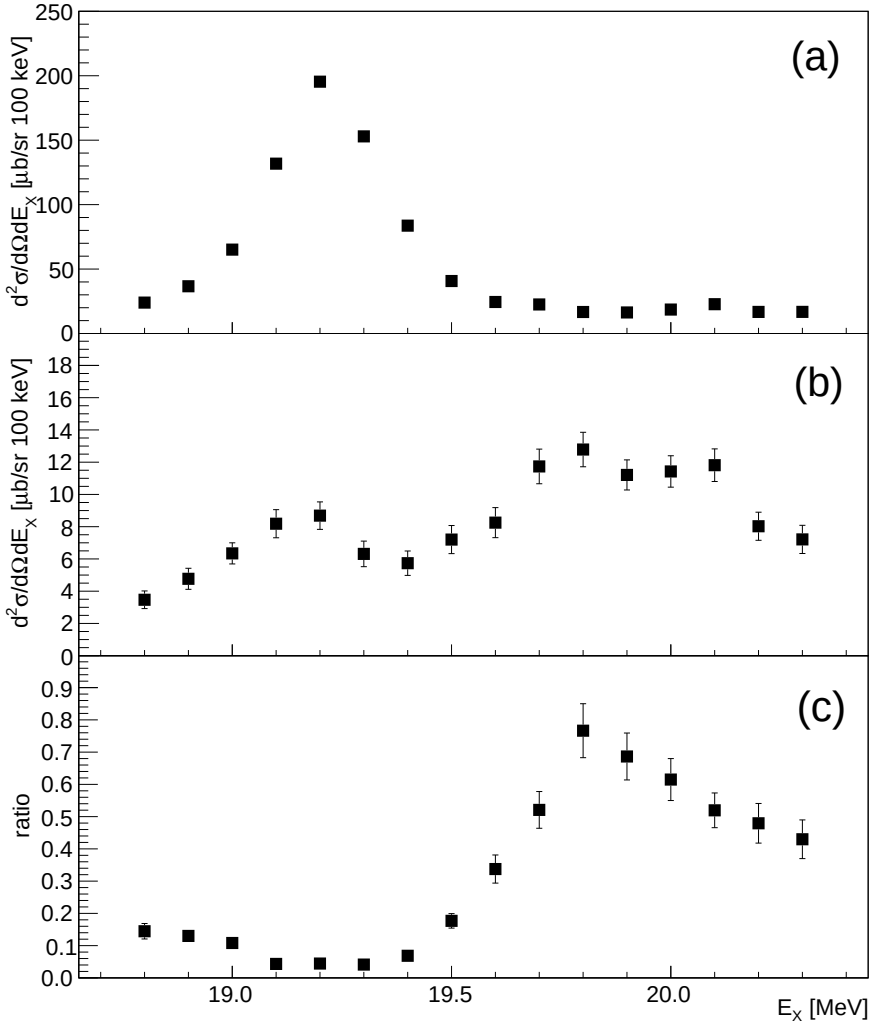

FIGURE 5.34: The differential cross section as a function of the excitation energy of ^{8}Be for (a) the ^{9}Be(^{3}He, α)^{8}Be$^*(p)^7$Li$_{\text{g.s.}}$ reaction and (b) the ^{9}Be(^{3}He, α)^{8}Be$^*(p)^7$Li$_{1\text{st}}$ reaction. (c) Ratio of the data in (b) to the ones in (a).

5.4 Γ_{p1}/Γ_{p0} Ratio

To determine the branching ratio $\Gamma_{p_1}/\Gamma_{p_0}$ for each resonance state of ^{8}Be, the differential cross sections in the rest frame of ^{8}Be plotted in Fig. 5.34(a) and (b) were fitted

with a function represented by the sum of seven single-level Breit-Wigner expressions, which is given by

$$\begin{aligned} f(E) =& \frac{A_{18.91}}{(E-18.91)^2+(\Gamma_{18.91}/2)^2} + \frac{A_{19.07}}{(E-19.07)^2+(\Gamma_{19.07}/2)^2} \\ &+ \frac{A_{19.235}}{(E-19.235)^2+(\Gamma_{19.235}/2)^2} + \frac{A_{19.4}}{(E-19.4)^2+(\Gamma_{19.4}/2)^2} \\ &+ \frac{A_{19.86}}{(E-19.86)^2+(\Gamma_{19.86}/2)^2} + \frac{A_{20.1}}{(E-20.1)^2+(\Gamma_{20.1}/2)^2} \\ &+ \frac{A_{20.2}}{(E-20.2)^2+(\Gamma_{20.2}/2)^2} \end{aligned} \tag{5.19}$$

Γ are the total widths of the resonance states of ^{8}Be whose values are given in Table 4.5. In the fitting, the table values were taken as the initial values, and each of the Γs was allowed to fluctuate within the uncertainty reported by NNDC [21] as

$$\begin{aligned} \Gamma_{18.91} &= 0.122 \quad (fixed) \\ 0.25 \leq& \Gamma_{19.07} \leq 0.29 \\ 0.211 \leq& \Gamma_{19.235} \leq 0.243 \\ \Gamma_{19.4} &\approx 0.645 \\ 0.6 \leq& \Gamma_{19.86} \leq 0.8 \\ 0.86 \leq& \Gamma_{20.1} \leq 0.9 \\ 0.7 \leq& \Gamma_{20.2} \leq 0.74 \quad . \end{aligned} \tag{5.20}$$

Regarding the $\Gamma_{19.4}$, since the uncertainty was not declared, the value was allowed to fluctuate within 100 keV range. In Fig 5.35, the results of the resonance fit are shown with red curves. Black curves correspond to the each component of the resonance states of ^{8}Be. The obtained fit parameters are listed in Table 5.3. By taking ratios of the fit parameter A for each resonance state of ^{8}Be between the results of the ^{9}Be(^{3}He, α)^{8}Be*(p)^{7}Li$_{\mathrm{g.s.}}$ reaction and the ^{9}Be(^{3}He, α)^{8}Be*(p)^{7}Li$_{\mathrm{1st}}$ reaction, the Γ_{p1}/Γ_{p0} ratios were deduced. The results are listed in Table 5.4, as well as the branching ratio defined as $\Gamma_{p1}/(\Gamma_{p0}+\Gamma_{p1})$ given in %.

In the prior result, the branching ratio was reported to be about 1% around 18.91 MeV resonance. However, we obtained a completely different results that Γ_{p1} becomes quite large around that energy region. Another large ratio was obtained around the 19.86 MeV resonance. For the 19.235 MeV resonance, which is the most important resonance peak in the BBN scale, the branching ratio was found to about 1.3%. This may suggest that the ^{7}Be(n, p_1)^{7}Li has a little influence on the BBN prediction for ^{7}Li abundance.

TABLE 5.3: Resonance fit results using the Breit-Wigner expressions for 7 resonance states of ^{8}Be.

^{9}Be(^{3}He, α)^{8}Be*(p_0)^{7}Li		
E_X [MeV]	A_{p0}	Γ_{tot} [MeV]
18.91	$2.02\times10^{-12} \pm 4.99\times10^{-3}$	1.22×10^{-1} (fixed)
19.07	$6.10\times10^{-1} \pm 3.39\times10^{-2}$	$2.50\times10^{-1} \pm 8.83\times10^{-3}$
19.235	$2.76 \pm 5.36\times10^{-2}$	$2.43\times10^{-1} \pm 2.14\times10^{-3}$
19.4	$2.22\times10^{-1} \pm 1.19\times10^{-1}$	$5.00\times10^{-1} \pm 1.57\times10^{-1}$
19.86	$7.50\times10^{-9} \pm 2.33\times10^{-1}$	$8.00\times10^{-1} \pm 3.12\times10^{-2}$
20.1	$6.36\times10^{-1} \pm 6.05\times10^{-1}$	$8.60\times10^{-1} \pm 2.79\times10^{-2}$
20.2	$1.45 \pm 4.25\times10^{-1}$	$7.00\times10^{-1} \pm 4.00\times10^{-2}$
Be(^{3}He, α)^{8}Be*(p_1)^{7}Li*(0.478 MeV)		
E_X [MeV]	A_{p1}	Γ_{tot} [MeV]
18.91	$4.70\times10^{-3} \pm 2.98\times10^{-3}$	1.22×10^{-1} (fixed)
19.07	$7.78\times10^{-2} \pm 1.76\times10^{-2}$	$2.54\times10^{-1} \pm 5.52\times10^{-3}$
19.235	$3.65\times10^{-2} \pm 1.48\times10^{-2}$	$2.40\times10^{-1} \pm 3.37\times10^{-6}$
19.4	$3.75\times10^{-5} \pm 1.29\times10^{-1}$	$7.44\times10^{-1} \pm 4.50\times10^{-3}$
19.86	$1.57 \pm 3.78\times10^{-1}$	$7.66\times10^{-1} \pm 1.49\times10^{-1}$
20.1	$9.15\times10^{-2} \pm 2.68\times10^{-1}$	$9.00\times10^{-1} \pm 2.97\times10^{-2}$
20.2	$2.79\times10^{-1} \pm 1.30\times10^{-1}$	$7.11\times10^{-1} \pm 3.23\times10^{-2}$

TABLE 5.4: Experimental results of Γ_{p1}/Γ_{p0} ratio for each of the resonance states of ^{8}Be at the excitation energy from 18.91 to 20.2 MeV.

E_X [MeV]	J^π	Γ_{p1}/Γ_{p0}	$\Gamma_{p1}/(\Gamma_{p0}+\Gamma_{p1})$ [%]
18.91	2^-	$2.32\times10^{9}\pm5.73\times10^{18}$	100±139
19.07	3^+	$1.27\times10^{-1}\pm2.97\times10^{-2}$	11.3±2.6
19.235	3^+	$1.33\times10^{-2}\pm5.38\times10^{-3}$	1.3±0.5
19.4	1^-	$1.69\times10^{-4}\pm5.84\times10^{-1}$	0.01±58
19.86	4^+	$2.09\times10^{8}\pm6.49\times10^{15}$	100±37
20.1	2^+	$1.44\times10^{-1}\pm4.44\times10^{-1}$	12.6±38.6
20.2	0^+	$1.92\times10^{-1}\pm1.06\times10^{-1}$	16.1±8.6

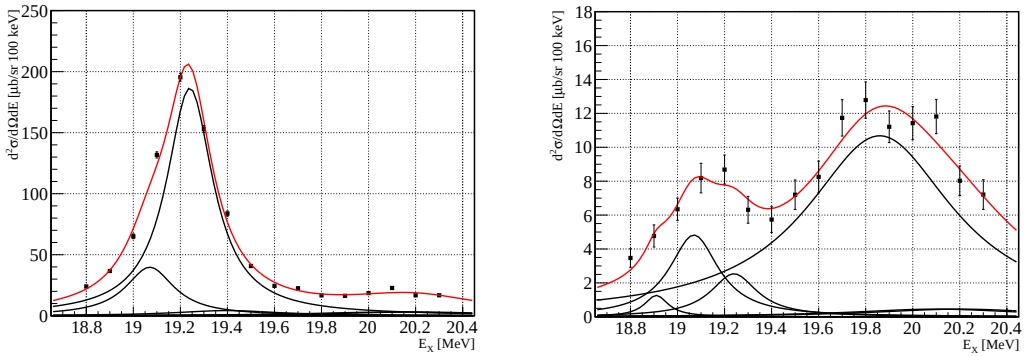

a) ground state b) 1st ex. state

FIGURE 5.35: Differential cross section of the ^{9}Be(^{3}He, α)^{8}Be*(p)^{7}Li$_{\text{g.s.}}$ reaction (left) and the ^{9}Be(^{3}He, α)^{8}Be*(p)^{7}Li$_{\text{1st}}$ reaction (right) as a function of the excitation energy of ^{8}Be. Resonance fit results are represented by the red curves in each graphs.

Chapter 6

Summary

We have carried out experiment of the $^{9}\mathrm{Be}(^{3}\mathrm{He},\alpha)^{8}\mathrm{Be}^{*}(p)^{7}\mathrm{Li}$ reaction to deduce the Γ_{p1}/Γ_{p0} ratio at the Tandem accelerator facility in Japan Atomic Energy Agency. A 1 μm thick beryllium target was tilted by 45° relative to the beam direction and irradiated by a ^{3}He beam accelerated at 30 MeV. Resonance states at the excitation energy from 18.91 to 20.2 MeV populated by the $(^{3}\mathrm{He},\alpha)$ reaction were identified by measuring the magnetic rigidity of α particles at zero degree using the magnetic spectrograph ENMA. Decay-protons were measured in coincidence with α particles by three silicon strip detectors surrounding the target for the angular range from 49° to 150°. We have succeeded in measuring the p_1 decay events separately from the p_0 decay events for the first time. A resonance fit with Breit-Wigner expressions was performed on the differential cross sections $d^2\sigma/d\Omega dE_X$ for both $^{9}\mathrm{Be}(^{3}\mathrm{He},\alpha)^{8}\mathrm{Be}^{*}(p)^{7}\mathrm{Li}_{\mathrm{g.s.}}$ and $^{9}\mathrm{Be}(^{3}\mathrm{He},\alpha)^{8}\mathrm{Be}^{*}(p)^{7}\mathrm{Li}^{*}_{\mathrm{1st}}$ reactions. The deduced Γ_{p1}/Γ_{p0} ratio suggests that the p_1 decay has strong peaks around the resonance states of ^{8}Be at 18.91 and 19.86 MeV. Around the 19.235 MeV resonance peak, which is the most important resonance state in the BBN scale, the ratio was found relatively small. Therefore, the $^{7}\mathrm{Be}(n,p_1)^{7}\mathrm{Li}$ reaction cross section may have little influence on the ^{7}Li abundance prediction in the BBN model.

In order to improve the statistical accuracy in the Γ_{p1}/Γ_{p0} ratio, additional measurements are desired with longer measurement time. Also, systematic errors have to be evaluated in the process of deriving the cross section data: In any calculation processes (transformation of variables between two kinematical frames, scattering angle of particles, Jacobian), it was always assumed that the recoil angle of ^{8}Be was at 180° with respect to the beam direction. This allowed to obtain the "average" value of the parameters, however, it is necessary to calculate the uncertainty in each variable due to this assumption. Thus, a simulation using Monte Carlo is required as a future prospect.

Appendix A

The Abundance of Contaminants in the ^{9}Be Target

A ^{9}Be target was prepared for the $^{9}\mathrm{Be}(^{3}\mathrm{He},\alpha)^{8}\mathrm{Be}^{*}(p)^{7}\mathrm{Li}$ reaction measurement by LEBOW company. The material purity is reported to have 99.8%, however, the species of and abundances of contaminants are not clarified. Therefore, to obtain these information, the elastic scattering measurement of α particles at 30 MeV was performed at the Cyclotron and Radioisotope Center (CYRIC) in Tohoku university. Using the ΔE-E method with the telescope silicon detectors, it was found that the ^{9}Be target contains ^{12}C and ^{16}O of about 1.1% and 1.6% impurities, respectively.

A.1 Property of Target

A 1 μm thick ^{9}Be target was prepared by LEBOW company in USA. It is 10 mm in diameter. The material purity is reported to have 99.8%. The 10×10 cm^2 kapton ($C_{22}H_{10}N_2O_5$) and mylar ($C_{10}H_8O_4$) sheets were prepared for the use of the reference targets. Their areal densities were determined by measuring the weights. Then, the sheets were cut into samples which both have $\varnothing$8 mm surface. The properties of the targets are listed in the Table A.1.

A.2 Experimental Setups

The experimental setup consists of the target of interest (^{9}Be, kapton, mylar targets are mounted on a movable ladder) and two silicon semiconductor detectors (SSD1 and SSD2) placed in a holder to compose a telescope detector. A collimator whose solid angle is 7.9 msr is placed at the entrance of the holder. See Fig. A.1 for the schematic drawing of the setup. The SSD1 and SSD2 have 75 μm and 500 μm thickness, respectively. Since the range of α particles at 30 MeV in silicon medium is 424 μm, this telescope setup is thick enough to stop and measure the energy of α particles. The thickness of the dead layer of each SSD is not examined. The setup was installed in a vacuum chamber whose pressure was kept around 10^{-5} mbar.

A beam of α particles was accelerated by the cyclotron at 30 MeV. The beam spot was tuned to a rectangular shape with 2.5 mm height and 1.8 mm wide. The beam intensity was measured by the current integrator placed at zero degree which generates an electric signal every electric charge of 10^{-10} C is accumulated. The angular distribution of elastic scattering was measured at 40°, 50°, and 60° with respect to the beam direction. In Fig. **??**, the circuit used for the experiment is depicted.

TABLE A.1: Property of Target

Name	Composition	Thickness [μm]	Areal Density [$\mu g/cm^2$]
^{9}Be	^{9}Be and contaminants	1.0	185.0
Kapton	$(C_{22}H_{10}N_2O_5)_n$	7.84	1.113×10^3
Mylar	$(C_{10}H_8O_4)_n$	1.20	167.64

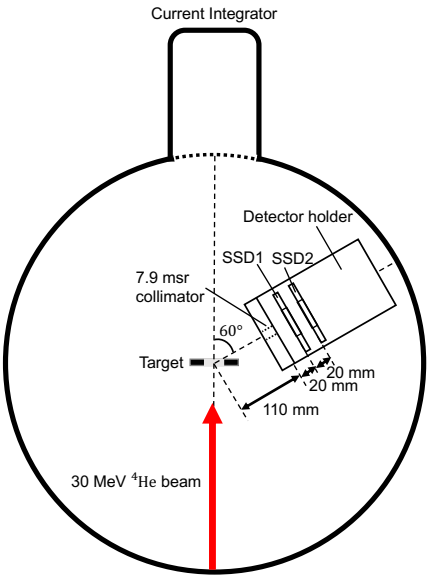

FIGURE A.1: Schematic drawing of the scattering chamber.

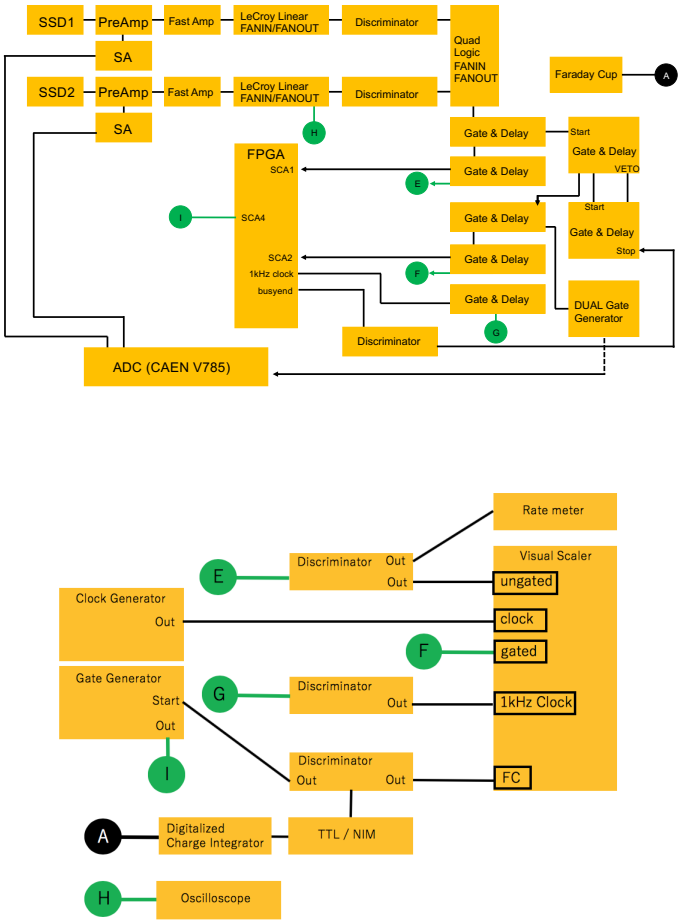

FIGURE A.2: Circuit diagrams. The upper diagram represents the circuit in the experimental hall and the lower represents the one in the control room.

A.3 ΔE-E Spectrum

Fig. A.3 shows the correlation diagram between the energy losses at SSD1 (ΔE_1) and SSD2 (E_2), for the case when the target was ^{9}Be and the measurement angle was at 60° to the beam direction. In this diagram, four curves decreasing with respect to the increase in x-axis can be seen. They represent, respectively, protons, deuterons, tritons and α particles in the order of left to right. At the top of the banana curve of protons, there is a part downwardly folded around $\Delta E_1 = 0.8$ keV. This represents that particles pass through even SSD2. Since the maximum range of ^{3}He in silicon medium is 47 μm for the scattering angle is at 60°, ^{3}He particles are not appearing in the diagram. Thus, the skirt of α particles is due to the channeling effect.

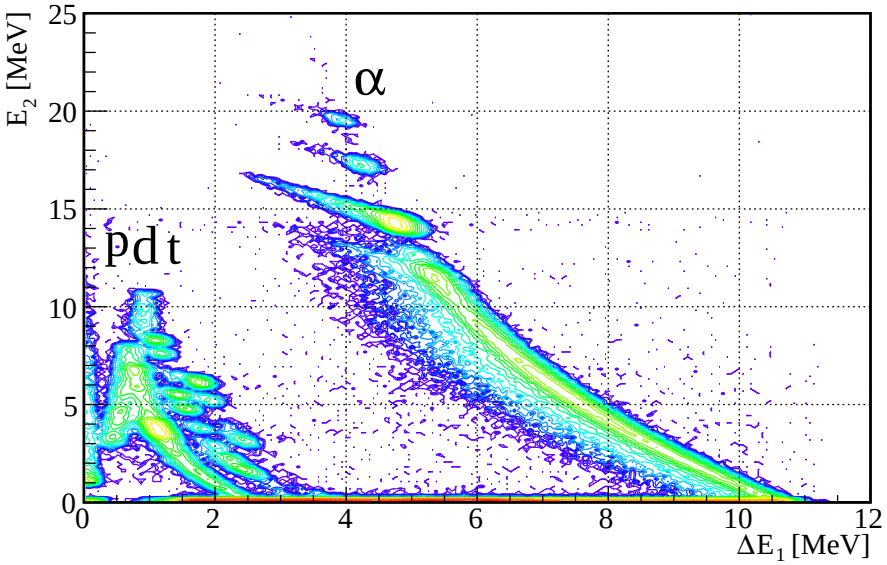

FIGURE A.3: ΔE-E spectrum. Measurement run with ^{9}Be target and with SSDs placed at the angle of 60 degrees to the beam direction.

A.4 Analysis

A.4.1 Data Processing

The energy loss ΔE of a charged particle in medium is in short given by

$$\Delta E \propto \frac{z^2}{\beta^2} \sim \frac{Auz^2}{2E} \quad , \tag{A.1}$$

where, z, β, E_{tot} and A are, respectively, the electric charge, velocity, kinetic energy and mass number of the particle, and u is the unified atomic mass unit. Here, the square root of the product of ΔE and E provides a specific value according to A and z,

$$\sqrt{\Delta E \cdot E} \sim z\sqrt{\frac{Au}{2}} \quad , \tag{A.2}$$

and it is $\sqrt{\Delta E \cdot E} = \sqrt{\Delta E_1 \cdot (\Delta E_1 + E_2)}$ in our measurement. The Fig. A.4 shows the correlation diagram between $\sqrt{\Delta E \cdot E}$ and E, which is from the same measurement as the Fig. A.3. Data in the solid line were projected to the Y-axis to obtain the kinetic energy spectrum of α particles. In Fig. A.5 - Fig. A.7, energy spectra are shown for the case with each target. The mean value of each peak was obtained by fitting the histogram with a Gaussian. For such histograms like in Fig. A.6, in which peaks are overlapping each other, a combination of multiple Gaussians was used for the fitting. Then, comparing the mean values with the theoretical kinematics calculation, the elements contributed to each peak were identified. As the result, it was found that there are mainly ^{12}C and ^{16}O contaminants in the ^{9}Be target, while ^{14}N contaminant was not found. Plus, as can be seen at the right side of the peak-3 in Fig. A.5, there might be also some ^{35}Cl contaminant. The origin of this contaminant is not clear at all.

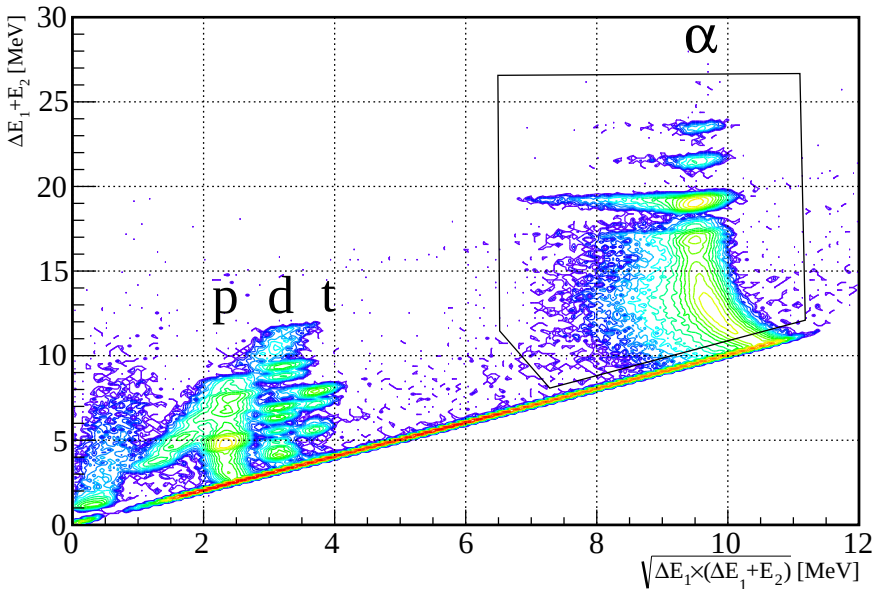

FIGURE A.4: Measurement with ^{9}Be target and with SSD placed at 60 degrees to the beam direction

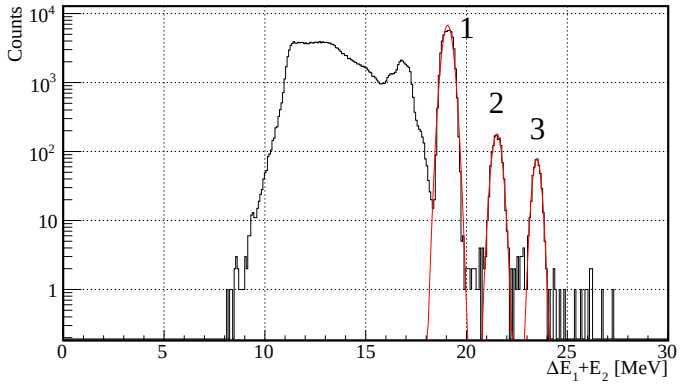

FIGURE A.5: Kinetic energy spectra of α particles scattered with ^{9}Be target.

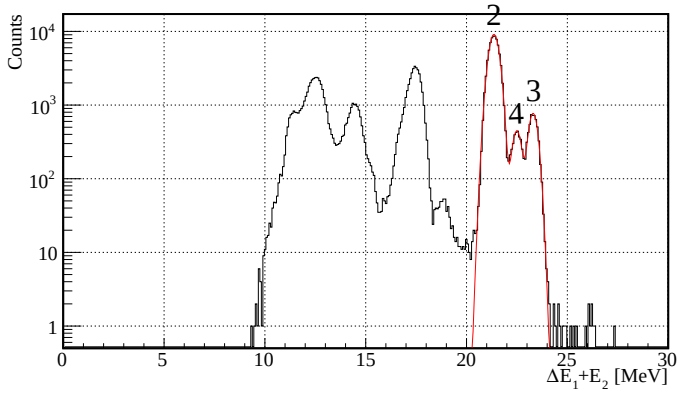

FIGURE A.6: Kinetic energy spectra of α particles scattered with kapton target.

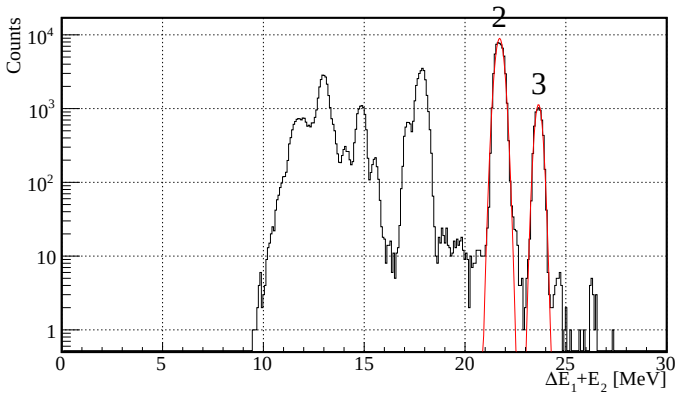

FIGURE A.7: Kinetic energy spectra of α particles scattered with mylar target.

TABLE A.2: Kinematics calculation

Scattering Angle [deg.]	Target elements and scattered energy [MeV]			
	^{9}Be	^{12}C	^{14}N	^{16}O
40	24.24	25.60	26.20	26.65
50	21.59	23.52	24.38	25.03
60	18.84	21.30	22.41	23.26

A.4.2 Abundance of Contaminants

The total number of particles detected (the yield) of each peaks in the total kinematic energy spectra was estimated from the Gaussian fitting. The relation between the yield and the differential cross section is given by

$$Y = I \times N \times \Delta\Omega \times \frac{d\sigma}{d\Omega} \times \epsilon \quad , \tag{A.3}$$

where Y [s^{-1}] is the yield, I [$s^{-1}m^{-2}$] is the beam intensity, N is the number of target element within the beam spot, $\Delta\Omega$ [sr] is the solid angle of the detector, $d\sigma/d\Omega$ [m^2sr^{-1}] is the differential cross section, and ϵ is the detector efficiency. Number of target can be rewritten in terms of the density ρ [$\mu g \cdot m^{-2}$] as

$$N = \frac{\rho \times S \times N_A}{A} \quad , \tag{A.4}$$

where S [m^2] is the beam spot surface, N_A is the Avogadro's number and A is the mass number. The areal density of targets are listed in Table. A.1. Regarding the "areal density" of each element in compound targets, ^{12}C and ^{16}O, ρ is multiplied by the mass fraction between an element and the whole compound, e.g.

$$\rho_{^{12}\text{C in kapton}} = \rho_{\text{kapton}} \times \frac{12 \times 22}{12 \times 22 + 1 \times 10 + 14 \times 2 + 16 \times 5} \tag{A.5}$$

The solid angle of the detector $\Delta\Omega$ and the differential cross section are the same for all targets for the same element. Thus, considering Eq.(A.3) - Eq.(A.5) the areal

TABLE A.3: Abundance of contaminants in ^{9}Be. Reference target : kapton

Contaminant	Detector angle [deg.]	Areal density [μg/cm^2]
^{12}C	40	2.53 ± 0.05
	50	2.36 ± 0.09
	60	1.55 ± 0.04
^{16}O	40	1.84 ± 0.09
	50	3.27 ± 0.31
	60	2.46 ± 0.12

TABLE A.4: Abundance of contaminants in ^{9}Be. Reference target : mylar

Contaminant	Detector angle [deg.]	Areal density [μg/cm^2]
^{12}C	40	2.44 ± 0.04
	50	2.01 ± 0.07
	60	1.40 ± 0.04
^{16}O	40	2.79 ± 0.11
	50	4.67 ± 0.43
	60	2.63 ± 0.13

density of each contaminant in ^{9}Be can be derived. For the case of ^{12}C,

$$\rho_{^{12}\mathrm{C\ in\ }^{9}\mathrm{Be}} = \frac{Y_{^{9}\mathrm{Be}} \times I_{\mathrm{kapton}}}{Y_{\mathrm{kapton}} \times I_{^{9}\mathrm{Be}}} \times \rho_{^{12}\mathrm{C\ in\ kapton}} \tag{A.6}$$

Table A.3 and A.4 show the results of the experiment. It was found that ^{12}C occupies about 1.1 % and ^{16}O occupies about 1.6 % in the ^{9}Be target for the average.

Appendix B

TABLE B.1: $(^3\mathrm{He}, \alpha)$ reaction

$^9\mathrm{Be}(^3\mathrm{He}, \alpha)^8\mathrm{Be}$			
$E_X(^8\mathrm{Be})$ [MeV]	E_α [MeV]	$B\rho$ [Tm]	Measurement Range
0	46.729	0.987	×
...			×
16.626	31.889	0.815	×
16.922	31.615	0.811	◯
17.64	30.947	0.803	◯
18.15	30.471	0.797	◯
18.91	29.759	0.787	◯
19.07	29.608	0.785	◯
19.24	29.448	0.783	◯
19.4	29.297	0.781	◯
19.86	28.863	0.775	◯
20.1	28.636	0.772	◯
20.2	28.541	0.771	△
20.9	27.876	0.762	×

$^{12}\mathrm{C}(^3\mathrm{He}, \alpha)^{11}\mathrm{C}$			
$E_X(^{11}\mathrm{C})$ [MeV]	E_α [MeV]	$B\rho$ [Tm]	Measurement Range
0	31.58	0.811	◯
2	29.682	0.786	◯
4.319	27.452	0.756	×

$^{16}\mathrm{O}(^3\mathrm{He}, \alpha)^{15}\mathrm{O}$			
$E_X(^{15}\mathrm{O})$ [MeV]	E_α [MeV]	$B\rho$ [Tm]	Measurement Range
0	37.575	0.849	×
5.183	29.606	0.785	◯
5.241	29.55	0.784	◯
6.176	28.643	0.772	◯
6.793	28.044	0.764	×

TABLE B.2: $(^3\mathrm{He}, p)$ reaction

$^9\mathrm{Be}(^3\mathrm{He}, p)^{11}\mathrm{B}$			
$E_X(^{11}\mathrm{B})$ [MeV]	E_p [MeV]	$B\rho$ [Tm]	Measurement Range
0	38.873	0.91	×
...			×
7.286	31.153	0.813	×
7.978	30.412	0.803	◯
8.56	29.788	0.795	◯
8.92	29.401	0.79	◯
9.184	29.118	0.786	◯
9.272	29.023	0.784	◯
9.82	28.433	0.776	◯
9.873	28.376	0.776	◯
10.262	27.956	0.77	×

$^{12}\mathrm{C}(^3\mathrm{He}, p)^{14}\mathrm{N}$			
$E_X(^{14}\mathrm{N})$ [MeV]	E_p [MeV]	$B\rho$ [Tm]	Measurement Range
0	33.294	0.841	×
2.313	30.861	0.809	◯
3.948	29.133	0.786	◯
4.915	28.109	0.772	◯
5.106	27.906	0.769	×

$^{16}\mathrm{O}(^3\mathrm{He}, p)^{18}\mathrm{F}$			
$E_X(^{18}\mathrm{F})$ [MeV]	E_p [MeV]	$B\rho$ [Tm]	Measurement Range
0	30.661	0.807	×
0.937	29.684	0.793	◯
1.041	29.575	0.792	◯
1.08	29.535	0.791	◯
1.121	29.492	0.791	◯
1.7	28.887	0.783	◯
2.1	28.469	0.777	◯
2.523	28.026	0.771	△
3.062	27.461	0.763	×

TABLE B.3: $(^3\mathrm{He}, d)$ reaction

$^9\mathrm{Be}(^3\mathrm{He}, d)^{10}\mathrm{B}$			
$E_X(^{10}\mathrm{B})$ [MeV]	E_d [MeV]	$B\rho$ [Tm]	Measurement Range
0	30.295	1.129	×
...			×
12.56	16.629	0.835	×
13.49	15.553	0.807	◯
14.4	14.485	0.779	◯
18.43	9.502	0.631	×

$^{12}\mathrm{C}(^3\mathrm{He}, d)^{13}\mathrm{N}$			
$E_X(^{13}\mathrm{N})$ [MeV]	E_d [MeV]	$B\rho$ [Tm]	Measurement Range
0	25.517	1.035	×
...			×
9.000	15.778	0.813	×
9.476	15.243	0.799	◯
10.25	14.368	0.776	◯
10.36	14.243	0.772	◯
10.833	13.703	0.758	×

$^{16}\mathrm{O}(^3\mathrm{He}, d)^{17}\mathrm{F}$			
$E_X(^{17}\mathrm{F})$ [MeV]	E_d [MeV]	$B\rho$ [Tm]	Measurement Range
0	24.219	1.009	×
...			×
7.95	15.756	0.813	×
8.01	15.69	0.811	◯
8.07	15.625	0.809	◯
8.075	15.619	0.809	◯
8.2	15.483	0.806	◯
8.383	15.283	0.8	◯
8.416	15.247	0.799	◯
8.436	15.225	0.799	◯
8.75	14.881	0.79	◯
8.76	14.87	0.789	◯
8.825	14.799	0.787	◯
8.98	14.629	0.783	◯
9.17	14.42	0.777	◯
9.45	14.111	0.769	×

TABLE B.4: $(^3\mathrm{He}, t)$ reaction

$^9\mathrm{Be}(^3\mathrm{He}, t)^9\mathrm{B}$			
$E_X(^9\mathrm{B})$ [MeV]	E_t [MeV]	$B\rho$ [Tm]	Measurement Range
0	28.395	1.336	×
...			×
16.024	10.748	0.82	×
16.71	9.848	0.785	◯
17.076	9.355	0.765	×

$^{12}\mathrm{C}(^3\mathrm{He}, t)^{12}\mathrm{N}$			
$E_X(^{12}\mathrm{N})$ [MeV]	E_t [MeV]	$B\rho$ [Tm]	Measurement Range
0	10.939	0.828	×
0.96	9.772	0.782	◯
1.191	9.486	0.771	△
1.8	8.719	0.739	×

$^{16}\mathrm{O}(^3\mathrm{He}, t)^{16}\mathrm{F}$			
$E_X(^{16}\mathrm{F})$ [MeV]	E_t [MeV]	$B\rho$ [Tm]	Measurement Range
0	13.428	0.917	×
...			×
0.721	12.628	0.889	×
3.758	9.152	0.757	×

Bibliography

[1]B. D. Fields, Annu. Rev. Nucl. Part. Sci. **61**, 47–68 (2011).

[2]S. Weinberg, *Cosmology* (Oxford Univ Pr, 2008).

[3]J. C. Mather et al., Astrophys. J. **512**, 511 (1999).

[4]M. Tanabashi, (Particle Data Group) Phys. Rev. D **98** (2018).

[5]E. Aver, K. A. Olive, and E. D. Skillman, (2015) arXiv:1503.08146v1[astro-ph.CO].

[6]F. E. Wietfeldt and G. L. Greene, Rev. Mod. Phys. **83**, 1173 (2018).

[7]the ALEPH Collaboration et al., Phys. Rep. **427**, 257 (2018).

[8]A. Coc and E. Vangioni, (2017) arXiv:1707.01004[astro-ph.CO].

[9]R. Cooke et al., Astrophys. J. **781**, 31 (2014).

[10]T. Bania, R. Rood, and D. Balser, Nature **415**, 54 (2002).

[11]L. Sbordone et al., Astron. Astrophys. **522**, 26 (2010).

[12]*Planck* Collaboration XVI et al., Astron. Astrophys. **594**, A13 (2016).

[13]M. Pospelov and J. Pradler, Annu. Rev. Nucl. Part. Sci. **60**, 539–568 (2010).

[14]R. H. Cyburt, B. D. Fields, and K. A. Olive, Phys. Rev. D **69**, 123519 (2004).

[15]R. V. Wagoner, Astrophys. J. Suppl. Ser. **18**, 247 (1969).

[16]S. Kubono et al., Phys. Rev. C **91**, 055802 (2015).

[17]M. Barbagallo et al., Phys. Rev. Lett. **117**, 152701 (2016).

[18]T. Kawabata et al., Phys. Rev. Lett. **118**, 052701 (2017).

[19]G. Beaudet, Astron. Astrophys. **134**, 240 (1984).

[20]L. Damone et al., Phys. Rev. Lett. **121**, and the Supplement Material http://link.aps.org/supplemental/10.1103/PhysRevLett.121.042701, 042701 (2018).

[21]D. R. Tilley et al., Nucl. Phys. A **745**, 155–362 (2004).

[22]R. C. Hanna, Philos. Mag. **46**, 381 (1955).

[23]P. E. Koehler et al., Phys. Rev. C **37**, 3 (1988).

[24]P. Bassi, B. Ferretti, and G. Venturini, Nuovo Cimento **28**, 1049 (1963).

[25]K. K. Sekharan et al., Nucl. Instr. Meth. **133**, 253–257 (1976).

[26]J. H. Gibbons and R. L. Macklin, Phys. Rev. **114**, 2 (1959).

[27]L. N. Generalov, S. N. Abramovich, and S. M. Selyankina, BULLETIN OF THE RUSSIAN ACADEMY OF SCIENCES: PHYSICS **81**, 6 (2017).

[28]H. Liskien and A. Paulsen, Atomic Data and Nuclear Data Tables **15**, 57–84 (1975).

[29]J. M. Blatt and V. F. Weisskopf, *Theoretical Nuclear Physics* (John Wiley & Sons Inc., New York, 1952).

[30]O. Pisanti et al., Comp. Mucl. Comm. **178**, 956–971 (2008).

[31]P. D. Serpico et al., (2004) arXiv:astro-ph/0408076v2.

[32]https://ttandem.jaea.go.jp/.

[33]Y. Sugiyama, N. Shikazono, and H. Ikezoe, Nucl. Inst. Meth. **187**, 25–35 (1981).

[34]Y. Sugiyama et al., Nucl. Inst. Meth. **215**, 17–25 (1983).

[35]Y. Sugiyama et al., Nucl. Inst. Meth. **A281**, 512–516 (1989).

[36]A. Sharma, SLAC J. ICFA **16**, 3 (1998).

[37]T. Sakakibara, Master's thesis of Tohoku university (2019).

Acknowledgements

First of all I would like to thank Professor Naohito Iwasa. Without his guidance and persistent supports this work could not have been accomplished. The door to his office was always open whenever I had a question about my research. I have learnt many things throughout last 2 years of master degree, and I would like to return the favor in any experimental works in the future.

A very special gratitude goes out to Professor Shigeru Kubono for a lot of helps, and sincere and valuable advices. The discussions we had together surely led our experiment to be successful. He has taught me how to proceed an experiment in order to achieve the purpose, and also gave me lectures with patience and conviction, which led me to a further and better scientific point of view.

I would also like to thank Dr. Katsuhisa Nishio for the opportunity to perform this experiment at the Tandem facility in JAEA. I am also grateful to the following staff in JAEA: Dr. Kentaro Hirose, Dr. Hiroyuki Makii, Dr. Riccardo Orlandi, Mr. Makoto Matsuda and the operators at the Tandem facility. It was a very exciting moment to work on the experiment together.

Special thanks to Dr. Shunji Nishimura, Dr. Seiya Hayakawa and Dr. Takahiro Kawabata for collaboration at the experiment. Without their passionate participation, the experiment could not have been successful.

I thank my fellow lab-mate, Mr. Takahiro Sakakibara, for all the fun we had in the last three years.

Finally, I sincerely would like to express my huge gratitude to my mother for the encouragement, constant support in my life and making it possible for me to study physics in Tohoku university.